

CONTACTLESS EXTRACTION OF RESPIRATORY RATE
FROM DEPTH AND THERMAL SENSORS

A Thesis

presented to

the Faculty of the

Electrical and Computer Engineering Graduate School

at the University of Missouri-Columbia

In Partial Fulfillment

of the Requirements for the Degree

Masters

by

SHAWN FERNANDES

Dr. Marjorie Skubic, Thesis Supervisor

DECEMBER 2018

Copyright by Shawn Fernandes, December 2018

All Rights Reserved

The undersigned, appointed by the dean of the Graduate School, have examined the thesis entitled

CONTACTLESS EXTRACTION OF RESPIRATORY RATE
FROM DEPTH AND THERMAL SENSORS

presented by Shawn Fernandes,

a candidate for the degree of master of Electrical and Computer Engineering,

and hereby certify that, in their opinion, it is worthy of acceptance.

Professor Marjorie Skubic

Professor Mihail Popescu

Dr. Laurel Despins

DEDICATION

.... To my Mom and Dad, sister Deepika, brother in law Jonathan, cousins Melissa, Marsha and Marcus for their continuous support and guidance.

ACKNOWLEDGEMENTS

Foremost, I would like to thank my advisor, Dr. Marjorie Skubic, who shared with me a lot of her expertise and research insight and valuable feedback. I would also like to thank Moein Enayati, who helped me with troubleshooting few snippets of the code and for helping me refine the graphs. I also like to express my gratitude to Dr. James Keller, Dr. Mihail Popescu, Dr. Marilyn Rantz, Dr. Laurel Despins, Dr. Guilherme DeSouza, Brad Harris, Dr. Eric Stone, Akshith Ullal, Anup Mishra, Noah Marchal, Mary Mengxuan and to the members of the center of eldercare and rehabilitation technology faculty, students and staff, whose thoughtful advice often served to give me a sense of direction during my MS studies.

TABLE OF CONTENTS

ACKNOWLEDGEMENTS	ii
LIST OF ILLUSTRATIONS	viii
LIST OF TABLES	xi
ABSTRACT	xii
Chapter	
1. INTRODUCTION	
1.1. Motivation.....	1
1.2. Problem statement.....	2
2.RELATED WORK AND BACKGROUND	
2.1. Related Work.....	3
2.1.1. In-home monitoring.....	3
2.1.2.Non-invasive long-term monitoring of subjects	
2.1.2.1. Non-invasive monitoring of subjects.....	4
2.1.2.2. Automated region of interest detection	4
2.1.2.3. Methods of respiration detection using depth and thermal hardware.....	5
2.1.2.4. Methods of respiration detection using UWB radar.....	5
2.1.2.5. Methods of detection with chair sensor and contact sensors.....	6
2.1.2.6. Methods of detection with Time Of Flight sensor.....	6

- 2.2. Background
 - 2.2.1. Network Sensors at TigerPlace, (Columbia, MO).....6
- 3. METHODOLOGY
 - 3.1. System.....8
 - 3.2. Depth and Thermal Camera System.....10
 - 3.3. Lab Setup.....11
 - 3.4. Data Processing
 - 3.4.1. Capturing the depth data11
 - 3.4.2. Conversion of the depth data.....11
 - 3.4.3. Enhancement of the depth data.....13
 - 3.4.4. Respiratory waveform extraction from the depth data.....13
 - 3.5. Ground Truth Signal.....14
 - 3.6. Scoring Performance.....15
- 4. ALGORITHMS
 - 4.1. LSTM –RNN.....17
 - 4.2. Object Signature and LSTM-RNN.....20
 - 4.3. Region of Interest Detection.....21
 - 4.4. Generation of grids.....22
 - 4.4.1. Fixed Grids generation.....22
 - 4.4.2. Varying Grids generation.....23

4.5. Detecting common grids based on thermal signature.....	23
4.6. Extraction of Respiration variation.....	25
4.7. Separation of Respiration and Restless body motion.....	28
4.8. Splitting of respiration signals into Supine, Left lateral, Right lateral, Prone.....	29
4.9. Selecting the best signal from grid of signals.....	29
4.9.1. Parameter 1 – Signal Energy Parameter.....	30
4.9.2. Parameter 2 – Signal Variation Factor	30
4.9.3. Parameter 3 - Signal Strength Parameter.....	31
4.9.4. Parameter 4 - Signal Symmetry Parameter.....	31
4.9.5. Parameter 5 – Signal Amplitude Variation Parameter.....	31
4.9.6. Parameter 6 – Signal Noise Ratio of Maxima Parameter.....	32
4.9.7. Parameter 7 – Signal Noise Ratio of Minima Parameter.....	32
4.10. Computing Respiration rate for given grids based on peaks detected.....	34
4.11. Computing Respiration rate for given grids based on Fourier Transforms.....	34
4.12. Plotting algorithms.....	35
4.13. Grid size SNR computation.....	35
5. INITIAL RESULTS	
5.1. Initial trials.....	37
5.2. Subject 1 Trial 1.....	40
5.3. Subject 1 Trial 2.....	42

5.4. Subject 2 Trial 1.....	43
5.5. Subject 2 Trial 2.....	45
5.6. Subject 3 Trial 1.....	46
6. LAB RESULTS	
6.1. IRB2 Fixed grids Peak detection	
6.1.1. Average.....	48
6.1.2. Median.....	50
6.2. IRB2 Varying grids Peak detection	
6.2.1. Average.....	52
6.2.2. Median.....	54
6.3. IRB2 Fixed grids FFT detection	
6.3.1. Average	56
6.3.2. Median.....	58
6.4. IRB2 Varying Grids FFT detection	
6.4.1. Average.....	60
6.4.2. Median.....	62
7. DISCUSSION	
7.1. Results	
7.1.1 Pre IRB results.....	65
7.1.2 IRB2 fixed grids peak detection average.....	66

7.1.3	IRB2 fixed grids peak detection median of grids.....	68
7.1.4	IRB2 varying grids peak detection average.....	69
7.1.5	IRB2 varying grids peak detection median of grids.....	71
7.1.6	IRB2 fixed grids FFT detection average.....	72
7.1.7	IRB2 fixed grids FFT detection median of grids.....	74
7.1.8	IRB2 varying grids FFT detection average.....	75
7.1.9	IRB2 varying grids FFT detection median of grids.....	77
7.1.10	Overall Accuracy.....	78
7.2.	Challenges.....	79
8.	CONCLUSIONS	
8.1.	Contributions.....	81
8.2.	Future Work.....	82

LIST OF ILLUSTRATIONS

Figure		Page
3.A	Data processing steps	8
3.B	Three dimensional representation of depth frame.....	8
3.C	Original Frame and Enhanced Frame.....	9
3.D	Estimated Waveform and Ground Truth	9
3.E	Filtered Waveform and Ground Truth.....	10
3.F	Kinect Figure.....	10
3.G	Lab setup.....	12
3.H	Butterworth Filter.....	14
3.I	AD instruments Respiratory band.....	15
4.A	LSTM-Classification.....	17
4.B	LSTM-Regression.....	17
4.C	LSTM – RNN.....	18
4.D	LSTM – RNN synapse.....	18
4.E	Scale and rotation invariant object signature.....	20
4.F	Output of Region of interest detection function.....	21
4.G	Output of Fixed grid logic function.....	22
4.H	Output of varying grid logic function.....	23
4.I	Output of thermal grid function on fixed grids.....	24
4.J	Output of thermal grid function on varying grids.....	24
4.K	Raw respiration waveform.....	26
4.L	Three dimensional view of depth data.....	27
4.M	Comparison of ground truth and raw respiration waveform.....	27
4.N	Output of respiration and restless body movement separation function.....	28
4.O	Output of best signal selection algorithm.....	29
4.P	Output of Parameter 2 – Signal variation factor on Pure sine wave.....	30
4.Q	Output of SNR function – part1.....	33
4.R	Output of SNR function – part2.....	33

4.S	Output of Peak detection based respiration rate estimation.....	34
4.T	Output of SNR function on grid sizes for IRB1 trials.....	36
4.U	Output of SNR function on grid sizes for IRB2 trials.....	36
5.A	Depth image of person sitting on chair distance of 56’’.....	37
5.B	Raw respiration variation of person sitting on chair.....	37
5.C	Depth image of person sitting on chair distance of 98’’.....	38
5.D	Raw respiration variation of person sitting on chair.....	38
5.E	Raw depth image of person on bed.....	39
5.F	Enhanced depth image of person on bed.....	39
5.G	Raw depth waveform for different positions on bed.....	40
5.H	Subject 1 Trial 1 Supine position.....	40
5.I	Subject 1 Trial 1 Left lateral position.....	41
5.J	Subject 1 Trial 1 Right lateral position.....	41
5.K	Subject 1 Trial 2 Supine position.....	42
5.L	Subject 1 Trial 2 Left lateral position.....	42
5.M	Subject 1 Trial 2 Right lateral position.....	43
5.N	Subject 2 Trial 1 Supine position.....	43
5.O	Subject 2 Trial 1 Left lateral position.....	44
5.P	Subject 2 Trial 1 Right lateral position.....	44
5.Q	Subject 2 Trial 2 Supine position.....	45
5.R	Subject 2 Trial 2 Left lateral position.....	45
5.S	Subject 2 Trial 2 Right lateral position.....	46
5.T	Subject 3 Trial 1 Supine position.....	46
5.U	Subject 3 Trial 1 Left lateral position.....	47
5.V	Subject 3 Trial 1 Right lateral position.....	47
6.A	IRB2 fixed grids average supine peak detection algorithm.....	48
6.B	IRB2 fixed grids average left lateral peak detection algorithm.....	49
6.C	IRB2 fixed grids average right lateral peak detection algorithm.....	49
6.D	IRB2 fixed grids average prone peak detection algorithm.....	50
6.E	IRB2 fixed grids median supine peak detection algorithm.....	50
6.F	IRB2 fixed grids median left lateral peak detection algorithm.....	51

6.G	IRB2 fixed grids median right lateral peak detection algorithm.....	51
6.H	IRB2 fixed grids median prone peak detection algorithm.....	52
6.I	IRB2 varying grids average supine peak detection algorithm.....	52
6.J	IRB2 varying grids average left lateral peak detection algorithm.....	53
6.K	IRB2 varying grids average right lateral peak detection algorithm.....	53
6.L	IRB2 varying grids average prone peak detection algorithm.....	54
6.M	IRB2 varying grids median supine peak detection algorithm.....	54
6.N	IRB2 varying grids median left lateral peak detection algorithm.....	55
6.O	IRB2 varying grids median right lateral peak detection algorithm.....	55
6.P	IRB2 varying grids median prone peak detection algorithm.....	56
6.Q	IRB2 fixed grids average supine FFT detection algorithm.....	56
6.R	IRB2 fixed grids average left lateral FFT detection algorithm.....	57
6.S	IRB2 fixed grids average right lateral FFT detection algorithm.....	57
6.T	IRB2 fixed grids average prone FFT detection algorithm.....	58
6.U	IRB2 fixed grids median supine FFT detection algorithm.....	58
6.V	IRB2 fixed grids median left lateral FFT detection algorithm.....	59
6.W	IRB2 fixed grids median right lateral FFT detection algorithm.....	59
6.X	IRB2 fixed grids median prone FFT detection algorithm.....	60
6.Y	IRB2 varying grids average supine FFT detection algorithm.....	60
6.Z	IRB2 varying grids average left lateral FFT detection algorithm.....	61
6.AA	IRB2 varying grids average right lateral FFT detection algorithm.....	61
6.AB	IRB2 varying grids average prone FFT detection algorithm.....	62
6.AC	IRB2 varying grids median supine FFT detection algorithm.....	62
6.AD	IRB2 varying grids median left lateral FFT detection algorithm.....	63
6.AE	IRB2 varying grids median right lateral FFT detection algorithm.....	63
6.AF	IRB2 varying grids median prone FFT detection algorithm.....	64
7.A	Peak detection of depth variation of Subject #20 Grid 13.....	79
7.B	Peak detection of ground truth of Subject #20.....	80

LIST OF TABLES

Table		Page
4.A	Description of each gate of LSTM-RNN synapse.....	19
4.B	Functions for each gate of LSTM-RNN synapse.....	20
4.C	Algorithm for enhancing the depth data.....	25
7.A	Pre IRB Accuracy table.....	65
7.B	IRB2 fixed grids peak detection average manual grid selection.....	66
7.C	IRB2 fixed grids peak detection average automated grid selection.....	67
7.D	IRB2 fixed grids peak detection median of grids.....	68
7.E	IRB2 varying grids peak detection average manual grid selection.....	69
7.F	IRB2 varying grids peak detection average automated grid selection.....	70
7.G	IRB2 varying grids peak detection median of grids.....	71
7.H	IRB2 fixed grids FFT detection average manual grid selection.....	72
7.I	IRB2 fixed grids FFT detection average automated grid selection.....	73
7.J	IRB2 fixed grids FFT detection median of grids.....	74
7.K	IRB2 varying grids FFT detection average manual grid selection.....	75
7.L	IRB2 varying grids FFT detection average automated grid selection.....	76
7.M	IRB2 varying grids FFT detection median of grids.....	77
7.N	Overall accuracy for manual grid selection.....	78
7.O	Overall accuracy for automated grid selection.....	78
7.P	Overall accuracy for median of grid	78

CONTACTLESS EXTRACTION OF RESPIRATORY RATE FROM DEPTH
AND THERMAL SENSORS

Shawn Fernandes

Dr. Marjorie Skubic, Thesis Supervisor

ABSTRACT

Monitoring of respiration and restless sleep can help detect sleep disturbances that may be indicative of poor health and functional deficits. The current methods of estimating the respiratory rate such as Pneumograph, Capnograph, Photo-plethysmograph (PPG), Respiratory inductance plethysmography (RIP), involve sensors that are in contact with the patient. However, we have a few scenarios such as in hospitals and senior retirement communities where we would like to non-invasively collect the respiration rate and restless body motion where we are not able to place these types of sensors on patients. The initial requirement was to non-invasively monitor vital activity of patients in psychiatric centers.

This work investigates a novel approach to estimate the respiratory rate of a person lying on the bed using depth and thermal sensors along with other signal processing algorithms. The initial proof of concept tests were conducted on three subjects. Additional testing on a diverse group of ten participants (ranging in age and body type) was performed to validate the algorithm and the data collection method.

The depth and thermal waveforms captured were tested to explore a new approach for detecting individual respiratory rate noninvasively, using various algorithms to detect the region of the bed, common grids where a person is present, best signal selection from grids, and accurately estimate the respiratory rate and amount of body movement during sleep. The performance results at approximately 30 frames per second for the set of 10 participants was a mean error difference of 0.6 breaths per minute for the time domain algorithm and 0.8 breaths per minute for the frequency domain algorithm.

Chapter 1

Introduction

1.1 Motivation

The need for respiration rate monitoring is ever important, as it often indicates a person's health. Non-invasive and contactless assessment of respiration is getting much attention in the research community as the technology of various devices and sensors improves. Respiration rate, respiratory volume, i.e., volume of air inhaled and exhaled, and respiration variability, i.e., the variability in respiration rate are one of the important physiological parameters that need to be monitored to evaluate the health of the patient and overall well-being [1].

The motivation for this project was to non-invasively monitor the vital signs and activity of patients in the psychiatric center. The current protocol for monitoring high risk patients in a psychiatric hospital calls for a staff member to enter each room every 15 minutes and visually determine that each patient is still breathing. This protocol has been set up for fast intervention in the case of a patient self-inflicting harm. Patients not at high risk may be monitored less frequently; however, the psychiatrists report that it is often difficult to assess the amount of risk, and thus, they typically monitor all of the patients in a psychiatric ward every 15 minutes. In addition to the staff burden, this procedure is also disruptive to the patients who often are light sleepers. The psychiatrists are asking for a non-obtrusive way to monitor patients. The most urgent need is for monitoring breathing; they are also interested in monitoring sleep quality (e.g., in the form of heart rate and restless body motion in bed) and general activity out of bed during the night.

This project was part of the system to be installed in the psychiatric center. We proposed to investigate the use of radar, depth and thermal sensing in a psychiatric hospital room for capturing breathing, sleep quality, and activity out of bed. Due to the strict requirements, the monitoring systems must be mounted on a ceiling or wall with a flush mount, so that nothing could be hung over a mounting fixture. Our clinical partners were excited about testing a ceiling mounted sensing system above each bed or between the two beds in a room.

1.2 Problem statement

This work addresses the specific problem of (1) finding a depth and thermal sensor combination and algorithmic system arrangement capable of estimating respiratory signals from different body positions, (2) developing a new approach for detecting an individual's respiratory rate and body motion on the bed using signal processing techniques.

This thesis describes the method involved in estimating the respiration rate in a remote, non-invasive contactless manner with the help of Foresite Healthcare DSK3 system with depth and thermal sensors. We describe in detail our methodology of extracting the data from a distance of 2.3 meters, and also if the subject is sleeping with different positions on the bed. We use the Foresite Healthcare DSK3 system to capture the depth field frames and corresponding thermal images, and then analyze the data and extract the respiration variation from the depth data. A detailed discussion of related work, the hardware used, how the raw data from the sensor is converted into respiration waveforms, algorithms, the initial testing process and results, possible future implementations of the system is done here.

The Foresite Healthcare DSK3 device depth sensor is similar to the Kinect v1 depth sensor, and the thermal sensor is the FLIR lepton thermal sensor. This device is placed perpendicular on top and facing the bed mattress. This system captures the depth and thermal variation, from which we apply algorithms to estimate respiration rate and body motion during sleep and report them in a qualitative way. Respiratory rates are reported in breaths per minute. So far the Foresite Healthcare DSK3 system has reported promising results in estimating respiratory rate during sleep.

In order to determine if the Foresite Healthcare DSK3 depth sensor was sensitive enough to pick up the depth variations on the chest during respiration, different body positions on the bed, different body positions on the chair, different distances were tested, and the results looked promising. Many new algorithms were tried and developed for automated estimation of the respiratory rate from the depth variation compared to a Ground Truth (GT) signal. The test was conducted in a laboratory setting on three participants with five trials and then validated on another ten different subjects.

Chapter 2

Related Work and Background

2.1 Related work

A few of the well-known contact-based methods are Pneumograph, Capnograph, PPG, RIP, Accelerometer, Pneumograph, also known as Spirometry, measures the movement of a volume of air (flow rate). Capnograph is where we measure the difference of CO₂ between inhalation and exhalation. PPG is known as Photo-plethysmograph, which is an optical-based sensor that shows variation in respiration. RIP, is also known as respiratory inductance plethysmography which is a respiration band worn around the chest that changes its inductance based on variation.

From amongst the known approaches, radar has a limited subject range, time of flight lidar is an expensive sensor system, and hydraulic based pressure sensors have wires or components that could be intrusive to the existing patient environment.

The contactless method has more advantages in terms of comfort and accuracy as it does not inconvenience the subject in order to take respiration readings and would not increase the chances of patient distress. Patients would still prefer non-invasive methods, as the different components of the sensors like wires, power sources could be intrusive and cumbersome.

2.1.1 In-home monitoring

Technology is being applied across many environments to help people. Sensors, video, and telecommunications are being engineered into homes to help caregivers monitor their well-being and support their everyday activities. In this sense, considerable research efforts have been focused towards in-home monitoring, where 24/7 monitoring of health and activities is intended to reduce emergency events and make efficient management of existing conditions [1]. Technology use will also facilitate the detection of early signs of illness, rapid intervention to health changes and/or decline, supporting the desire to maintain independence in their own homes, which is routinely identified as a passionate priority for people as they age [2].

2.1.2 Non-invasive long-term monitoring of subjects

2.1.2.1 Non-invasive monitoring of subjects

The method of using non-invasive sensors to monitor patients has been successfully demonstrated by E. Stone et al [3]. The Kinect v1 depth streams were captured and stored remotely on the server. Automated matlab based scripts were then run on the depth data to analyze gait, walk strides, walk speed, fall detection for the enrolled subjects. The processed data is stored in a database, and the web-portal UI then proceeds to display the processed data and stored videos based on user selected.

As described by Al-Khalidi et al [4], various methods of respiration detection can be classed as contact or non-contact. The contact method is an invasive procedure wherein we need to place the sensor on the subject's body. The non-contact method is a non-invasive procedure where the sensor is located remotely. The various contact and non – contact respiration sensors are based on measuring respiratory sounds, airflow, movements, CO₂ emission, and oximetry probe.

The three different non-contact based methods for estimating the respiratory rate are radar-based, optical based, and thermal based. In the radar-based method, as demonstrated by Jong Kim et al [5], variation in radar signals is used to estimate the respiratory rate. It can either be Doppler or Constant Wave. In the optical-based method, as demonstrated by Benetazzo et al, [6], and by S. Šprager and D. Zazula [7], variation in light is used to estimate the respiration variation. We can have either red-green-blue (RGB), i.e. color based or infrared (IR), i.e. thermal based depth sensors. In the thermal-based method, as demonstrated by AL-Khalidi et al [8], variations in thermal heat signature is used to estimate the respiration rate from the variation.

2.1.2.2 Automated region of interest detection

The techniques of focusing on the region of interest around the chest in order to generate the depth frame containing the chest waveform variation for evaluating the rate of respiration has been implemented in two ways.

The first method, as demonstrated by Y. Lin et al [9], we can segment the picture based on depth reading and then estimate the position of head and chest. In this paper, the region of the chest is estimated once we know the region of the head. The region of the head is determined by the fixed ratio of the radius of the head for a given distance. This is first pre-determined for every distance for the sensor and then calibrated in the algorithm to determine the position of the head.

The second method, as demonstrated by T. Harada et al [10], we can use the pressure sensors mounted on the bed to estimate posture of the body and then focus on the region of interest. The pressure sensors on the bed relay the posture of the body, and then we can estimate the posture based on the shape of the pressure waveforms.

2.1.2.3 Methods of respiration detection using depth and thermal hardware

Few implementations as demonstrated by F. Benetazzo et al [12] at a distance of 1.4 meters, obtained maximum value of error mean value = 0.533 and correlation coefficient of $r = 0.9292$. Bakhtiyari et al [13] obtained mean correlation values of 0.539 and 0.571 with a Kinect v2 placed at a 1-meter distance. T. T. Dang et al [14], was able to detect respiration successfully with a PrimeSense camera placed at a distance of 0.7 meters.

2.1.2.4 Methods of respiration detection using UWB radar

Few implementations, as demonstrated by M. Baboli et al [15], wherein the subject was placed at a distance of 1 meter from the UWB transmitter, and 1 meter from the UWB receiver, and as the distance between the transmitter and receiver was 1 meter, we can deduce that the subject was about 1.414 meters from the system. Their algorithm is based on detection of movement energy in a specified band of frequency using wavelet and filter banks. One of the advantages of their algorithm is its ability to detect heart and respiration rates of a subject in an environment containing other motion. The heart movement is detected with the accuracy of 95% and respiration with the 100%. This algorithm has a repeatability of 93% which is a significant characteristic of the method.

2.1.2.5 Methods of detection with chair sensor and contact sensors

There have been various methods of respiration and heart rate detection via two three axis accelerometer sensors placed on subjects chest and back, such as demonstrated by Vertens et al [16], show mean percentage error of around 6% for respiration and 2% for heart rate. Griffiths et al [17] demonstrated the use of conductive fabric on the chairs armrests, and pressure sensors on the back of the chair to measure respiration rate, with an accuracy of 83% for heart rate and 73% for respiratory rate. W Grace et al [18] demonstrated the use of a hydraulic liquid filled bladder connected to a pressure transducer to measure the heart rate and the respiration rate, with an accuracy of 2.8 brpm and 9.9 bpm of variation in the model.

2.1.2.6 Methods of detection with Time Of Flight sensor

Garn H et al [19] demonstrated the extraction of respiration using the Microsoft time of flight camera. The Kinect v2 is commonly referred to the time of flight camera [20], [21]. The sensor was placed at a distance of 1.8 meters on the ceiling, with a resolution of 512 x 424, at a frame rate of 30Hz. They were able to report an accuracy of around 94% on average.

2.2 Background

2.2.1 Network sensors at TigerPlace (Columbia, MO)

TigerPlace, an active retirement community developed by Americare in affiliation with the MU Sinclair School of Nursing [22] and the Center for Elder care and Rehabilitation Technology at the University of Missouri have been working on maintaining and improving the quality of life of their residents. Sensor networks have been installed in the apartments of volunteer residents in order to support in-home monitoring for the purpose of capturing activity patterns using passive sensing. Changes in these patterns may indicate declining health [23]. These changes are compared to changes in the health conditions as part of ongoing research to develop early illness recognition methods. To date, over forty sensor

networks have been installed in homes of elderly residents [24].

The integrated sensor network include a bed sensor developed by colleagues at the University of Virginia [25]. It is a pneumatic strip placed on top of the bed mattress, underneath the bed linens, that captures qualitative heartbeat and respiration as well as restless body movement on the bed. Bed restless body movement is reported as one of four levels, depending on the time for continuous movement, while heart and respiration rate are reported as low, normal and high. The need for quantitative measure of heart rate and respiration motivated the development of a new transducer along with a new algorithm for detecting heartbeats and computing heart rate [26].

Chapter 3

Methodology

3.1 System

In order to estimate the respiratory rate, subjects were asked to rest on the bed, while the depth camera is perpendicularly placed on top of the bed at a distance of 2.3 meters. For this experiment, we only used the depth frames, as seen in Fig. 3B to extract the depth frame around the region of interest. As the subject is breathing, the rib cage moves synchronously with the respiratory rate. The chest depth variation is then captured with the help of the depth camera in the form of a sequence of depth frames. We have manually defined a depth frame around the chest area of the subject and computed the variation of the depth values in this region, in order to track the movement of the chest which is due to the respiration, as seen in Figure 3A and 3C. We filter the depth values for a certain range of distance around the subjects' body. As shown in Fig. 3D and 3E, we can capture a respiratory waveform that is close to the ground truth obtained by the RIP.

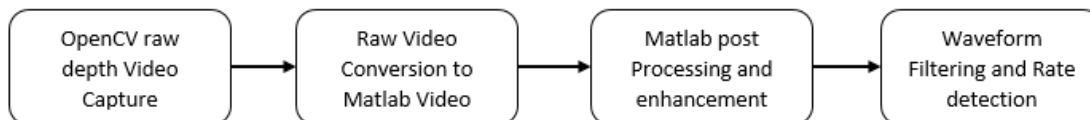


Fig. (3A) shows the data processing steps involved in extracting the respiratory waveform from the raw depth data sequence.

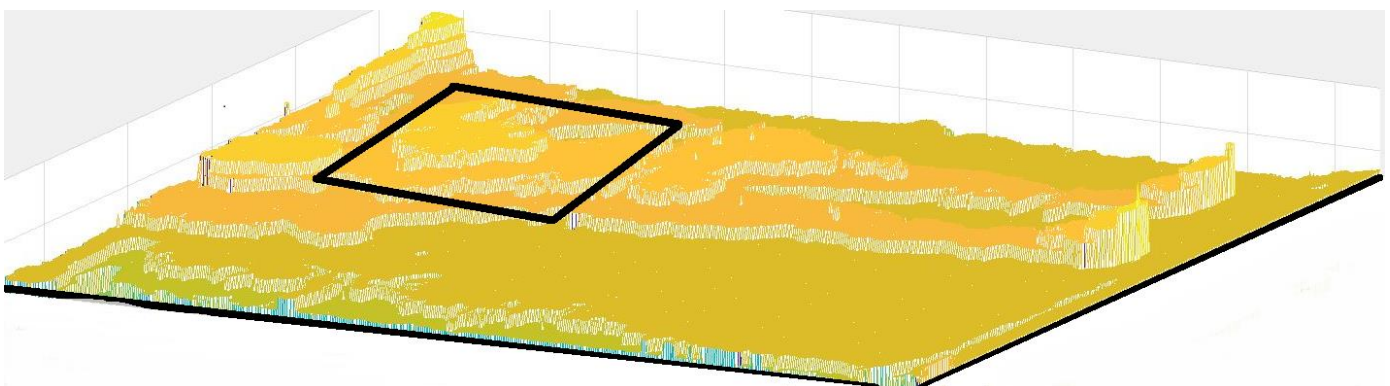


Fig. (3B) Picture showing the three-dimensional depth and the chest depth focusing around the region of interest.

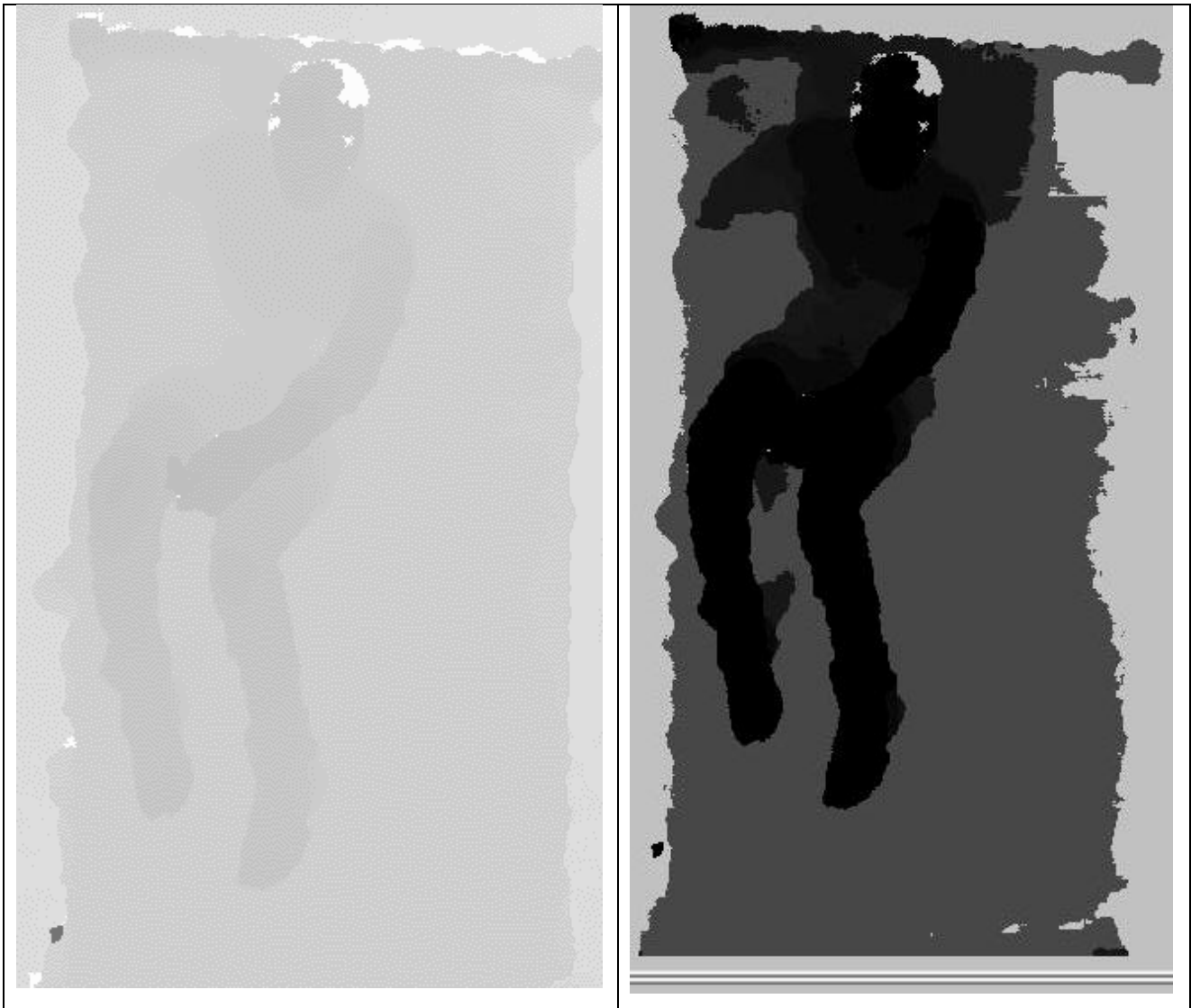


Fig. (3C) Picture at the left shows the original depth frame of a subject sleeping on the bed that has been captured by the depth camera, and picture at the right shows the enhanced depth frame.

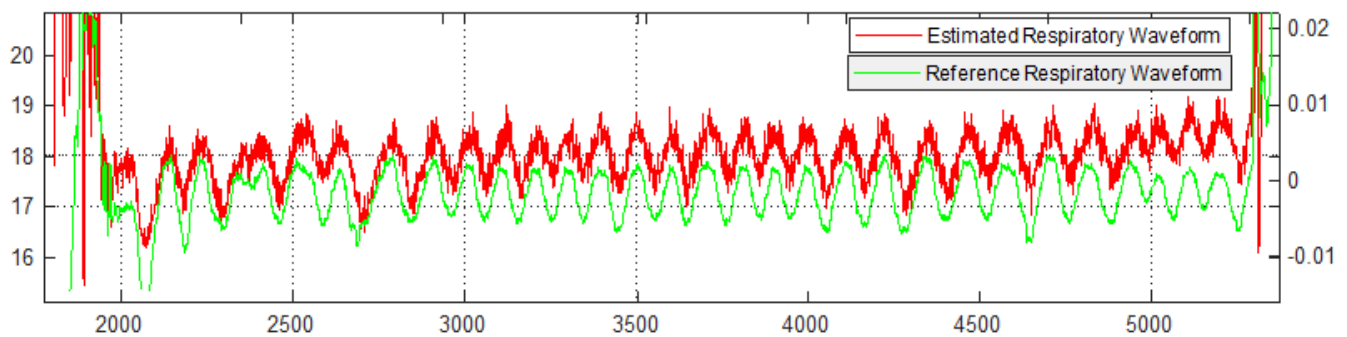


Figure. (3D) Picture showing high co relation between our estimated raw unfiltered waveform and reference ground truth signal.

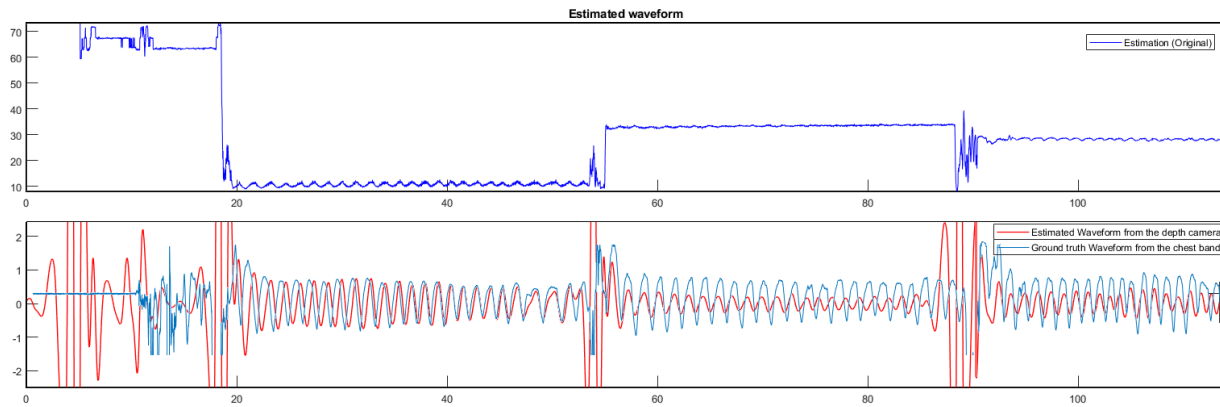


Fig. (3E) shows the results of our respiratory waveform estimation. The topmost graph is our estimated waveform from the depth data. The lower plot shows the overlapping of the ground truth waveform from the respiratory band (blue), and the filtered version of our estimated waveform from the depth camera (red). Comparing the two plots in the lower graph shows how well our estimation matches the ground truth respiratory waveform.

3.2 Depth and Thermal Camera System

Foresite Healthcare DSK3 system, as seen in Fig. 3F, comprises of the depth sensor similar to the Kinect v1 [27] and the FLIR lepton thermal camera [28]. Kinect v1 is an integrated camera system which comprises of an Infrared (IR) camera and a Red Green Blue (RGB) camera. Kinect v1, has a 640x480 RGB camera alongside a 640x480 depth camera. It has a max depth distance of 4.5m, Horizontal field of view at 57° and vertical field of view at 43°. The Depth sensor used in Kinect is based on the IR projector and an IR camera.



Fig. (3F) Picture showing the Foresite Healthcare DSK3, which has the Kinect v1 depth sensor [27] and FLIR thermal camera [28].

The IR projector projects a uniformly distributed pattern of light around the objects in a room. The depth camera then converts the density of the light scatters into a 3D depth frame, i.e. each two-dimensional coordinate of the picture frame has a corresponding depth value at a frame rate of 30 per second, as seen in image 3C. Kinect interfaces via a USB 2.0 compatible port.

The data generated by a depth camera is a depth intensity for every 2-dimensional coordinate, and this is analogous to a grayscale image of the scene. Each point in this depth frame image would have a value in the range of 0-255, which is an eight-bit unsigned integer.

3.3 Lab Setup

The study has been conducted in the standard lab setting, where the depth camera has been placed at a height of 2.3 meters over the bed surface, simulating realistic distances between ceiling and bed. As part of this paper, we have enhanced the algorithm to detect the respiration variation from a height of 2.3 meters. The sensor is placed directly above the bed, and faces the surface of the bed in a perpendicular direction, as seen in Fig. 3G

3.4 Data Processing Steps

3.4.1 Capturing the depth data

The depth data stream is captured and converted to MPEG format directly on Linux with OpenCV libraries. The source code has been compiled on C++, and it records the raw depth data stream into a YUV 8bit encoded sequence of frames at 30 fps, which can then be used for data extraction.

3.4.2 Conversion of the depth data

We then convert the captured depth data to MATLAB compatible format, for processing. As the captured data is in a single channel, we reconvert this to three channel compatible depth data using a third party video encoding software.

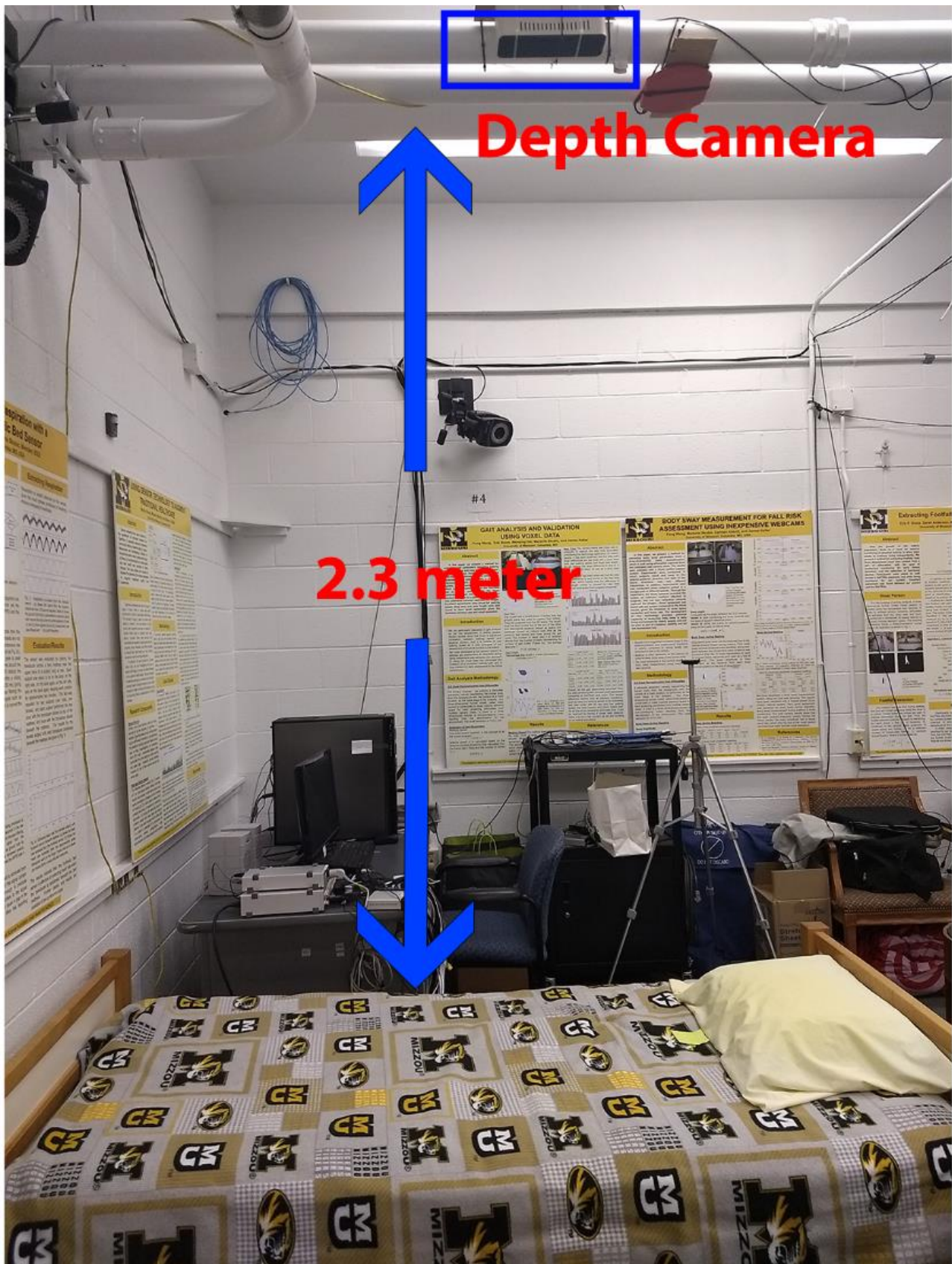


Fig. (3G) shows the lab setting, where we have the depth camera at a height of 2.3 meters from the bed.

3.4.3 Enhancement of the depth data

Once we import the depth data into Matlab, we then apply histogram stretching image enhancement and cropping processing techniques to get the raw respiration variation.

Histogram stretching is the process of stretching the minimum and maximum value of the image to the minimum and maximum limit of the image data type supported format respectively. We manually select the range of values and crop the depth frame, so that the region of interest as the area around the chest, where the respiration activity takes place.

3.4.4 Respiratory waveform extraction from the depth data

In order to smooth out the noise, we apply various filtering techniques to get the smoothed out respiration waveform. We then compare the respiration waveform to the ground truth.

The raw unfiltered waveform \mathbb{D} can be modeled as the sum of the respiratory waveform, the high-frequency artifacts, and low-frequency artifacts, as seen by equation (3)

$$\begin{aligned} \mathbb{D}_{raw-depth-waveform} &= \mathbb{R}_{respiration-waveform} + \epsilon_{high-frequency-artifacts} \\ &+ \epsilon_{low-frequency-artifacts} \end{aligned}$$

The ϵ high-frequency artifacts could be the combination of the movement of the subject on the bed and noise. The ϵ low-frequency artifacts can be attributed to noise. In order to extract the useful respiratory waveform \mathbb{R} , we would need to make use of a band-pass filter.

We implemented the fourth order Butterworth [29] band-pass filter, whose response is shown in Fig. (3H), with a high cut off frequency of 0.4Hz and a low cut off frequency of 0.15Hz in order to get the smoothed out respiratory waveform. The lower and higher frequencies were chosen in order to get the accurate respiration waveform frequencies from the raw unfiltered waveform.

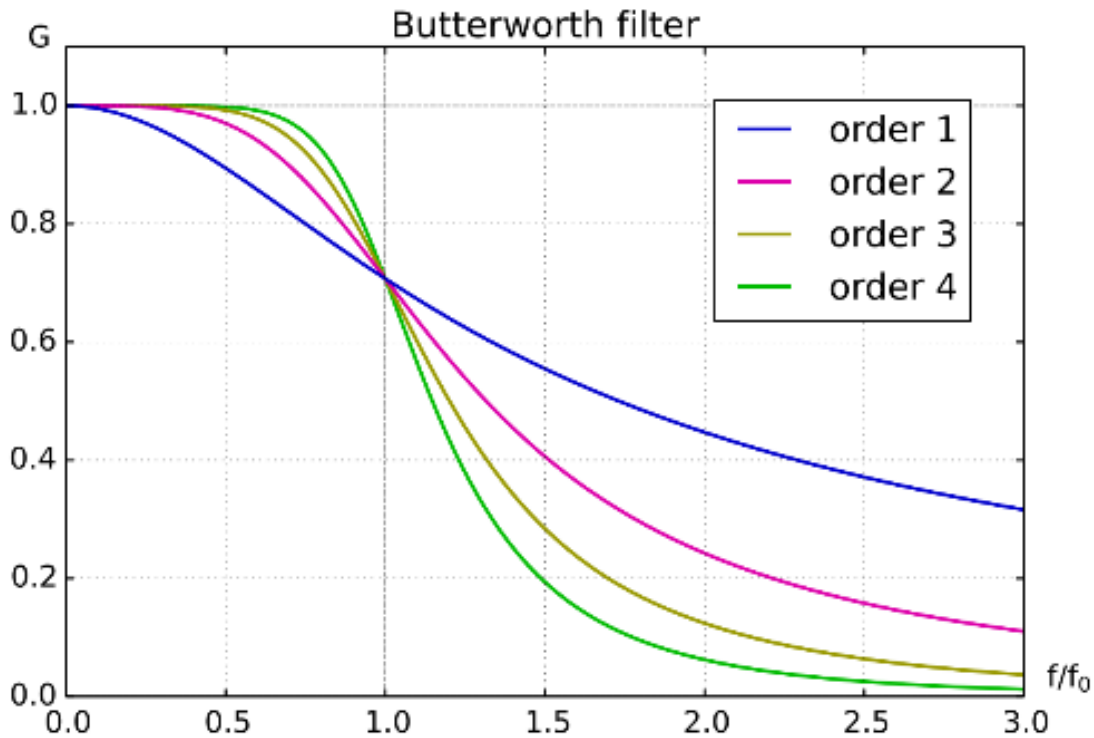


Fig. (3H) shows the frequency response of a Butterworth filter.

We also used the Savitzky-Golay [30] filtering in order to smooth out the respiration variation. The order of the filtering was 3, and the frame length was equal to the window size of the respiration window detection.

3.5 Ground Truth Signal

The Ground Truth signal for the respiratory waveform for the subjects was collected with the help of the RIP band worn on the subject's chest. RIP, as shown in Fig 3I, is also known as respiratory inductance plethysmography which is a respiration band worn around the chest that changes its inductance based on variation. This variation is captured on the Ad instruments 16/35 system [31] with labchart software.



Fig. (3I) shows the Ad instruments respiratory band, used for capturing the ground truth [31].

3.6 Scoring the performance

The criteria used for scoring the ability of the system for capturing respiratory rate was based on:

(a) Respiration Count: Ratio of the number of peaks from estimated waveform and ground truth in a fixed time segment / moving window / moving frame.

$$\text{Respiration Count \%} = \frac{\text{Number of Peaks in estimated waveform}}{\text{Number of Peaks in ground truth}}$$

(b) Peak to Peak interval: Average Ratio of the distance between similar respiration peaks between synchronized estimated waveform and ground truth.

$$\text{Peak to Peak interval \%} = \frac{1}{N} \sum_{k=1}^N \frac{\text{Distance of } P_1, P_2 \dots P_k \text{ in estimated waveform}}{\text{Distance of } P_1, P_2 \dots P_k \text{ in ground truth}}$$

(c) Breath to Breath respiratory rate: Ratio of the average respiratory rate taken between two beats between estimated waveform and ground truth for a fixed time segment

Breath to Breath Respiratory Rate %

$$= \frac{1}{N} \sum_{k=1}^N \frac{\text{Number of breaths in estimated waveform segment1, segment2, ... segmentk}}{\text{Number of breaths in ground truth segment1, segment2, ... segmentk}}$$

(d) Overall Interval: Ratio between the number of peaks in the entire segment between estimated waveform and ground truth for a given position

$$\text{Overall interval \%} = \frac{\text{Number of Peaks in estimated waveform}}{\text{Number of Peaks in ground truth}}$$

(e) Overall rate: Ratio of the Rate of overall interval between estimated waveform and ground truth

$$\text{Overall rate \%} = \frac{\text{Overall interval of estimated waveform}}{\text{Overall interval of ground truth}}$$

(f) Restless Body Movement ratio: The ratio of the total duration of time between the movement of the subject on the bed and the steady stable sleep position or posture of the person.

$$\text{Restless Body Movement \%} = \frac{\text{Total interval of subject movement}}{\text{Total interval of subject at rest + movement}}$$

(g) Respiration Accuracy: The Difference between the actual respiration rate and the ground truth.

$$\text{Respiration Accuracy} = \text{Actual Respiration Rate} - \text{Ground Truth Respiration Rate}$$

Chapter 4

Algorithms

4.1 LSTM-RNN network for sequence classification

The Long Short Term Memory is a type of Recurrent Neural Network (LSTM-RNN) [32] that can learn, be trained and predict long term dependencies between time steps of sequence data.

The core components of an LSTM network are a sequence input layer and an LSTM layer. A sequence input layer inputs sequence or time series data into the network.



Figure (4A) illustrates the architecture of a simple LSTM network for classification [32]. The network starts with a sequence input layer followed by an LSTM layer. To predict class labels, the network ends with a fully connected layer, a softmax layer, and a classification output layer.

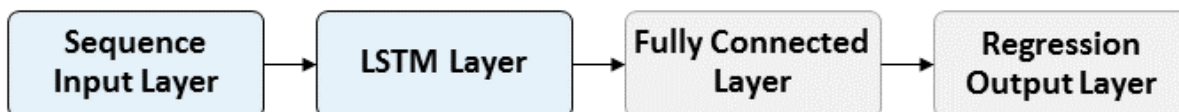


Figure (4B) illustrates the architecture of a simple LSTM network for regression [32]. The network starts with a sequence input layer followed by an LSTM layer. The network ends with a fully connected layer and a regression output layer.

The first LSTM unit takes the initial state of the network and the first time step of the sequence X_1 , and then computes the first output h_1 and the updated cell state c_1 . At time step t , the unit takes the current state of the network (c_{t-1}, h_{t-1}) and the next time step of the sequence X_t , and then computes the output h_t and the updated cell state c_t .

The state of the layer consists of the output state (also known as the hidden state) and the cell state. The output state at time step t contains the output of the LSTM layer for this time step. The cell state contains information learned from the previous time steps. At each time step, the layer adds information to or removes information from the cell state, where the layer controls these updates using gates.

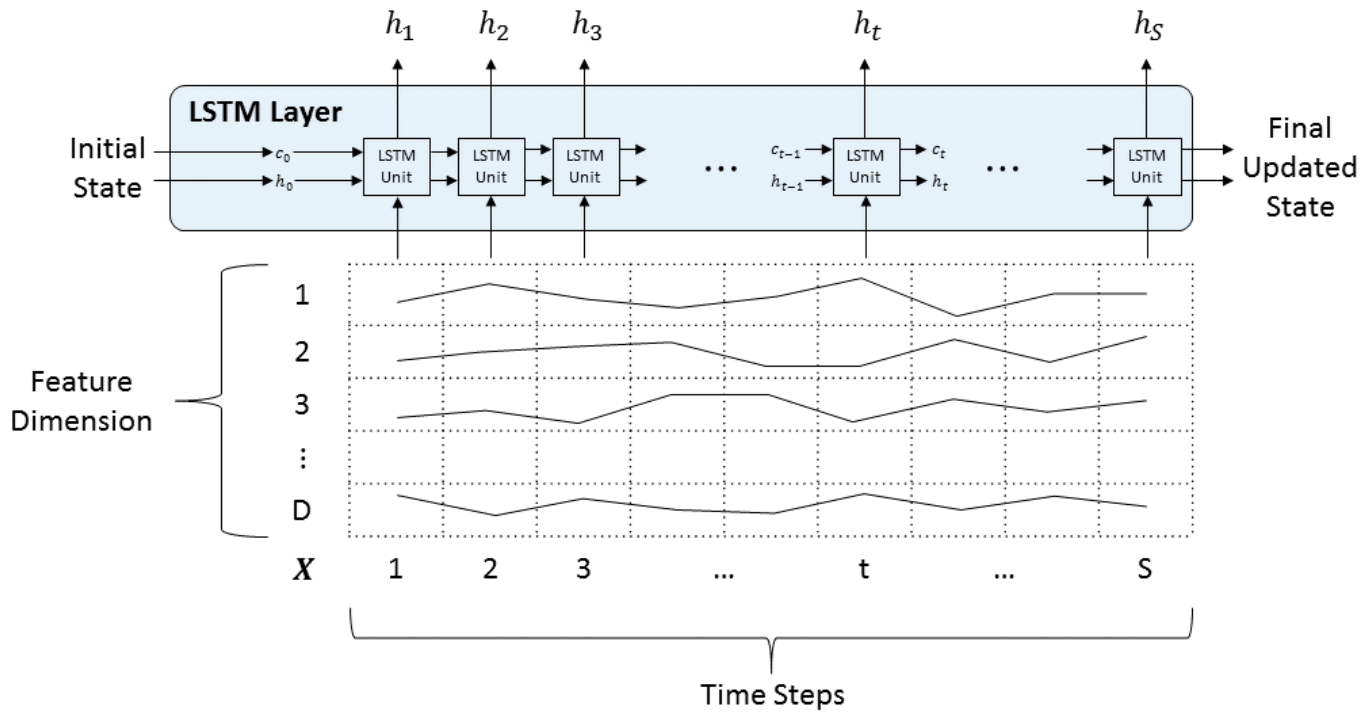


Fig (4C) illustrates the flow of a time series X with D features of length S through an LSTM layer [32]. In this diagram, h denotes the output (also known as the *hidden state*) and c denotes the *cell state*.

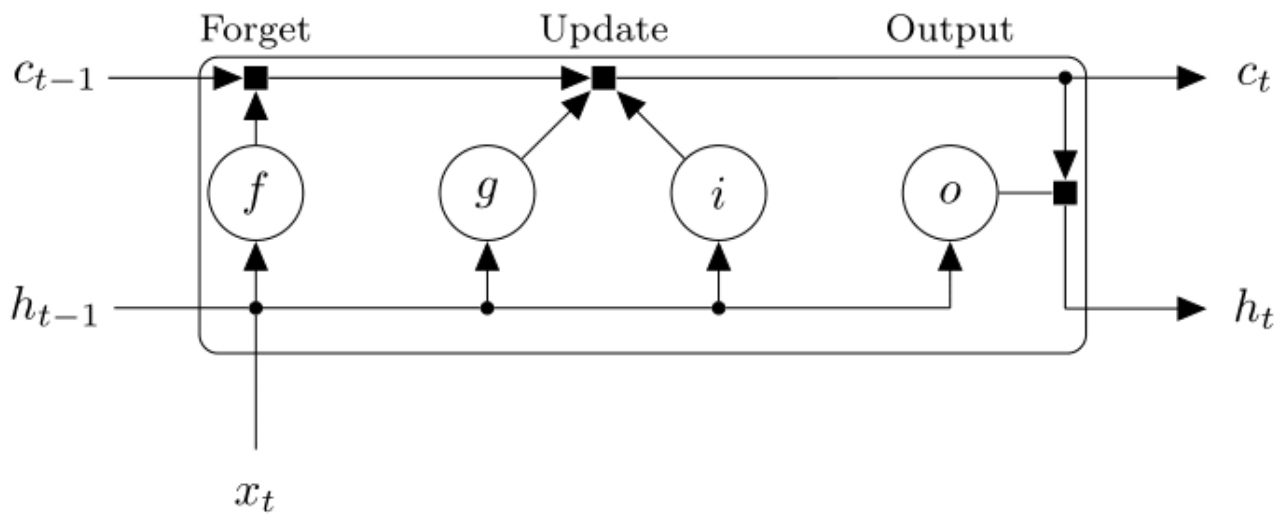


Figure (4D) illustrates the flow of data at time step t . The diagram highlights how the gates forget, update, and output the cell and output states [32].

Component	Purpose
Input gate (i)	Control level of cell state update
Forget gate (f)	Control level of cell state reset (forget)
Layer input (g)	Add information to cell state
Output gate (o)	Control level of cell state added to output state

Table (4A) summarizes the components that control the cell state and output state of the layer [32].

The learnable weights of an LSTM layer are the input weights W (Input Weights), the recurrent weights R (Recurrent Weights), and the bias b (Bias). The matrices W , R , and b are concatenations of the input weights, the recurrent weights, and the bias of each component, respectively. These matrices are concatenated as follows:

$$W = \begin{bmatrix} W_i \\ W_f \\ W_g \\ W_o \end{bmatrix}, R = \begin{bmatrix} R_i \\ R_f \\ R_g \\ R_o \end{bmatrix}, b = \begin{bmatrix} b_i \\ b_f \\ b_g \\ b_o \end{bmatrix}$$

where i, f, g , and o denote the input gate, forget gate, layer input, and output gate, respectively.

The cell state at time step t is given by

$$c_t = f_t \odot c_{t-1} + i_t \odot g_t,$$

where \odot denotes the Hadamard product (element-wise multiplication of vectors).

The output (hidden) state at time step t is given by

$$h_t = o_t \odot \tanh(c_t).$$

Component	Formula
Input gate	$i_t = \sigma (W_i x_t + R_i h_{t-1} + b_i)$
Forget gate	$f_t = \sigma (W_f x_t + R_f h_{t-1} + b_f)$
Layer input	$g_t = \tanh (W_g x_t + R_g h_{t-1} + b_g)$
Output gate	$o_t = \sigma (W_o x_t + R_o h_{t-1} + b_o)$

Table (4B) shows the formula for each component at time step t [32].

Here, σ denotes the sigmoid function given by $\sigma(x) = (1 + e^{-x})^{-1}$.

4.2 Identification of the object shape using scale and rotation invariant signature and classification by LSTM-RNN.

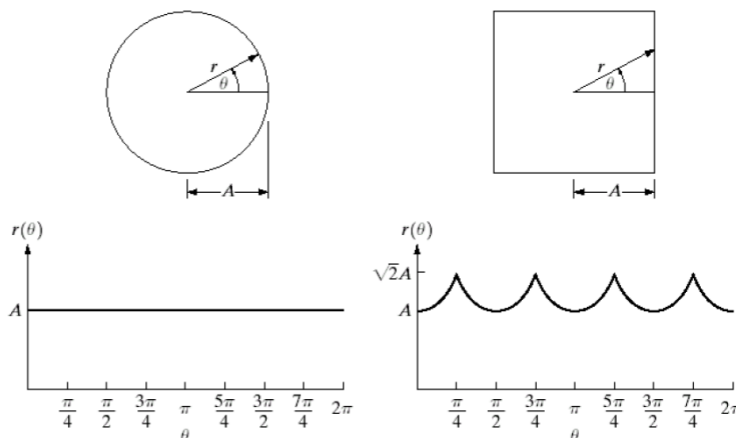
In order to obtain a scale invariant and rotation invariant signature of the object, we make use of the technique of plotting the distance between the centroid of the object and its boundaries [33] [34].

The object boundaries and its centroids are determined from existing MATLAB functions, and we then use the distance formula to plot the variation of the distance of the points from the centroid of the figure.

- The idea behind a signature is to convert a two dimensional boundary into a representative one dimensional function.

a b

FIGURE 11.5
Distance-versus-angle signatures. In (a) $r(\theta)$ is constant. In (b), the signature consists of repetitions of the pattern
 $r(\theta) = A \sec \theta$ for $0 \leq \theta \leq \pi/4$ and
 $r(\theta) = A \csc \theta$ for $\pi/4 < \theta \leq \pi/2$.



© 2002 R. C. Gonzalez & R. E. Woods

Figure (4E) is a snippet from the Digital Imaging Processing textbook which illustrates the concept of scale and rotation invariant signature of an object shape[33][34].

As seen in the Figure 4E, given an object, we first compute the centroid, and then plot a two dimensional graph of the distances from the centroid to the points on the boundary. As the distance vector traverses an entire rotation, an unique pattern emerges for each distinct image. By normalizing this image, we can also see a similar signature for similarly shaped objects irrespective of the size. This signature can then be fed and trained on a LSTM-RNN network for object detection and classification.

4.3 Region of Interest Detection

The algorithm detects the region of interest automatically. The input to the algorithm is the depth data frame containing the empty bed. The algorithm then uses thresholding logic and finds the region of interest, and obtains the x co-ordinate, y-co-ordinate, width and height of the specified region respectively. As seen in Fig 4F, the algorithm was able to threshold the bed region accurately and thereby obtain the region of interest co-ordinates. This is done by the function named **Bed_ROI.m**.

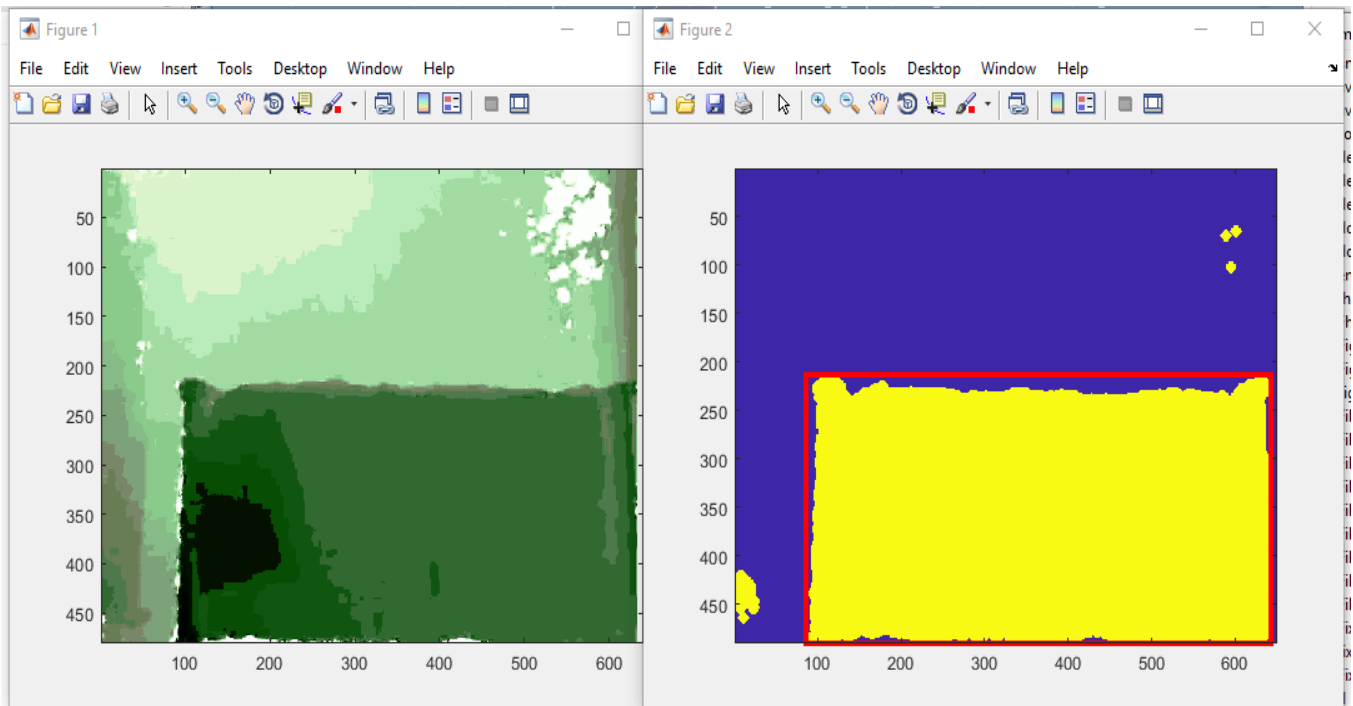


Figure (4F) shows the bed on the left, and the automated region of interest detection to the right.

4.4 Generation of Grids

Once the region of interest has been detected, the region needs to be divided into fixed segments called grids, for computation of variation. The region of interest can be divided into grids based on two below methodologies. The size of the grid also has an effect on the signal to noise ratio of the respiration variation seen. Creation of grids also allows us to focus on a few select grids, preferably around the region of the chest, and save computational resources and increase speed of computation.

4.4.1 Fixed Grids generation algorithm

In this method, the height and width dimensions of the grids need to be specified as an input parameter, and the algorithm draws grids starting from the centroid of the region of interest until the boundaries. As seen in Fig. (4G), this algorithm ensures that only the full sized grids are able to fit within the region. This is done by the function named **grid_logic.m**.

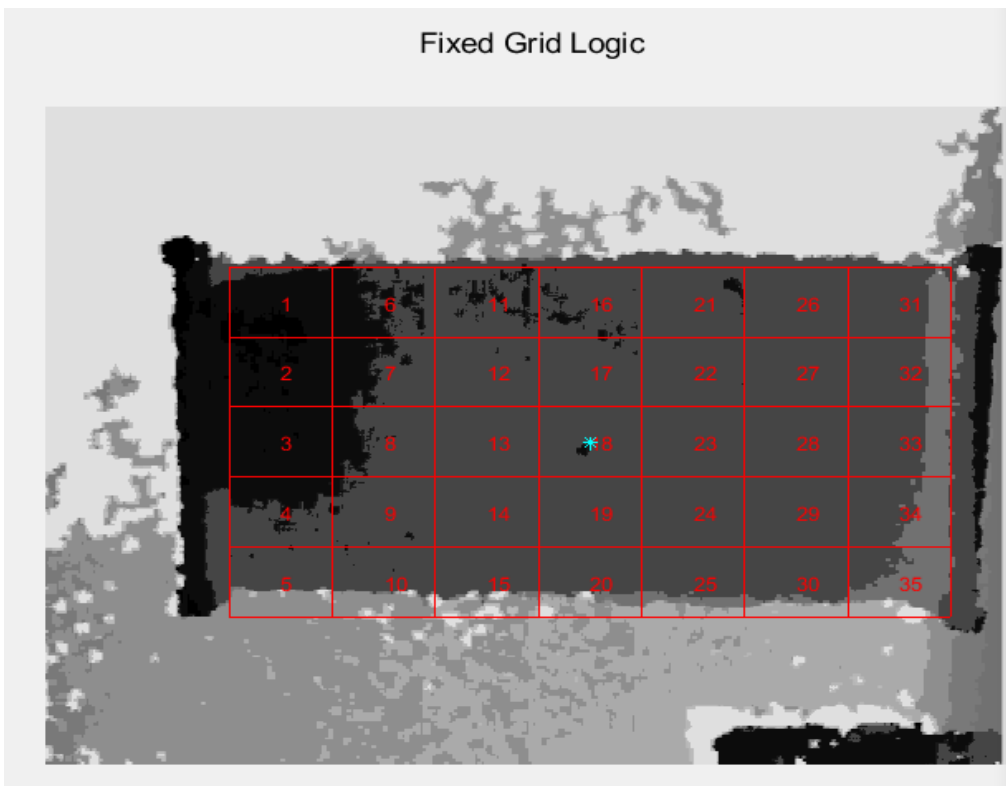


Figure (4G) shows the region of interest split into fixed grids of fixed size from centroid until edge of boundary.

4.4.2 Varying Grids generation algorithm

In this method, the number of width and height segments needs to be specified as input parameters, and the algorithm draws grids by evenly dividing the region of interest by the specified width and height parameters. As seen in Fig. (4H), this algorithm ensures that the entire region gets covered and grids get divided evenly based on the input parameters given. This is done by the function named **even_grid_logic.m**.

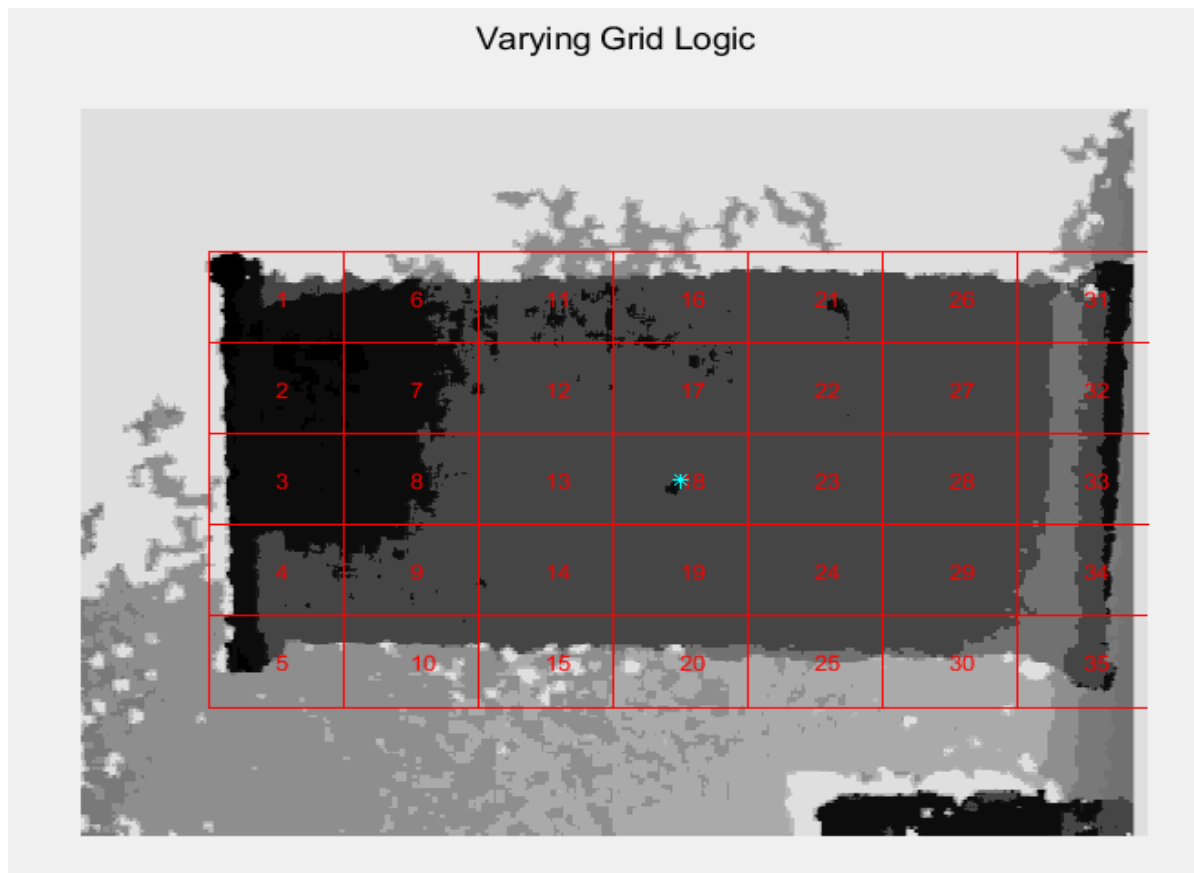


Figure (4H) shows the region of interest split into evenly spaced grids of varying size based on number of segments of width and height.

4.5 Detecting common grids based on thermal signature

We then run the algorithm to select the grids areas that correspond to the body area on the bed. This is done by thresholding the thermal signature, and superimposing the grid on the bed area. As seen in Fig. (4I) for fixed grids and Fig. (4J) for varying grids, the grids that have a higher thermal

measurement superimposed would be selected. This helps save computational resources by checking only grids where the body of the person is present and skipping the grids where the body is not present. This is done by the function named **thermal_grid.m**.

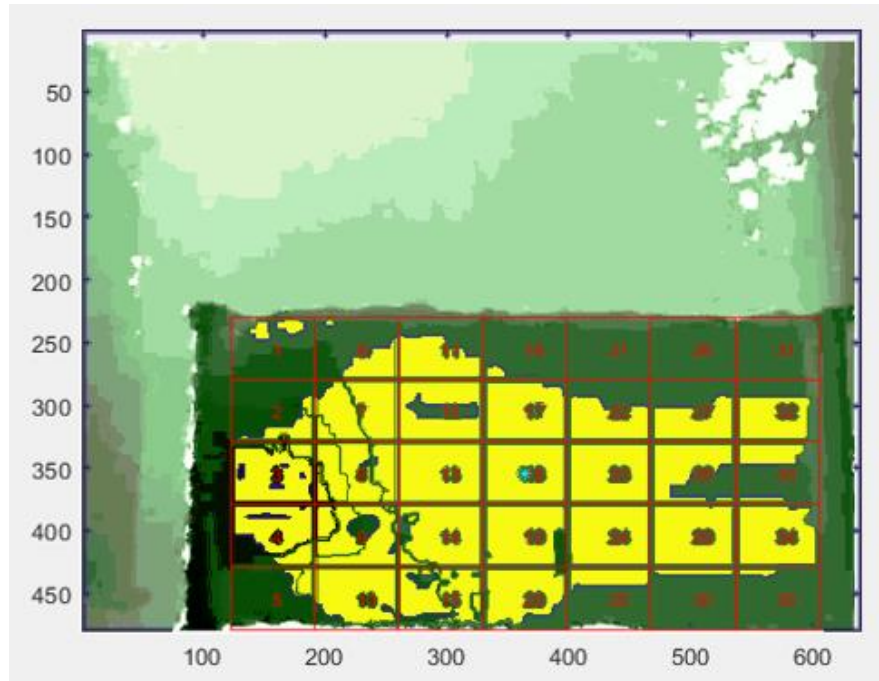


Figure (4I) shows the thermal image of the person superimposed on fixed grids, and only the grids having the thermal signature would be computed.

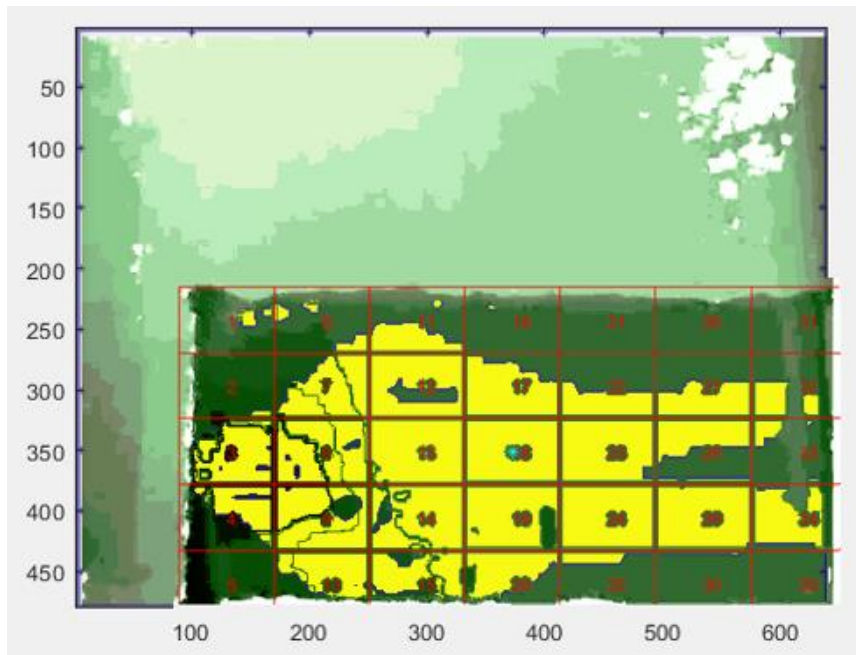


Figure (4J) shows the thermal image of the person superimposed on varying grids, and only the grids having a higher thermal measurement would be selected for respiration computation

4.6 Extraction of Respiration variation

Histogram stretching is the process of stretching the minimum and maximum value of the image to the minimum and maximum limit of the image data type supported format respectively. This is done by the function named **Est_respiration_kinect.m**.

If we have a given image, whose input intensity values I_{in} are in between a and b , and the enhanced image whose maximum range of values are in between c and d , then Output intensity I_o is given by equation (1)

$$I_o = \frac{(I_{in} - c)(b - a)}{d - c} + a$$

This method of histogram stretching the values works well for the depth data, and enhances the sensitivity of the camera.

We manually select the range of values to vertically crop the depth frame, so that the region of interest as the area around the chest, where the respiration activity takes place.

In order to compute the respiration variation, we take the average of all the values in a depth frame. The average value of a depth frame is given by equation (2)

$$Average = 1/n \sum_{k=1}^n i_k$$

where i is the depth value of the k^{th} position and n is the number of pixels in the frame.

Algorithm 1 Algorithm for depth frame enhancement
Input: Depth data sequence
Output: unfiltered respiration waveform
Initialization:
1.Import depth data sequence
LOOP Process
2.for length of depth data sequence do
3.histogram enhance depth frame
4.crop depth frame
5.Histogram enhance depth frame
LOOP Process
6.for length of depth data sequence do
7.compute average value of frame
8.return range of average depth frame values

Table (4C) shows the algorithm for respiration variation detection

Fig. (4K), (4L) and (4M) shows the raw waveform obtained from the depth data. Video of algorithm at work, with raw waveform, 2D depth frame, 3D depth frame, is given below.

<https://missouri.box.com/s/8gr8b3qrq8q7frmdpqxmq1snpa17wsg>

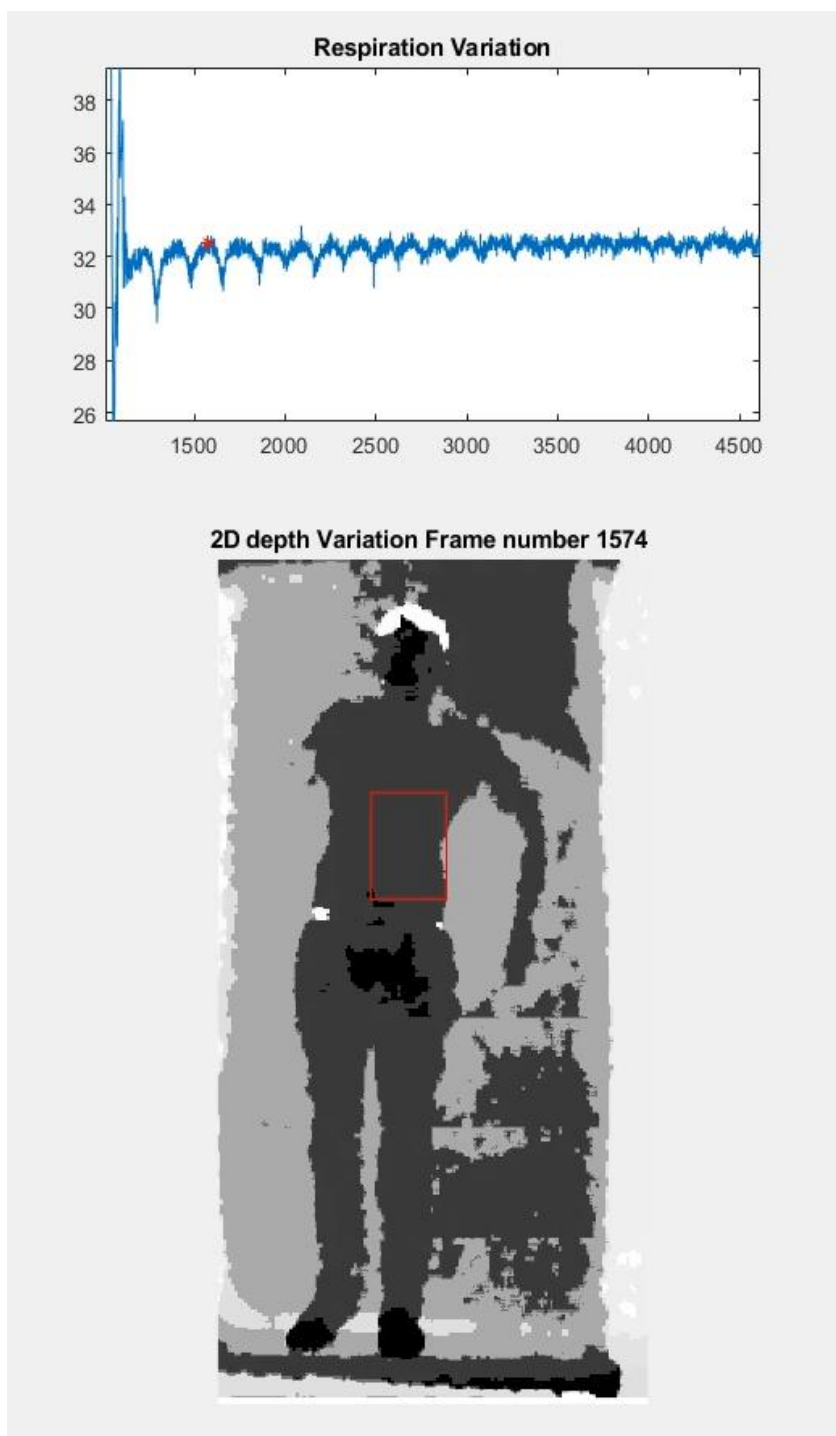


Figure (4K) shows the raw respiration waveform obtained by the algorithm from the red grid area.

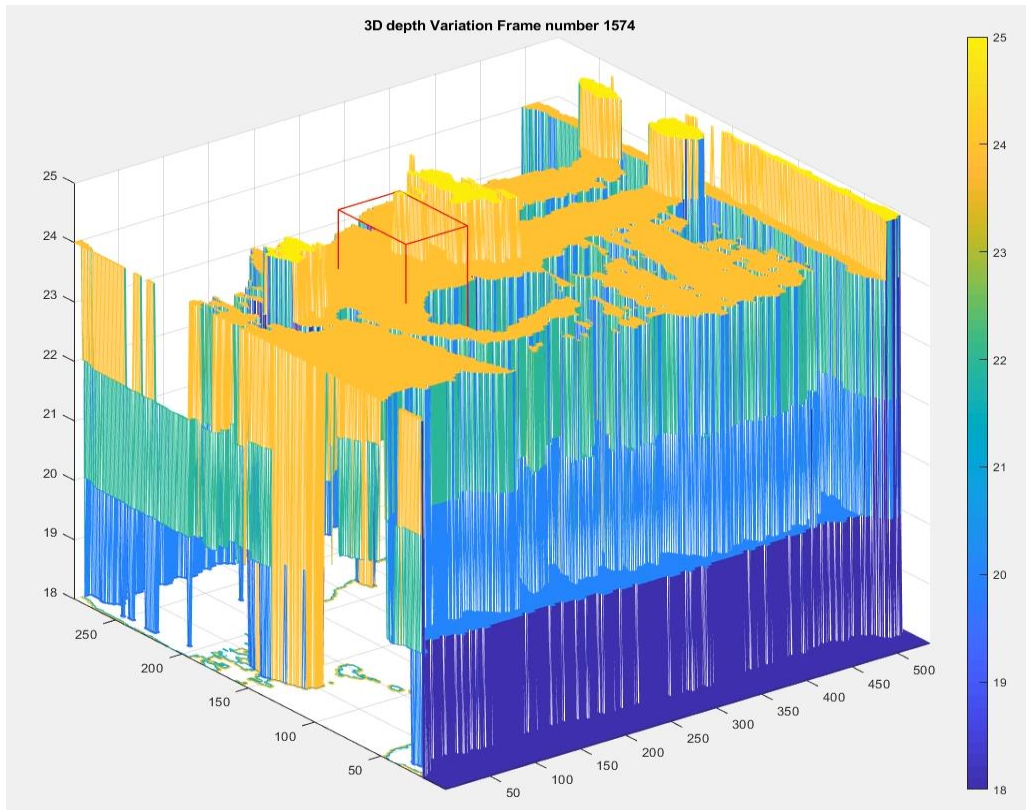


Figure (4L) shows the three dimensional variation for the red grid area.

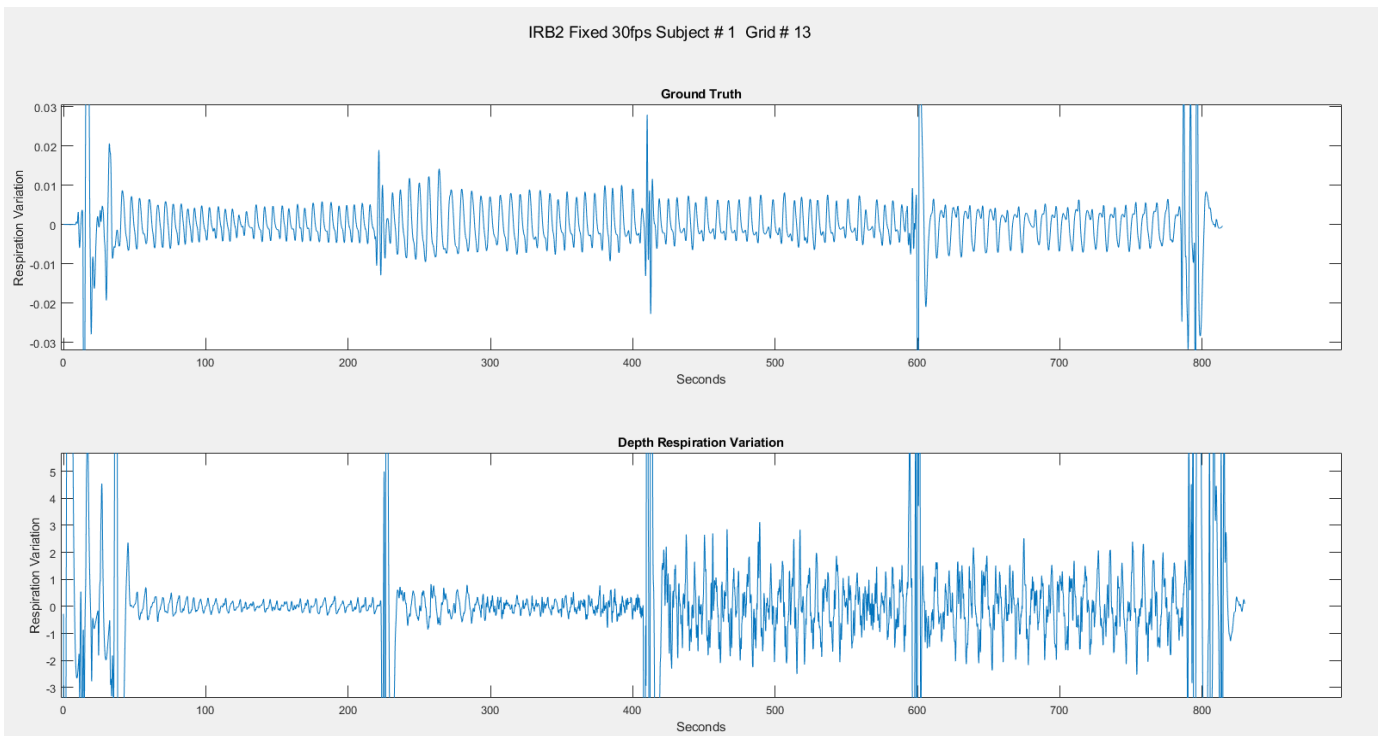


Figure (4M) shows the ground truth on top, and the filtered respiration variation from the algorithm below. The abrupt transitions are due to the body movement when changing posture between supine, left lateral, right lateral and prone.

4.7 Separation of Respiration and Restless body motion

The algorithm can separate prominent restless body movement with the respiration from the raw waveform based on isolating outliers which are quartiles based on a certain threshold value. We are also able to compute the % of restless body movement, along with the respiration and restless body movement waveform. This is done by the function named **seg_signal_grid.m**. Note that this function was not used for the test results reported in Chapters 6 and 7; rather, the restlessness segments due to posture changes on the bed were manually segmented

The function below performs the automatic segmentation of respiration from the measure depth data signal, separating out the major restlessness segments:

Respiration waveform =
`filloutliers(Filtered waveform,0,'quartiles','ThresholdFactor',ths_fac);`

The parameter `ths_fac` was chosen to be 0.5.

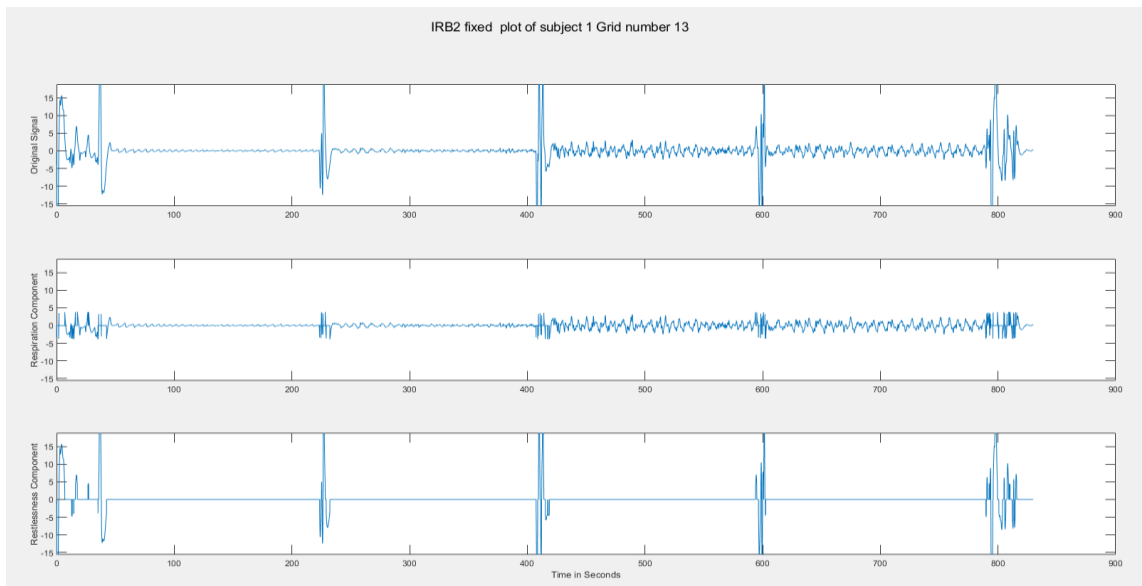


Figure (4N) shows the raw signal on the top, the respiration variation in the middle, and the restless body movement component below.

4.8 Splitting of respiration signals into Supine, Left Lateral, Right lateral, Prone

As part of the IRB2 experiment, we conducted systematic trials, wherein the person started the trial by being on the supine position, followed by left lateral shoulder, followed by right lateral shoulder, and finally the prone position. With this assumption, the four longest signals from the respiration component was computed, and accordingly, classified as supine, left lateral, right lateral and prone. This is done by the function named **split_position.m**.

4.9 Selection of the best signal from the grid of signals

In order to select the best signal from the entire grid of signals, we process the signals and compute certain parameters based on few algorithms, and then sort the returned score for each signal in order to select the best signal. Parameters 4, 5, 6 & 7 (described below) were used for the calculation; parameters 1, 2 and 3 were considered and tested but not used because they were not effective in selecting the best grid. This is done by the function named **select_best_sig_seg.m**. As seen in Figure (4O), for subject #16, grid 13 is the best, followed by grid 12. The highest from either parameter 6 or parameter 7 is considered, followed by highest of parameter 5, and highest of parameter 4, all sorted in descending order by Matlab.

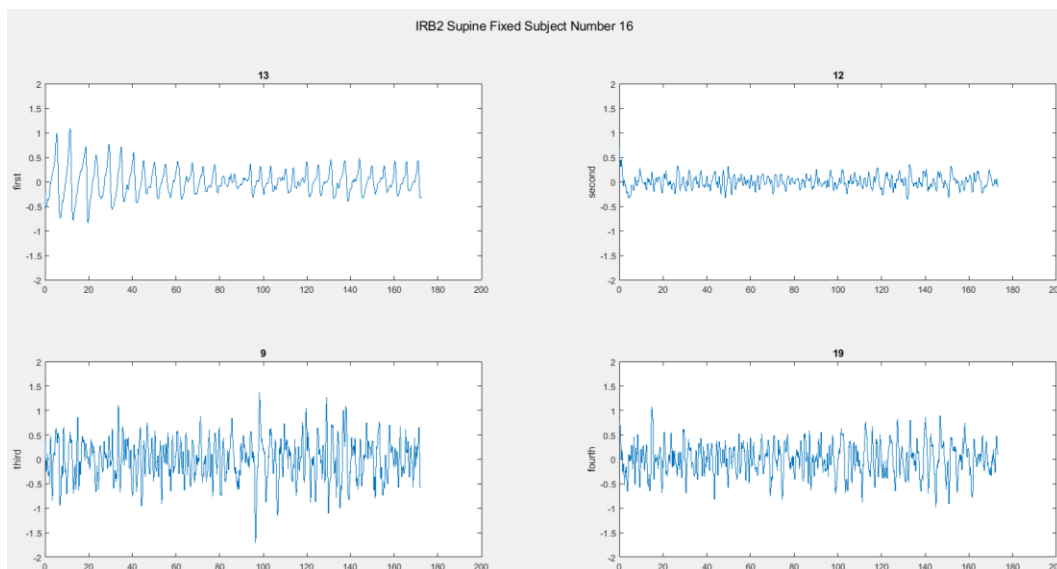


Figure (4O) shows the best signal algorithm selecting grid 13 for subject #16, based on parameters score.

4.9.1 Parameter 1 – **Signal Energy parameter:**

This parameter is defined as the difference between the mean of maxima and mean of minima. It gives us an estimate of the overall energy content in the signal.

$$\text{Signal Energy Parameter} = \text{Mean}(\text{Maxima}) - \text{Mean}(\text{Minima})$$

4.9.2 Parameter 2 - **Signal Variation factor:**

This parameter is defined as the ratio between the median of the difference of the moving max and moving min to the standard deviation of the difference of the moving max and moving min. The fixed window size is a parameter that can be predetermined, and should ideally be at least 15 seconds.

$$\text{Signal Variation Factor} = \frac{\text{Median}(\text{Moving_Range})}{\text{Standard_Deviation}(\text{Moving_Range})}$$

$$\text{Moving_Range} = \text{Moving_Maxima}[\text{Fixed_window_size}] - \text{Moving_Minima}[\text{Fixed_window_size}]$$

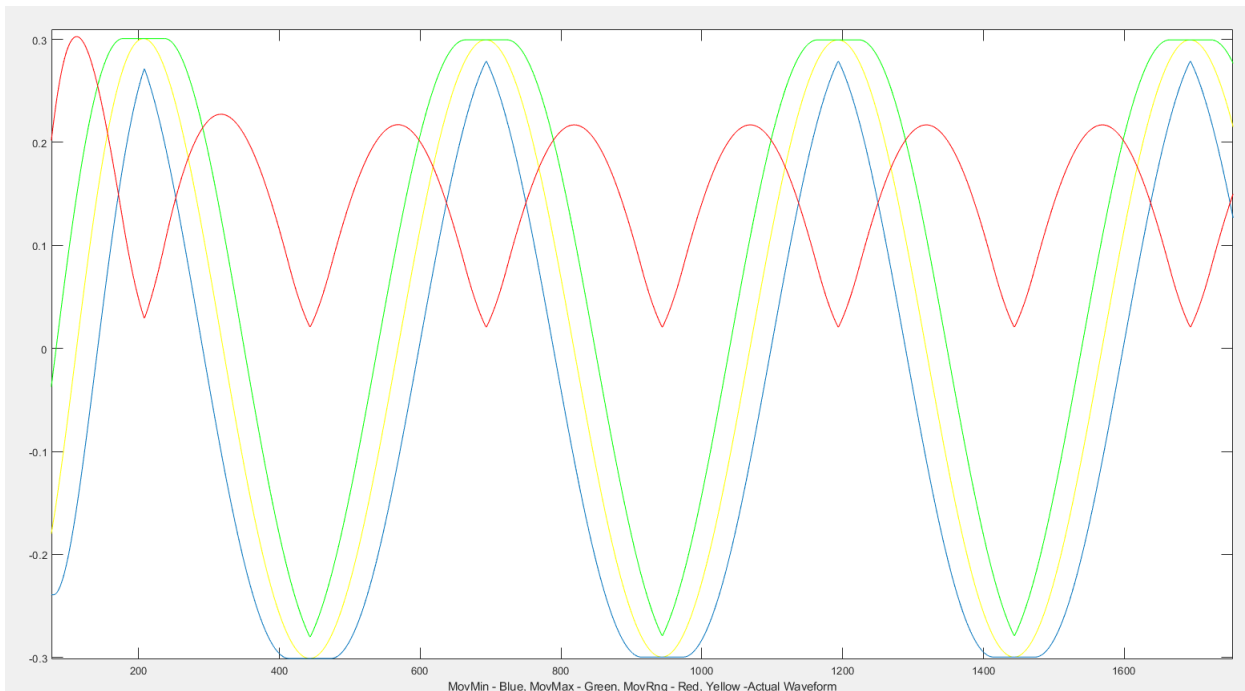


Figure (4P) shows the variation of the signal variation parameter for the signal in yellow, the MovingMin in blue, the MovingMax in Green, the difference between them in red.

4.9.3 Parameter 3 - **Signal Strength parameter**

This algorithm calculates the median of the peaks of the signal, giving us a value for the amplitude of the signal.

$$\text{Signal Strength parameter} = \text{Median}(\text{Maxima})$$

4.9.4 Parameter 4 - **Signal Symmetry parameter:**

This algorithm checks the number of maxima, and number of minima, and computes the score, based on the inverse of the ratio of the number of maxima to the number of minima subtracted from 1.

$$\text{Signal Symmetry parameter} = \frac{1}{1 - \frac{\text{Number of Maxima}}{\text{Number of Minima}}}$$

For maxima = minima, we get a score of infinity, shows symmetrical signal.

For maxima > minima, we get a negative response,

For maxima < minima, we get positive response.

Matlab is able to handle infinity, and the higher the score, the better is the signal.

4.9.5 Parameter 5 - **Signal Amplitude Variation parameter**

This algorithm computes the change in variability of the amplitude. Each deviation of amplitude from given range gets a certain score on the scale, from $-\infty$, -5000, -4000, -3000, -2000, -1000, -500, -100. No deviations equals a score of 1.

To compute this score, we find the difference between the subsequent respiration peaks, and find the subsequent difference between the above results. Based on the maximum and minimum value present in the second result, we score the signal based on a threshold, as the signal with high amplitude variation would have higher value in the second subsequent difference compared to a signal with low amplitude variation.

Signal Amplitude Variation Threshold

$$= \text{subsequent difference}(\text{subsequent difference}(\text{maxima of signal}))$$

4.9.6 Parameter 6 - **Signal to Noise Ratio of Maxima parameter**

This algorithm computes the signal to noise ratio of the signal for maxima peaks. It is defined by the ratio of the maxima peaks within a suitable respiration time period to all the maxima peaks. For ideal respiration signal, the ratio would be one, and less than one for noisy signal. For this calculation, we have considered the entire signal from one supine. Left lateral, right lateral or prone position.

$$\text{Signal Noise Ratio of Maxima parameter} = \frac{\text{Number of Respiration Maxima}}{\text{Number of Maxima}}$$

4.9.7 Parameter 7 - **Signal to Noise Ratio of Minima parameter**

This algorithm computes the signal to noise ratio of the signal for minima peaks. It is defined by the ratio of the minima peaks within a suitable respiration time period to all the minima peaks. For ideal respiration signal, the ratio would be one, and less than one for noisy signal. Fig. 4Q shows respiration signal maxima peak detection, and Fig. 4R shows peak detection for all maxima in the signal. For this calculation, we have considered the entire signal from one supine. Left lateral, right lateral or prone position.

$$\text{Signal Noise Ratio of Minima parameter} = \frac{\text{Number of Respiration Minima}}{\text{Number of Minima}}$$

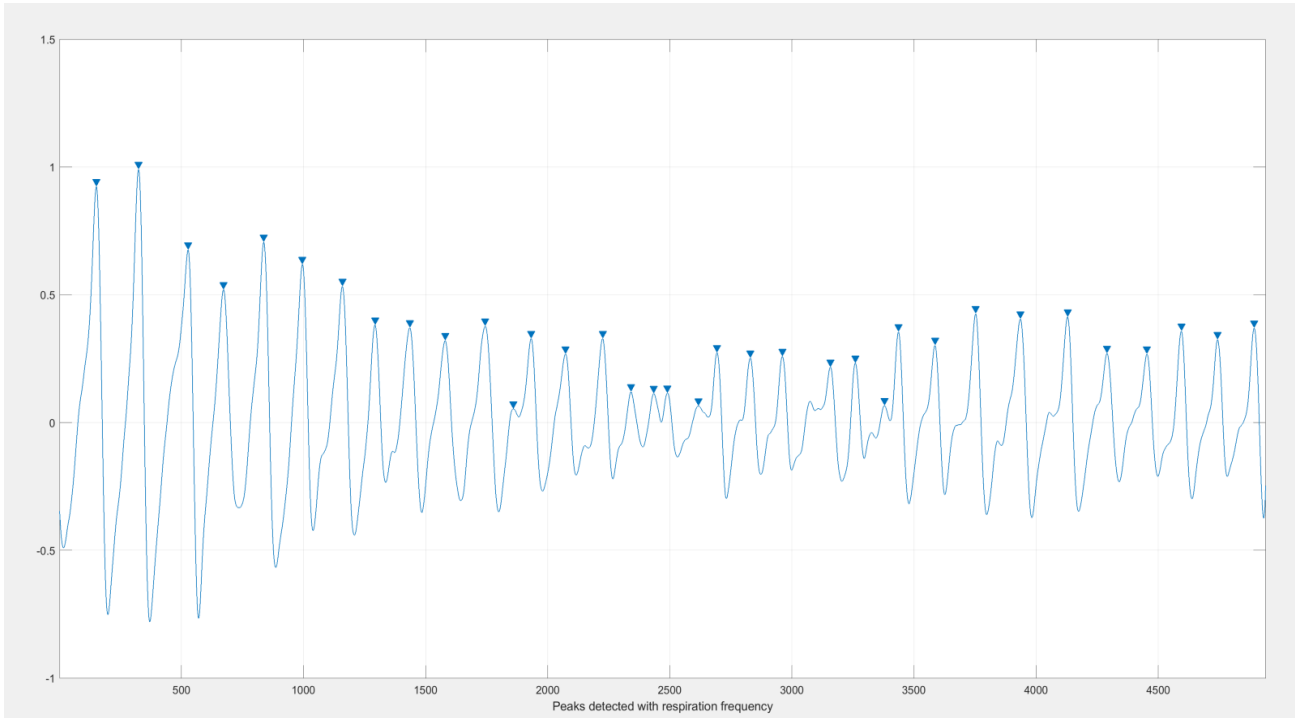


Figure (4Q) shows the peak detection for peaks within the respiration frequency.

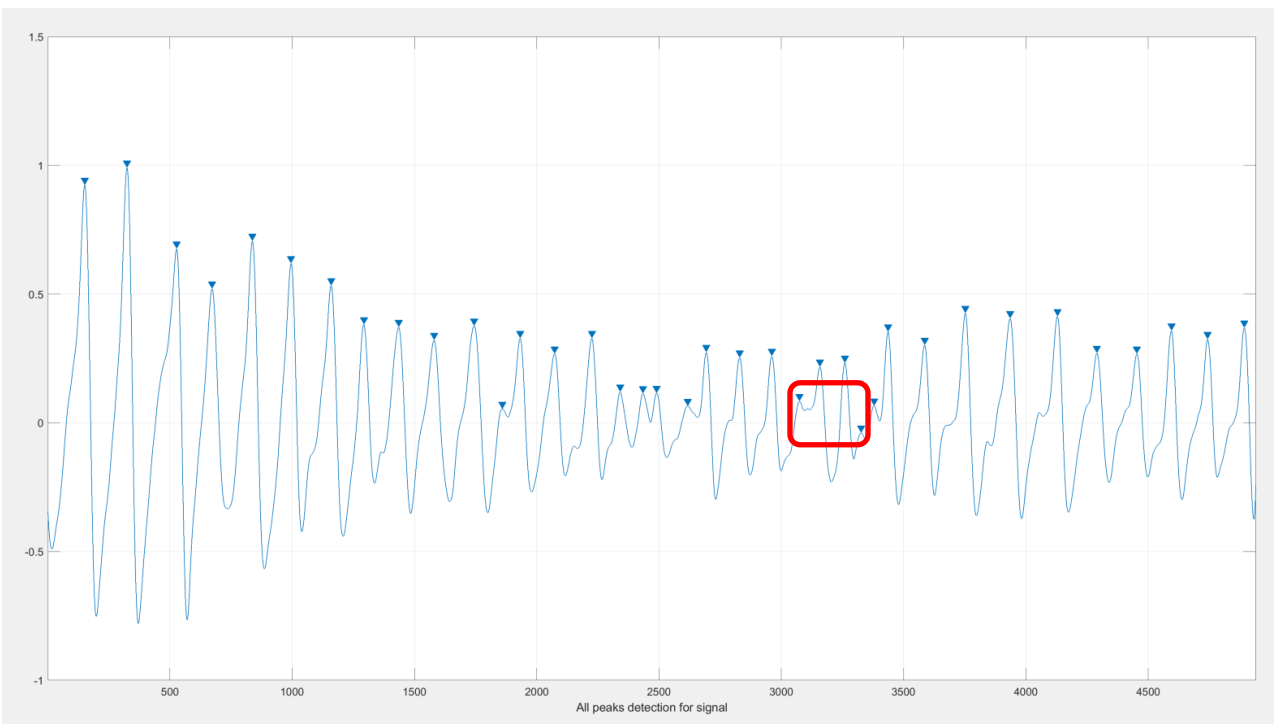


Figure (4R) shows the peak detection for all the maxima in the signal, the extra maxima detected has been highlighted in red.

4.10 Computing Respiration rate for given grids based on peaks detected

One of the methods of computing the respiration rate is based on detecting the peaks in the respiration signal. Based on millisecond time frame accuracy, the floating point sampling frequency of the signal is computed. After computing the precise sampling frequency, and having the length of the signal, we then count the number of respiration peaks present using MATLAB findpeaks function with tuning parameters to pick out peaks within respiration frequency, and estimate the respiration frequency, as seen in Fig. (4S).

$$\text{Peak Respiration Rate in B.P.M} = \frac{\text{Number of Peaks} * \text{Sampling Frequency} * 60}{\text{Length of signal}}$$

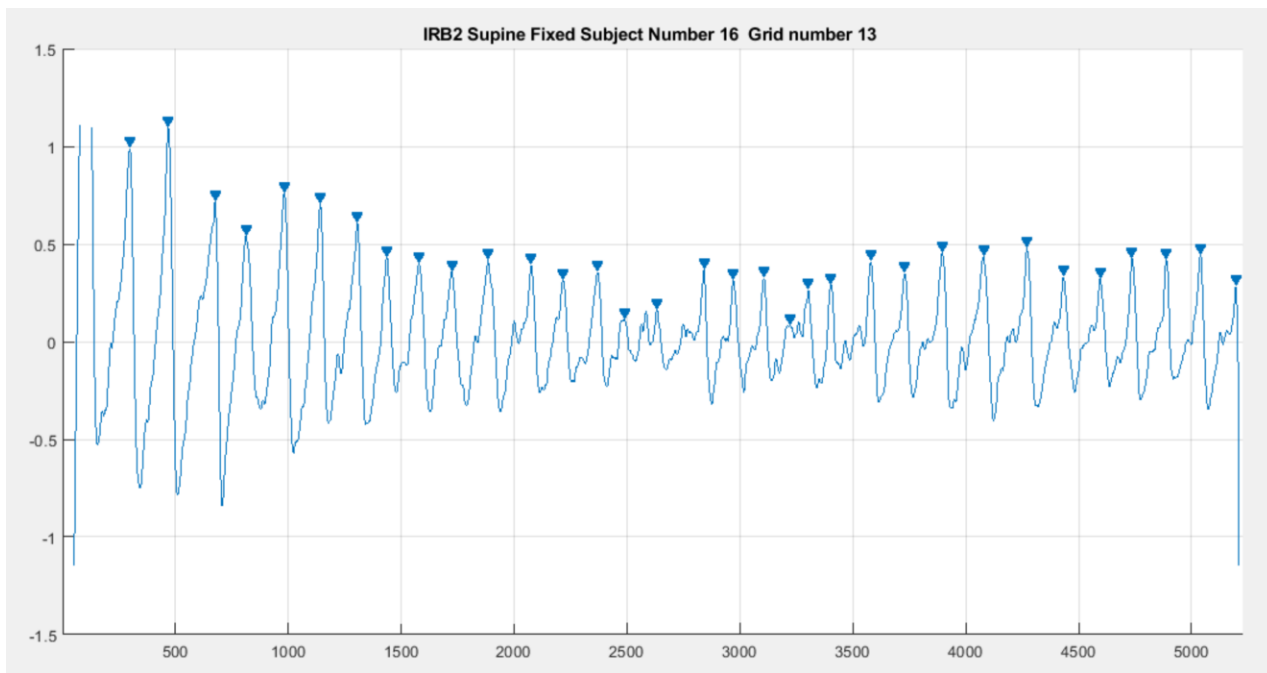


Figure (4S) shows the peak detection for all the respiration maxima in the signal, which would then be used to estimate respiration rate.

4.11 Computing Respiration rate for given grids based on Fourier Transforms

The other method of computing the respiration rate is based on checking the peak frequency from the Fourier transform of the signal. The overall frequency of the signal is computed based on averaging the frequencies which are 90% and above the peak frequency.

$$\text{Fourier Respiration Rate in B.P.M} = \frac{1}{n} \sum_{i=1}^n \text{Frequencies}_i \in \{\text{Frequencies}_i \geq 0.9 \text{Frequency}_{peak}\}$$

4.12 Plotting algorithms

As part of plotting the results, a few scripts had to be run in order to extract the ground truth, generate the manually segmented ground truth, generate the manually segmented respiration signals for peak detection and FFT respiration rate algorithm performance. Once the variables had been generated, the graphs had been plotted from the grid signals with few other scripts.

4.13 Grid Size SNR computation

As part of selecting the optimal grid sizes, the Signal to Noise Ratio maxima algorithm was run on the central grids for the three variable grid sizes. The SNR value 1 shows the optimal grid size selected of width 68 pixels and height 51 pixels. The SNR value 2 is for a slightly bigger grid of width 80 pixels and height 60 pixels, and the SNR value 3 is for a slightly smaller grid of width 60 pixels and height 45 pixels. As seen in Fig. 4T for IRB1 and Fig. 4U for IRB2, the dark green shows normalized grid area, and the SNR value 1 in red, SNR value 2 in blue and SNR value 3 in light green is scaled up to magnify the differences, and we can see that initial grid size is optimal.

The working code for all the above algorithms can be found at

lewis.rnet.missouri.edu:/storage/htc/eldercare/data/projectdata/cameraRespRestless
<https://vcs.missouri.edu/CERT-Students/studentProjects/cameraRespRestless>

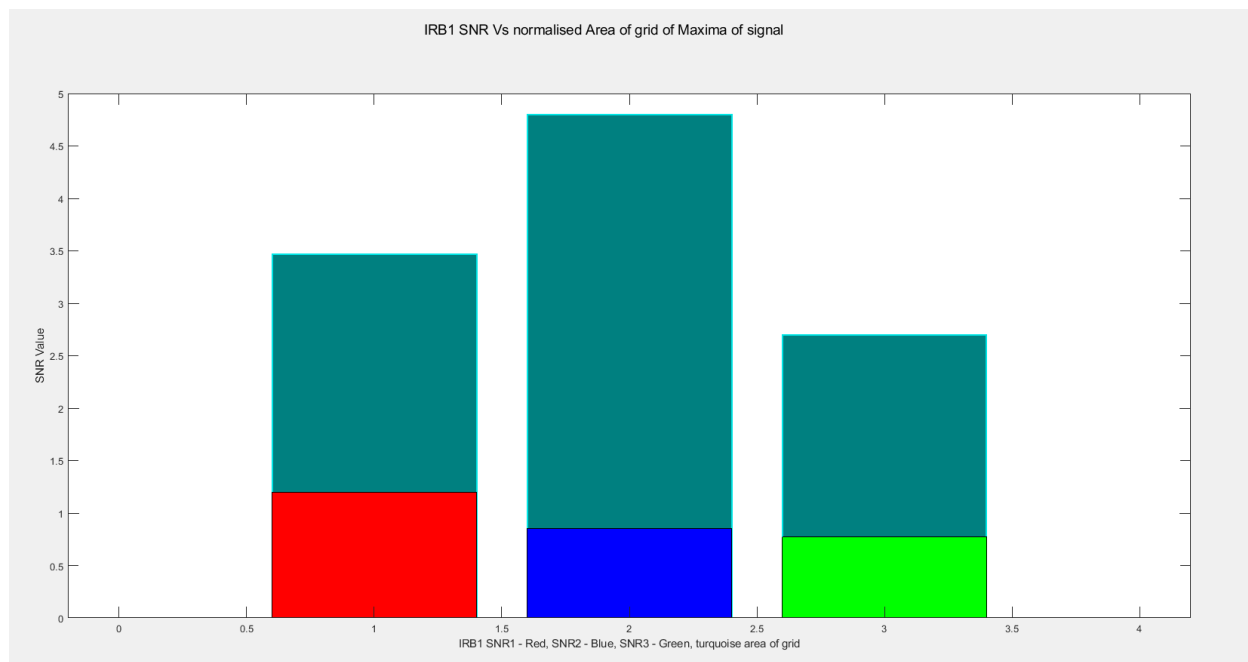


Figure (4T) shows the SNR variation depending on grid size for IRB1 trials. Dark green is grid area, red is SNR1 for grid size 68 x 51, blue is SNR2 for grid size 60 x 80, and green is SNR3 for grid size 45 x 60.

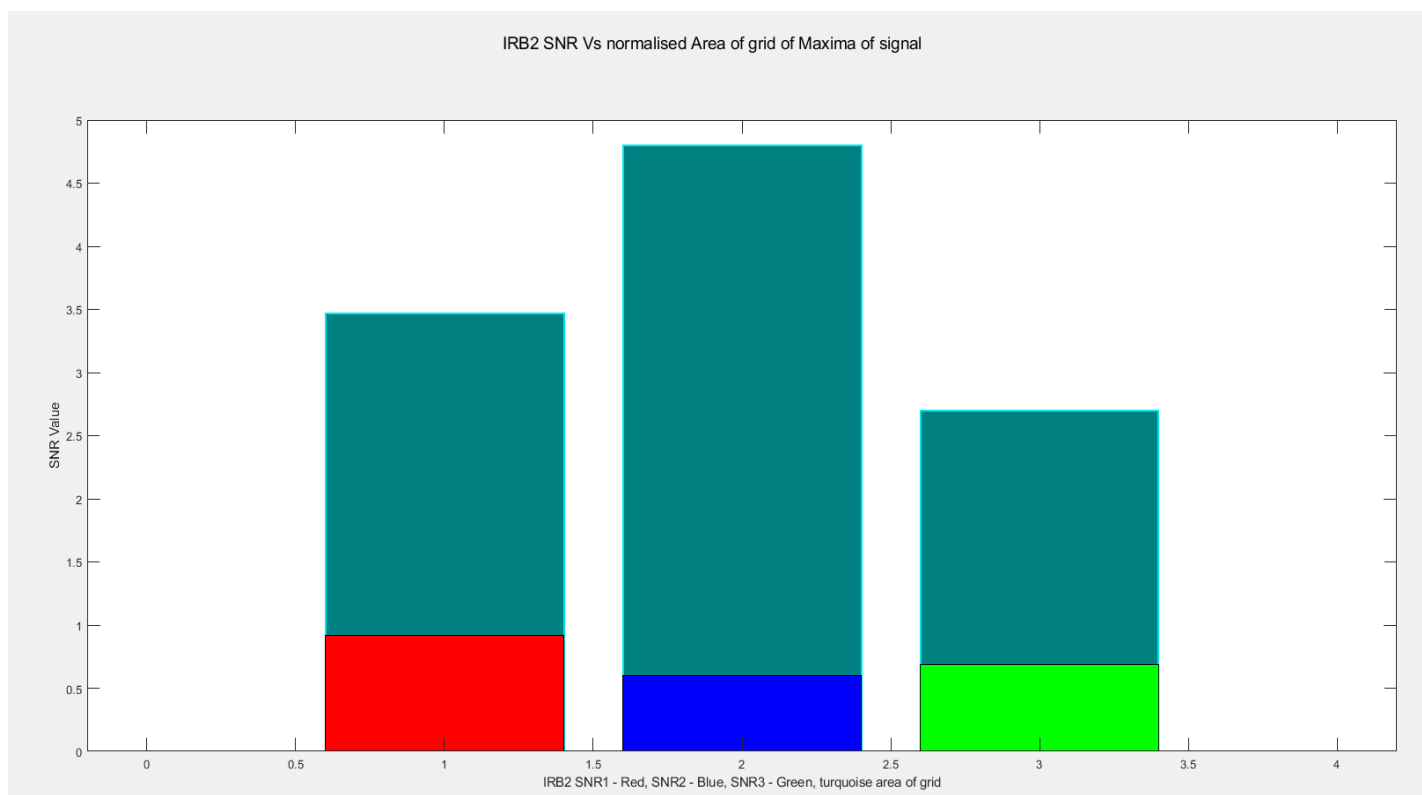


Figure (4U) shows the SNR variation depending on grid size for IRB2 trials. Dark green is grid area, red is SNR1 for grid size 68 x 51, blue is SNR2 for grid size 60 x 80, and green is SNR3 for grid size 45 x 60.

Chapter 5

Initial Results

5.1 Initial Trials

Initial trial runs consisted of the sensor facing a person sitting on the chair perpendicular to the ground plane. The person was seated at a distance of 56'' and 98'', or 1.23m and 2.15m respectively. The Foresite Healthcare DSK3 system captured the depth data with the resolution of 640 x 480, at 30fps. The below waveforms are raw and unfiltered, and obtained as described in section 4.6 of this paper.

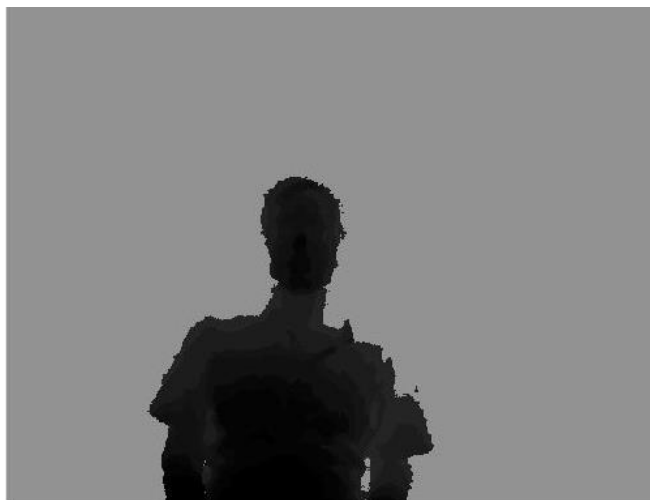


Figure (5A) shows person sitting at a distance of 56'' from the sensor

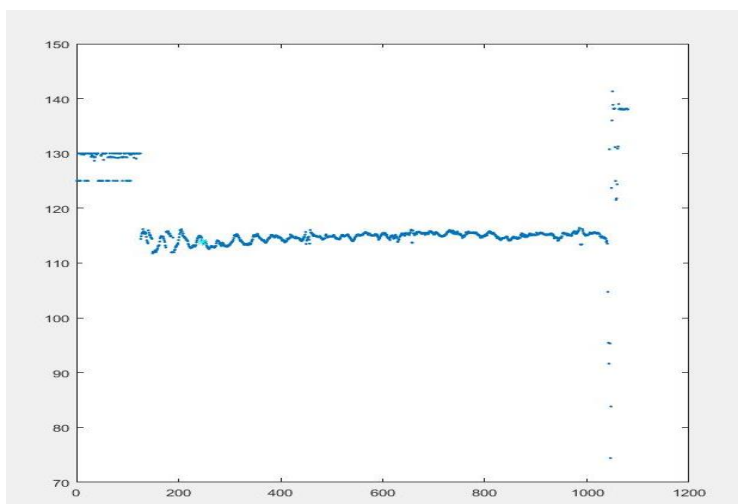


Figure (5B) shows respiratory waveform at a distance of 56'' from the sensor

We can see the rough respiration rate graph captured for each of the frame.



Figure (5C) shows person sitting at a distance of 98'' from the sensor

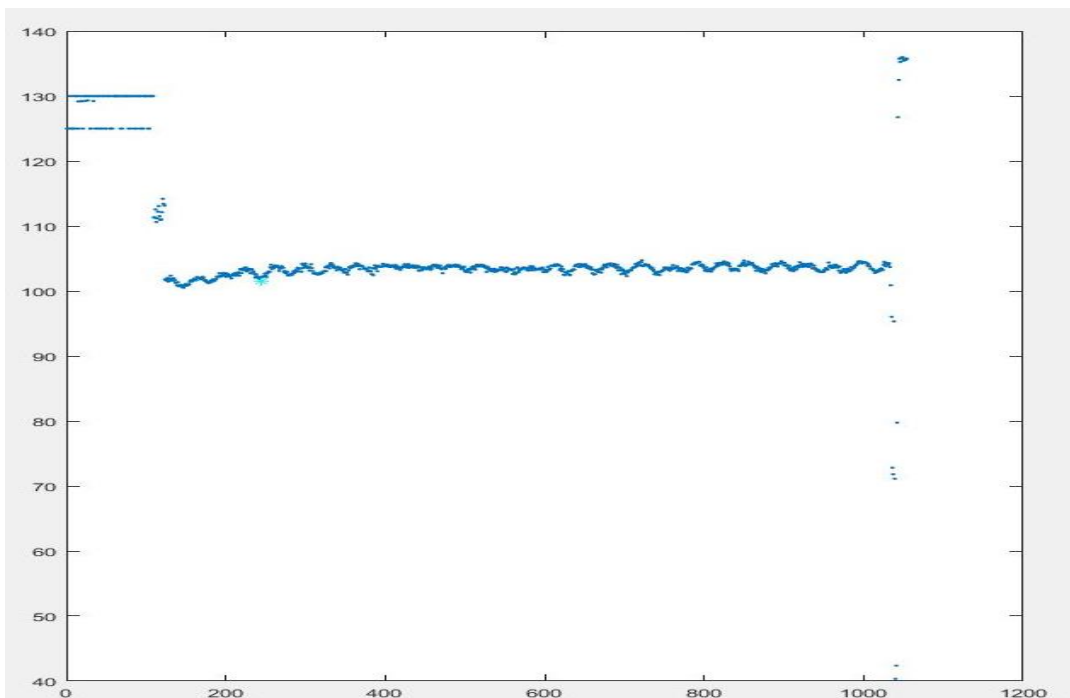


Figure (5D) shows person sitting at a distance of 98'' from the sensor



Figure (5E) shows the raw depth image of person sleeping on bed

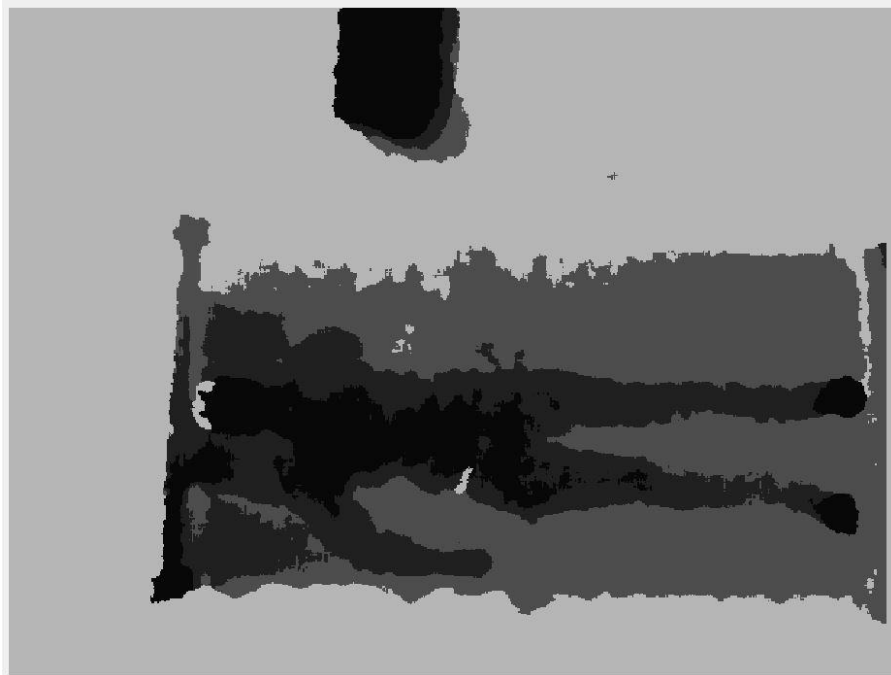


Figure (5F) shows the enhanced processed depth image of person sleeping on bed

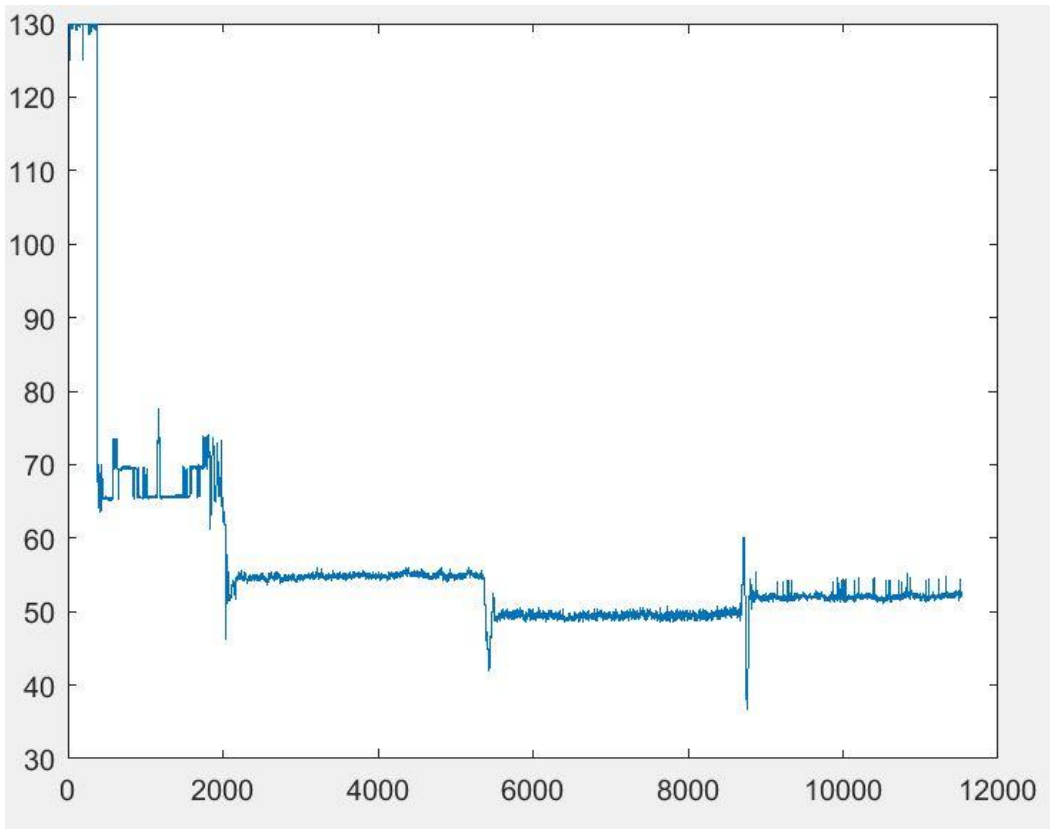


Figure (5G) shows the processed depth waveform for different positions on the bed

5.2 Subject 1 Trial 1

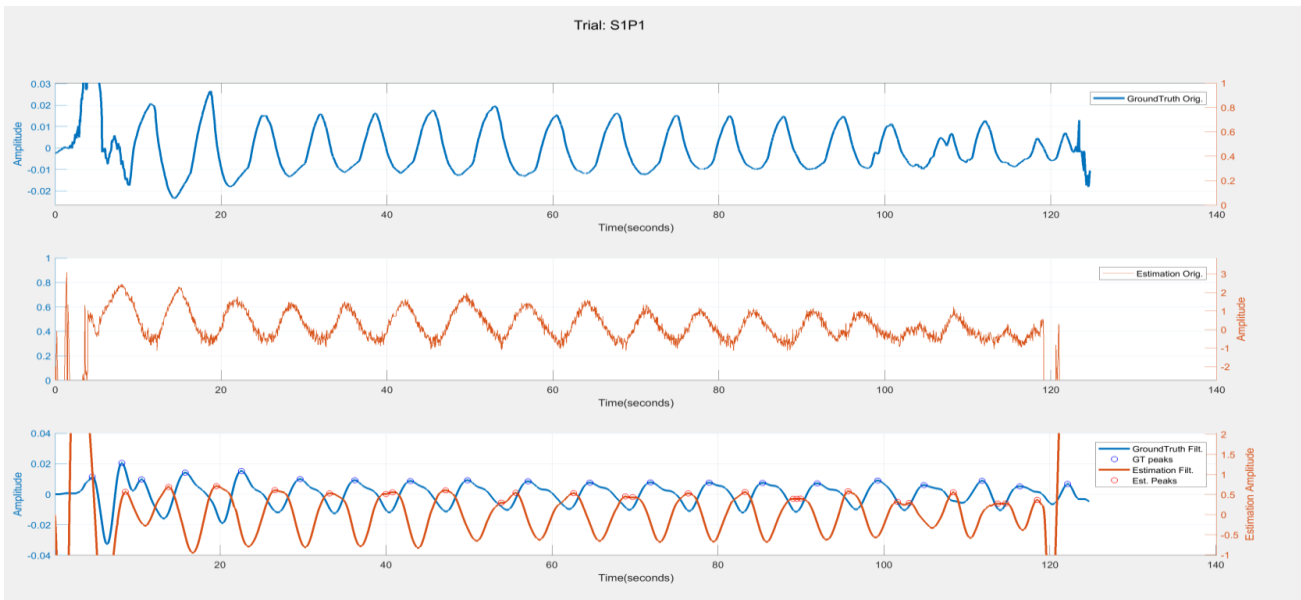


Figure (5H) shows the ground truth, followed by the unfiltered waveform and the filtered ground truth with filtered estimation for the supine position.

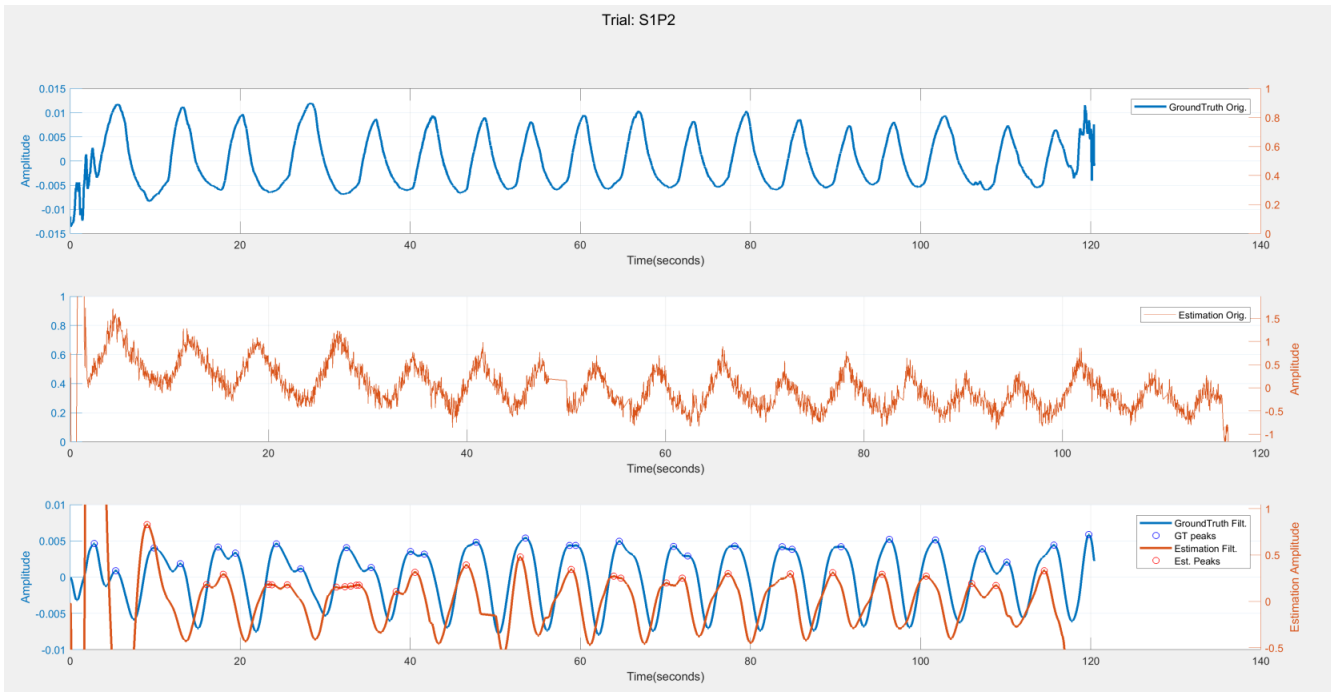


Figure (5I) shows the ground truth, followed by the unfiltered waveform and the filtered ground truth with filtered estimation for the left lateral position.

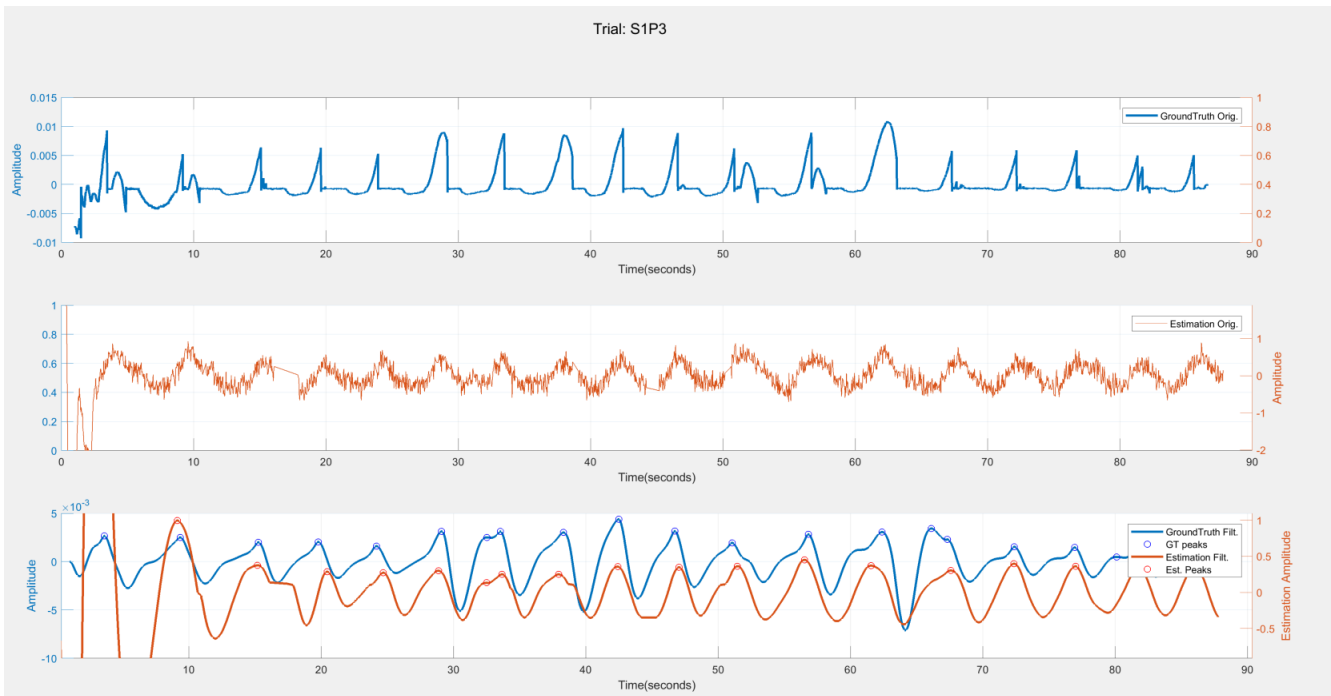


Figure (5J) shows the ground truth, followed by the unfiltered waveform and the filtered ground truth with filtered estimation for the right lateral position.

5.3 Subject 1 Trial 2

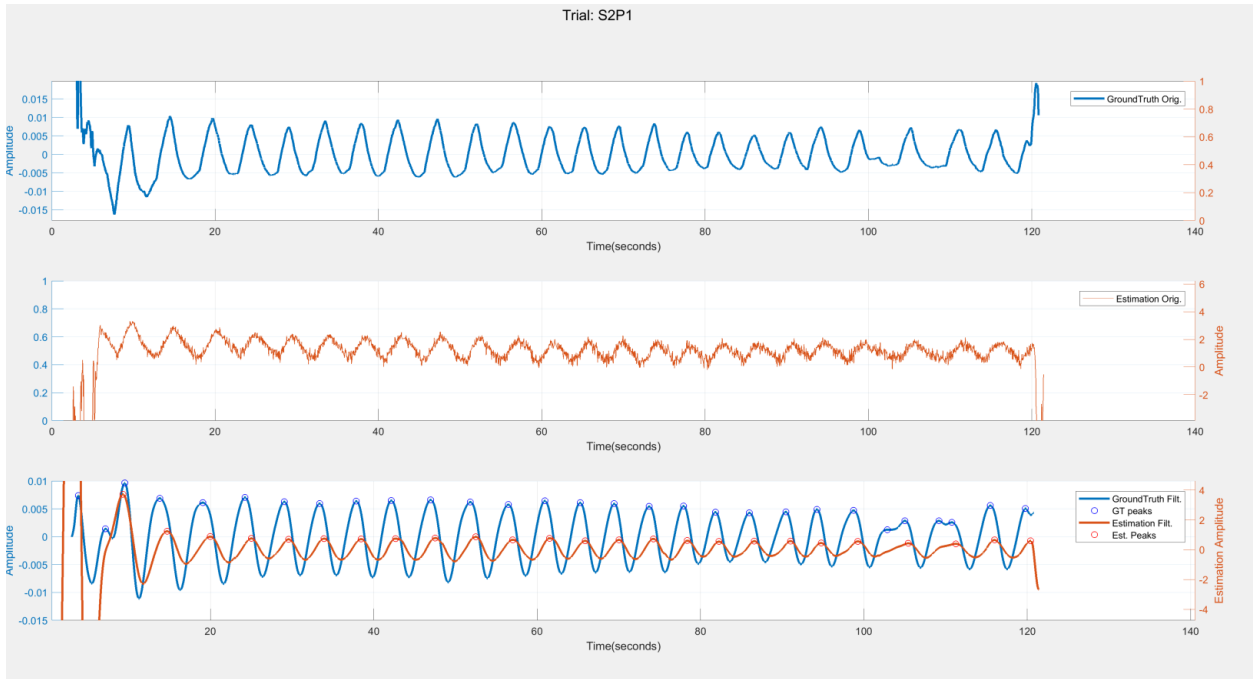


Figure (5K) shows the ground truth, followed by the unfiltered waveform and the filtered ground truth with filtered estimation for the supine position.

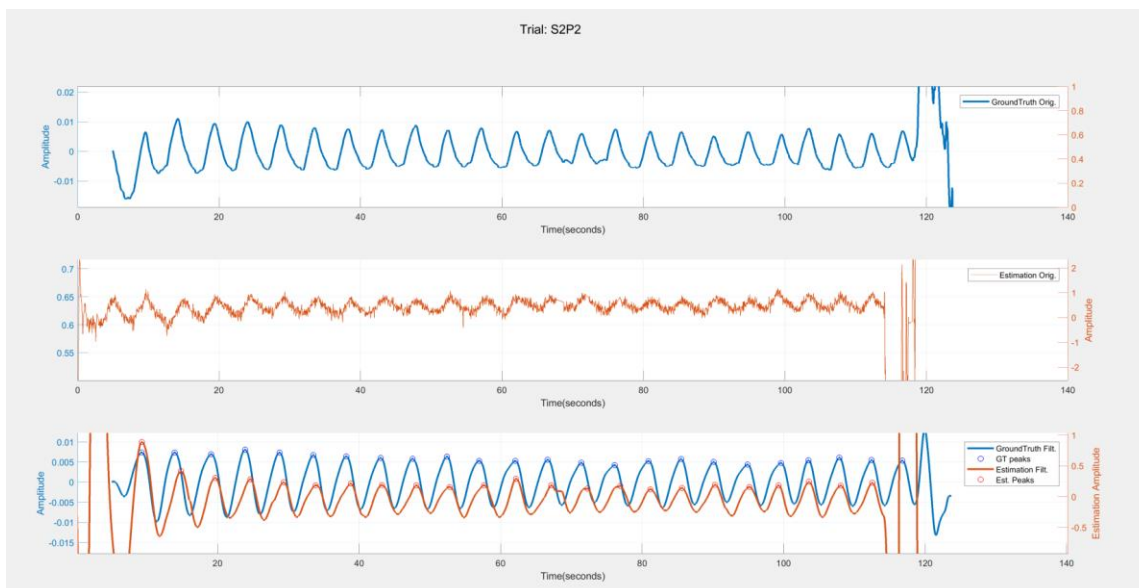


Figure (5L) shows the ground truth, followed by the unfiltered waveform and the filtered ground truth with filtered estimation for the left lateral position.

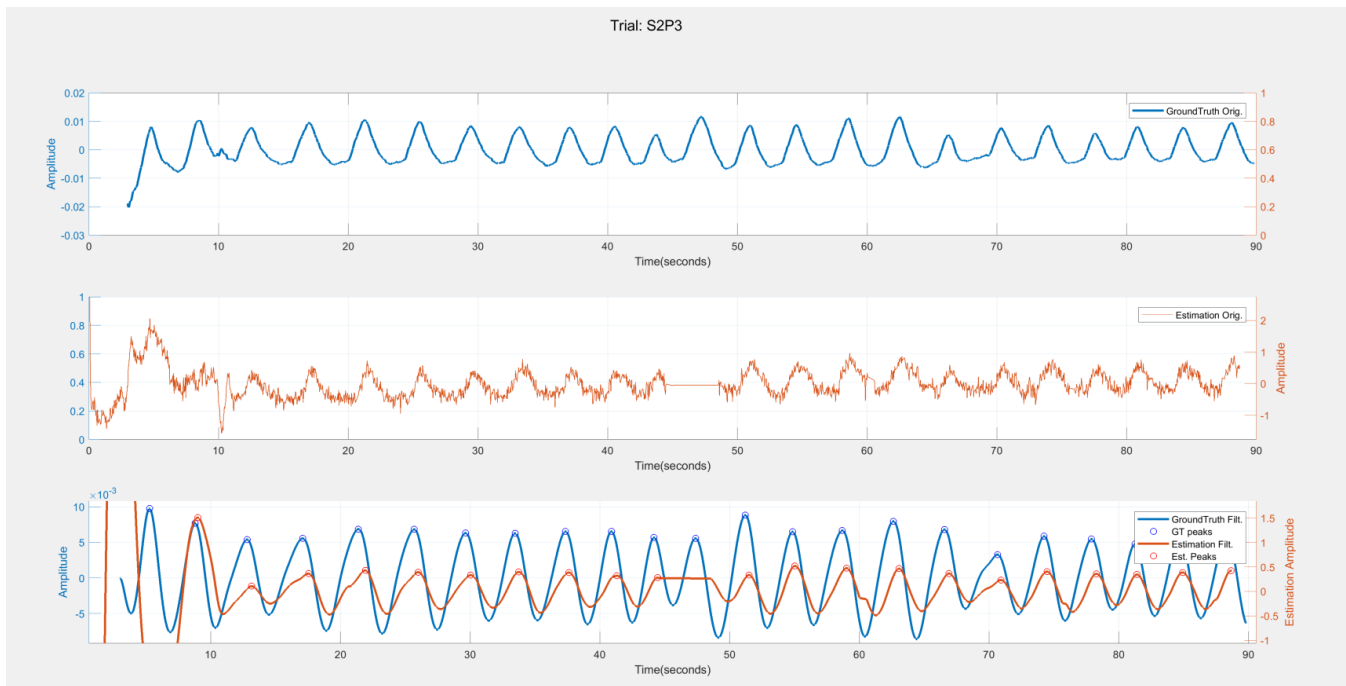


Figure (5M) shows the ground truth, followed by the unfiltered waveform and the filtered ground truth with filtered estimation for the right lateral position.

5.4 Subject 2 Trial 1

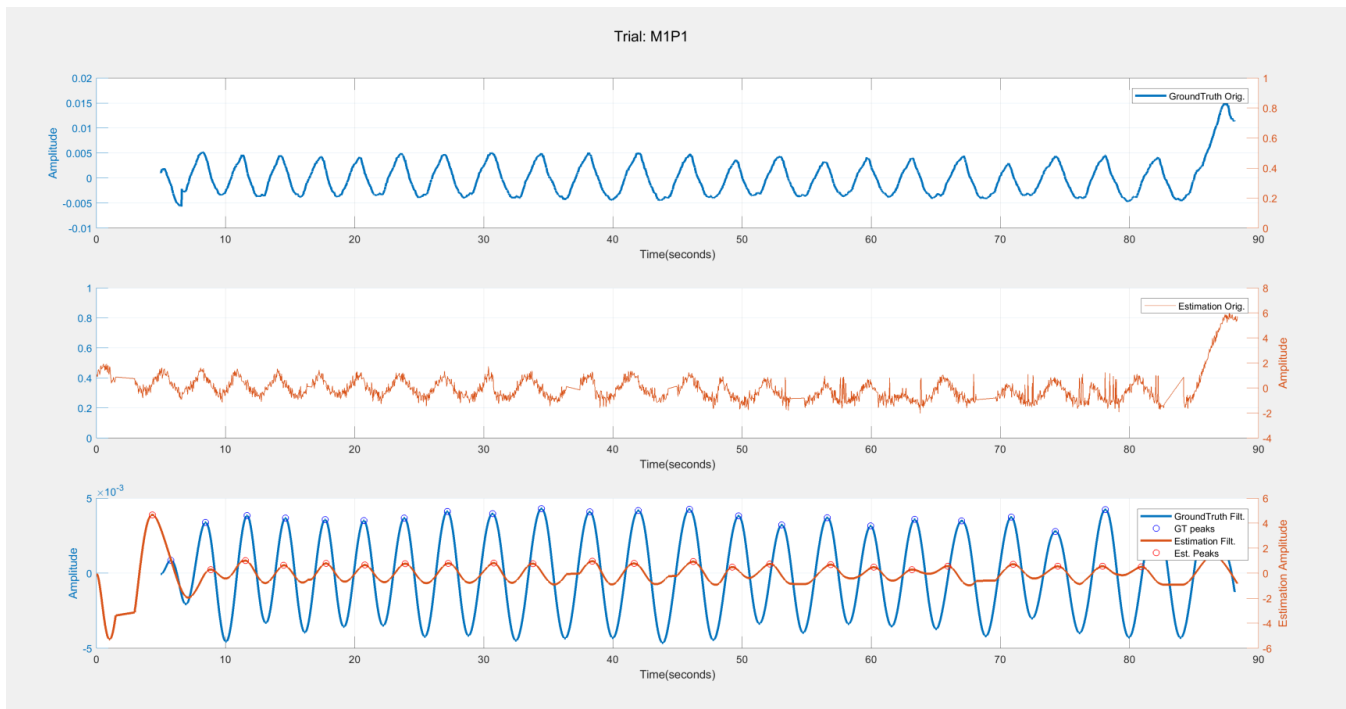


Figure (5N) shows the ground truth, followed by the unfiltered waveform and the filtered ground truth with filtered estimation for the right lateral position.

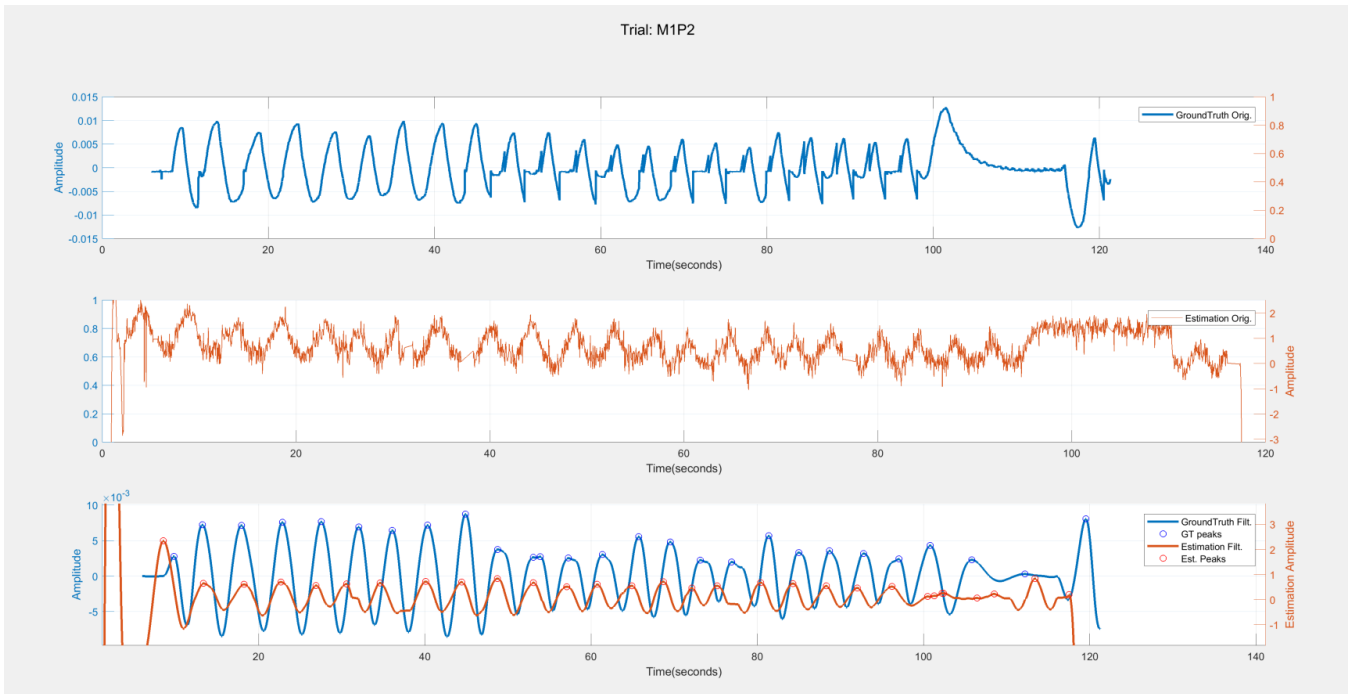


Figure (5O) shows the ground truth, followed by the unfiltered waveform and the filtered ground truth with filtered estimation for the left lateral position.

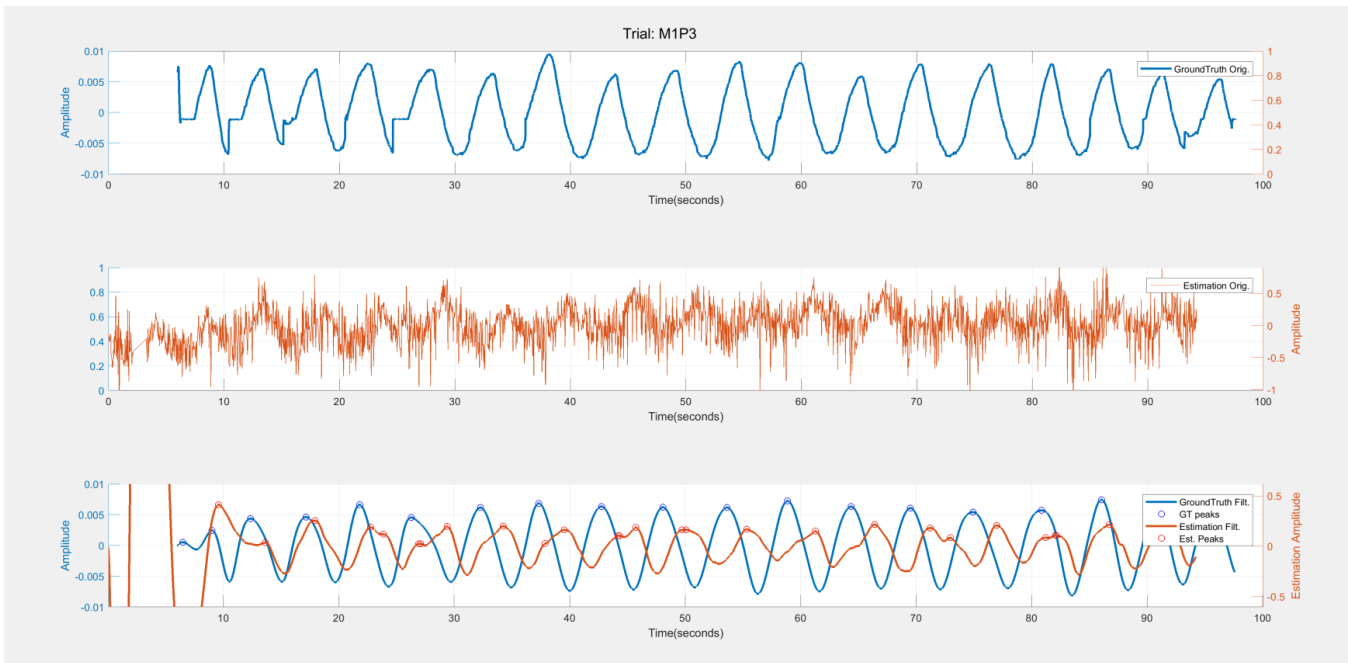


Figure (5P) shows the ground truth, followed by the unfiltered waveform and the filtered ground truth with filtered estimation for the right lateral position.

5.5 Subject 2 Trial 2

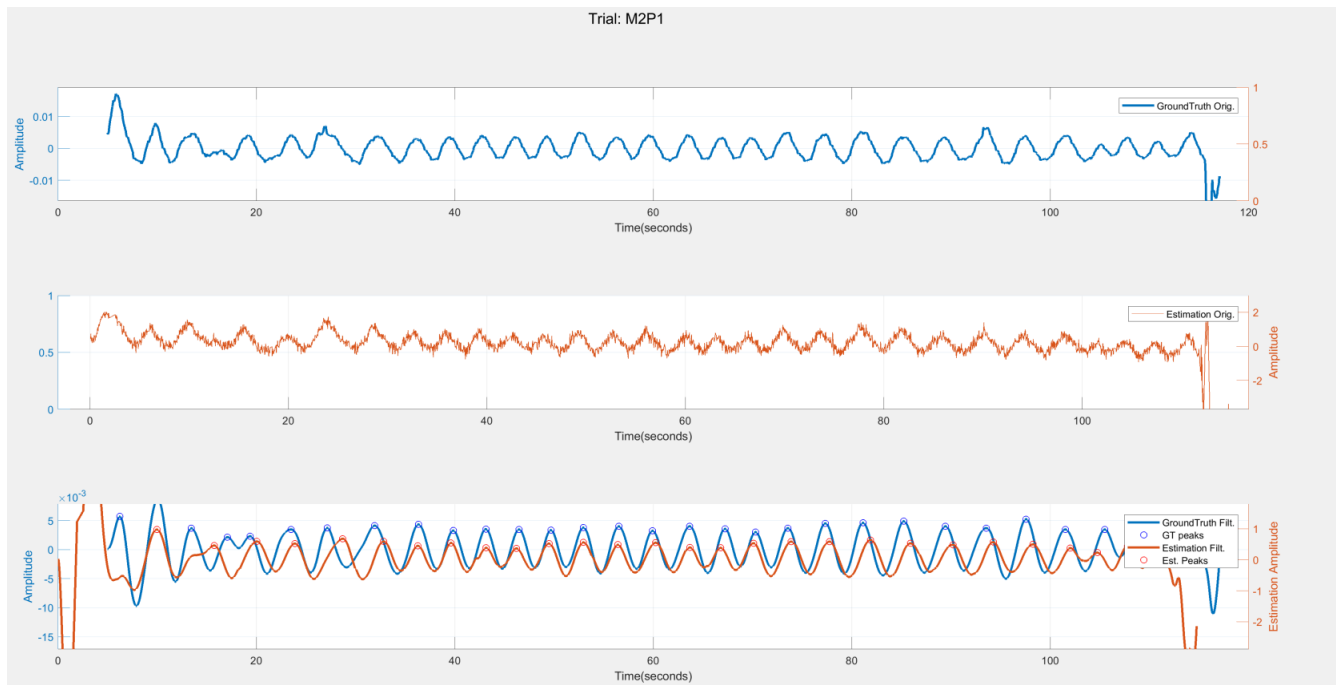


Figure (5Q) shows the ground truth, followed by the unfiltered waveform and the filtered ground truth with filtered estimation for the supine position.

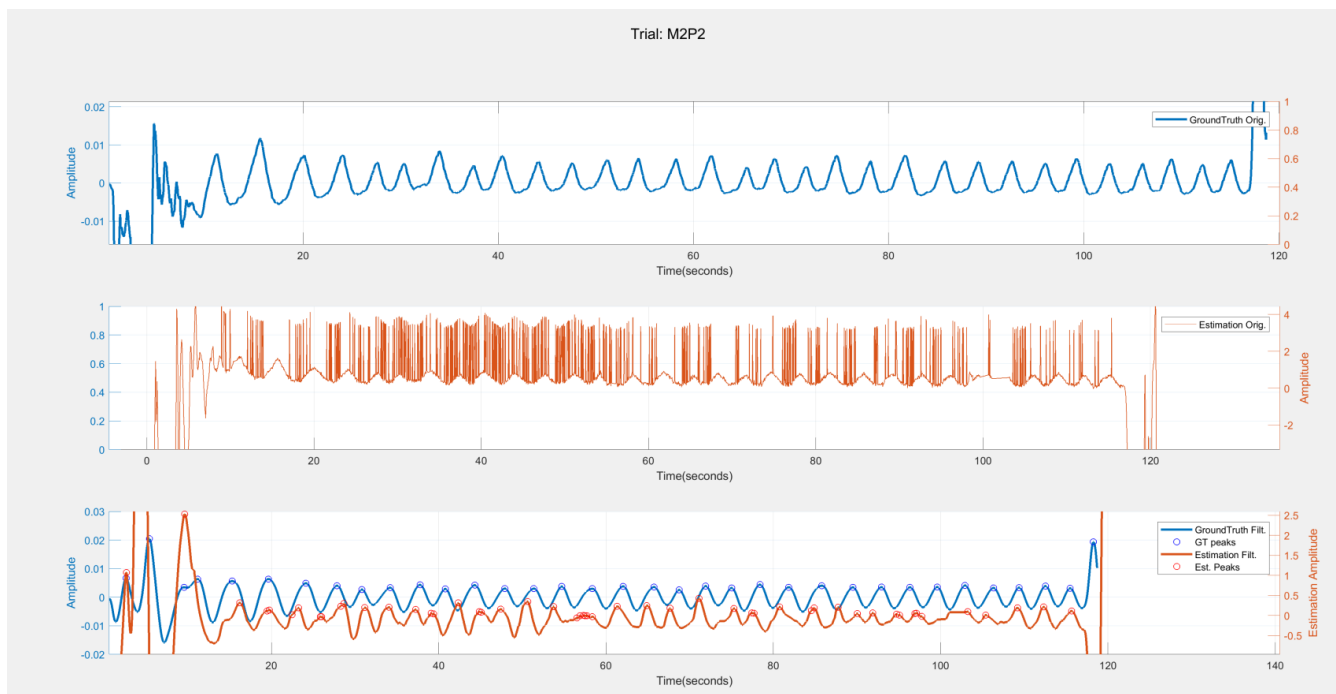


Figure (5R) shows the ground truth, followed by the unfiltered waveform and the filtered ground truth with filtered estimation for the left lateral position.

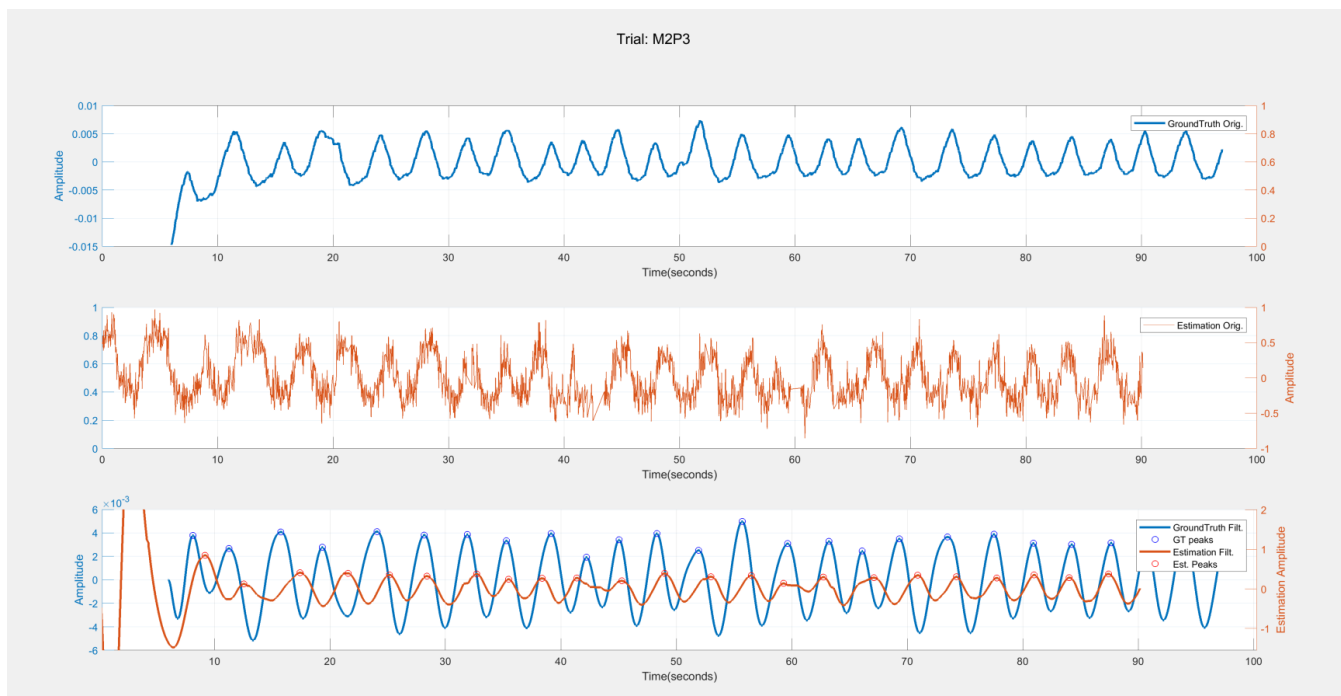


Figure (5S) shows the ground truth, followed by the unfiltered waveform and the filtered ground truth with filtered estimation for the right lateral position.

5.6 Subject 3 Trial 1

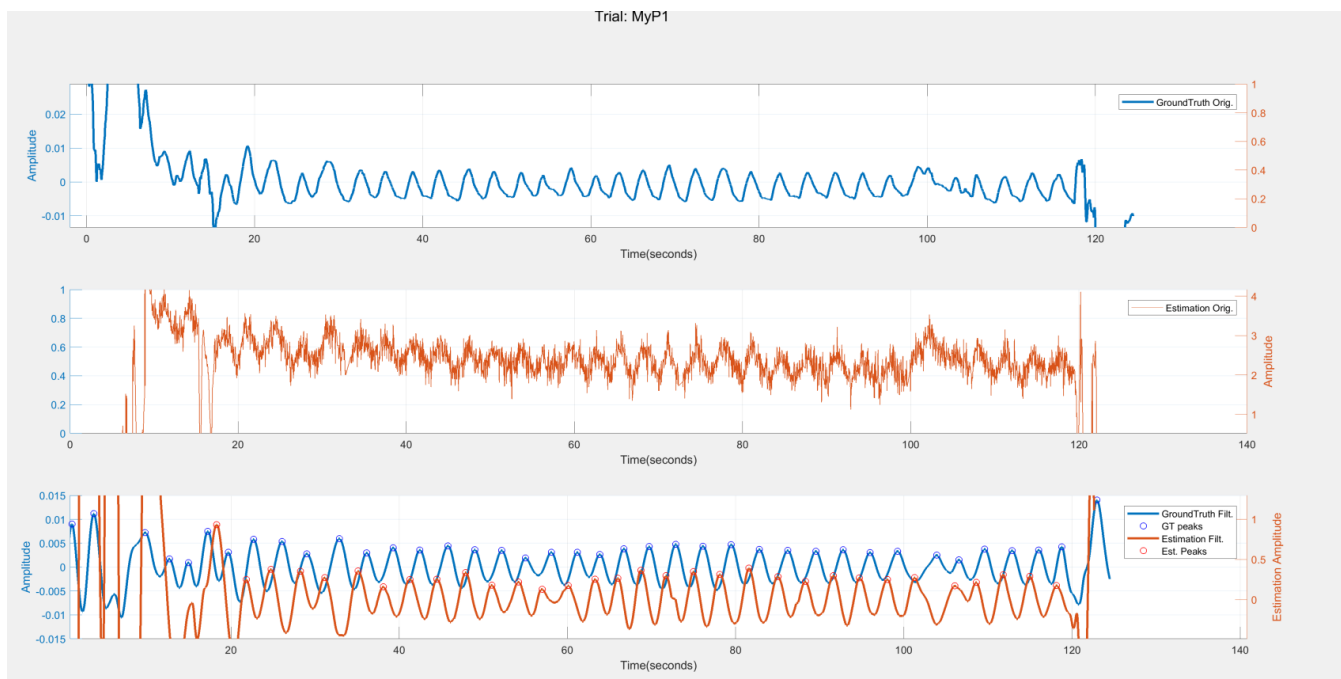


Figure (5T) shows the ground truth, followed by the unfiltered waveform and the filtered ground truth with filtered estimation for the supine position.

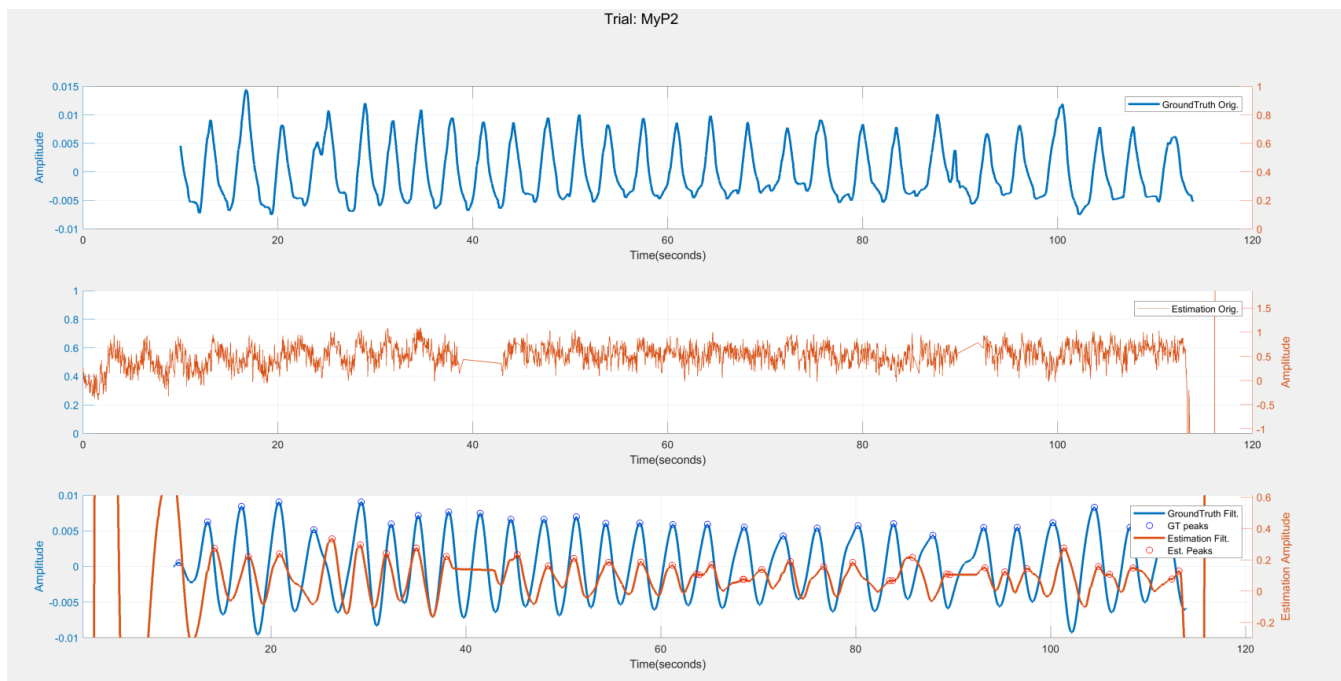


Figure (5U) shows the ground truth, followed by the unfiltered waveform and the filtered ground truth with filtered estimation for the left lateral position.

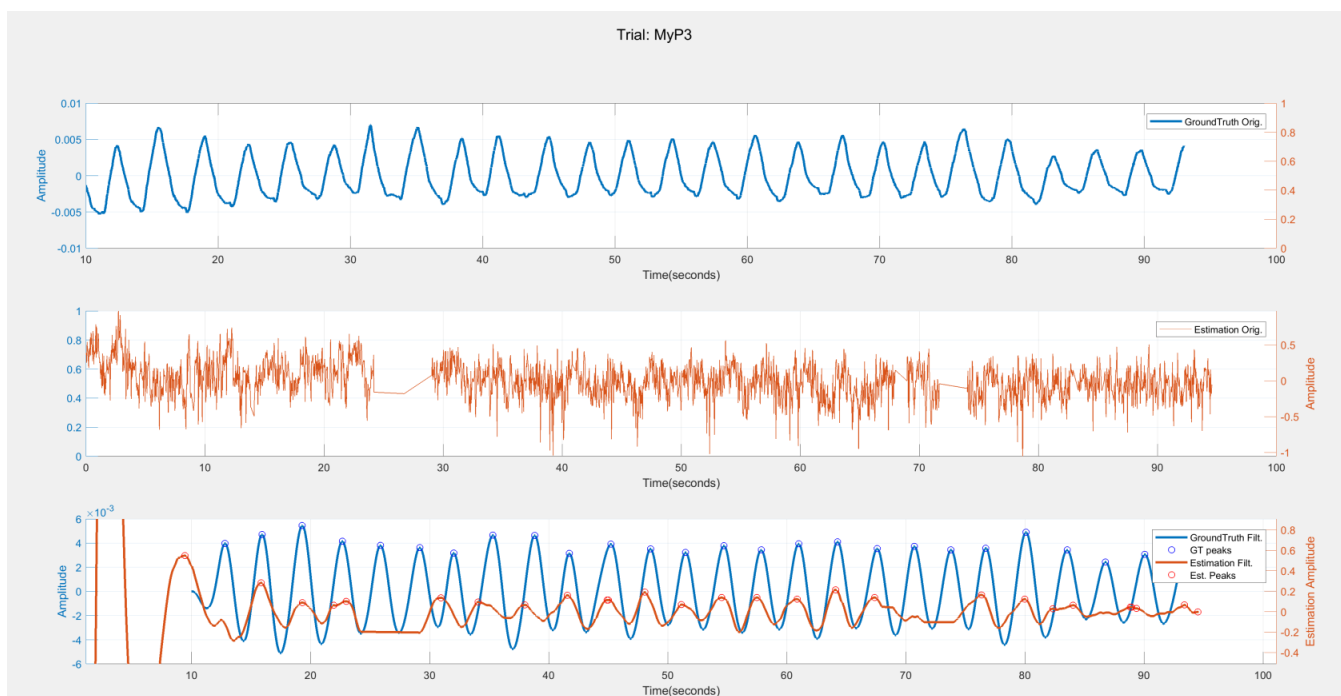


Figure (5V) shows the ground truth, followed by the unfiltered waveform and the filtered ground truth with filtered estimation for the right lateral position.

Chapter 6

Lab Results

The IRB2 trials dataset was obtained from the Foresite Healthcare DSK3 system that captured the depth data with the resolution of 640 x 480, at approximately 30fps. The IRB2 trials comprise of the respiration rate from the grid areas around the chest region. The postures have been manually segmented from the periods of restlessness due to posture changes. The cyan is the ground truth, and the dark blue is the actual respiration rate. For each subject, we have selected grids that pertain to the center of the chest region 7, 8, 9, 12, 13, 14, 17, 18, 19. The respiration rate is computed for different subjects, and for different positions, for different grid variations, and with peak and FFT algorithms. The net median for all the respiration rates from the depth data is also computed, and displayed as green. IRB2 subjects #16-#25 are numbered #1-#10 on the graph. The shared folder where the IRB data is stored can be found at

- [\\CIRLWS24\Eldercare - IRB Shared Folder](#)
- lewis.net.missouri.edu:/storage/htc/eldercare/data/projectdata/cameraRespRestless

6.1. IRB2 Fixed grids peak detection

6.1.1 Average

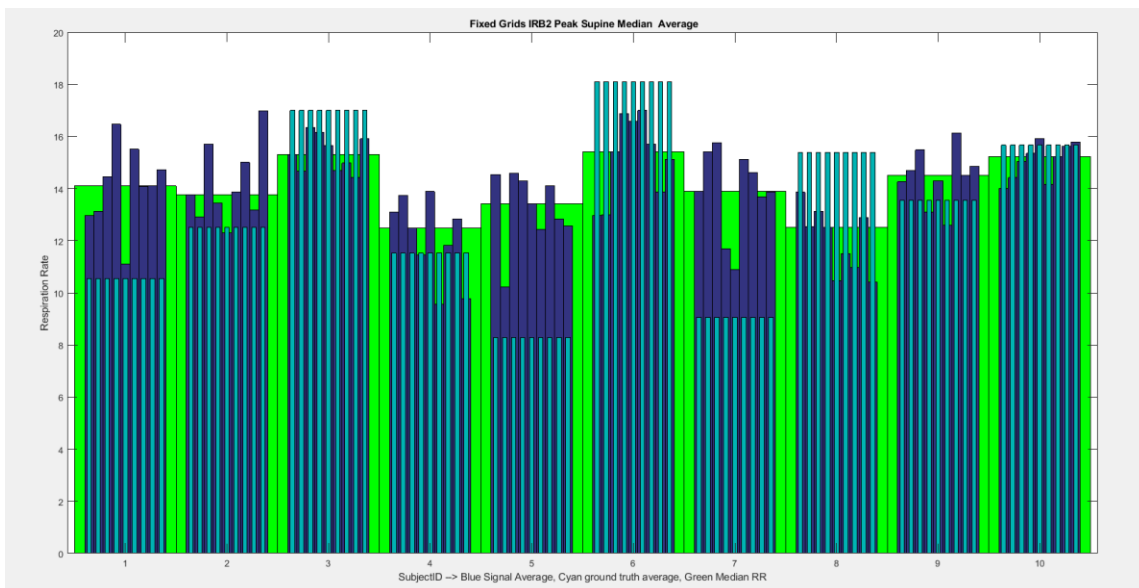


Figure (6A) shows the algorithm respiration detection rate for Supine, for subjects 16-25, grids 7, 8, 9, 12, 13, 14, 17, 18, 19. Cyan is the ground truth, blue is the respiration rate from the depth data, Green is the median Respiration rate from all the grids.

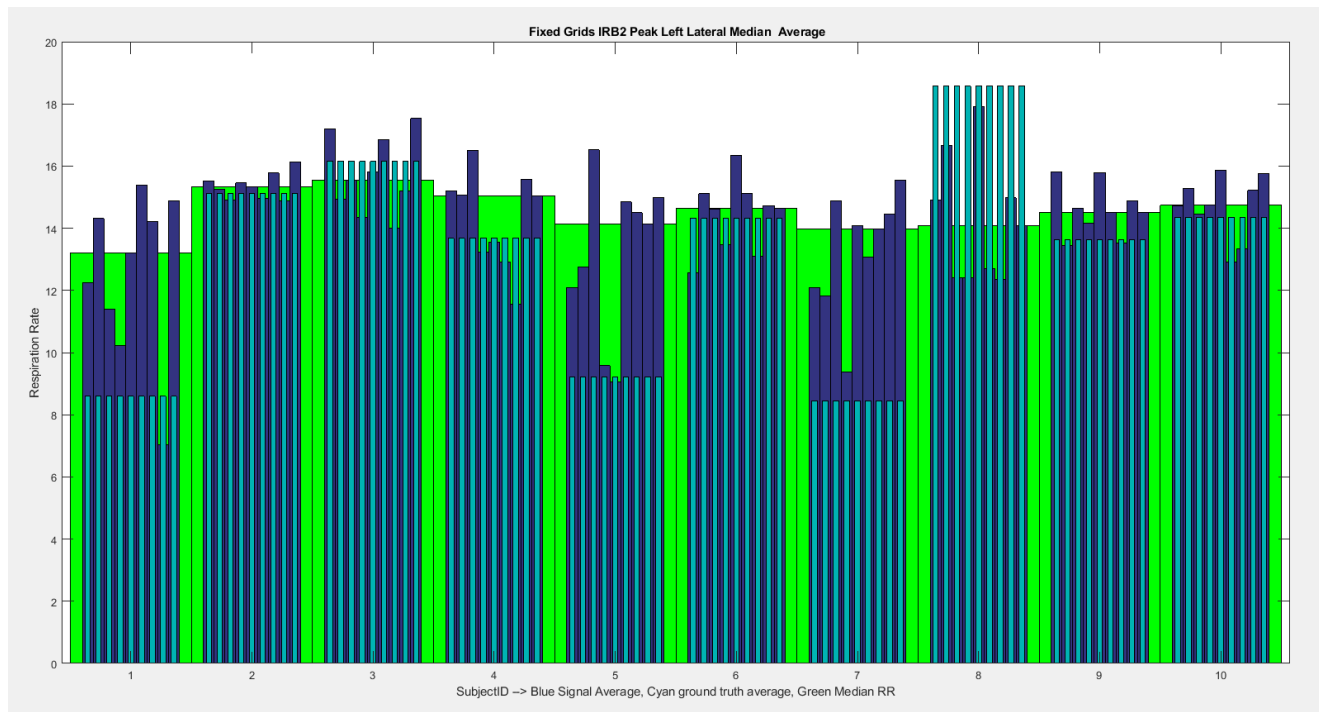


Figure (6B) shows the algorithm respiration detection rate, for subjects 16-25, grids 7, 8, 9, 12, 13, 14, 17, 18, 19. Cyan is the ground truth, blue is the respiration rate from the depth data, Green is the median Respiration rate from all the grids.

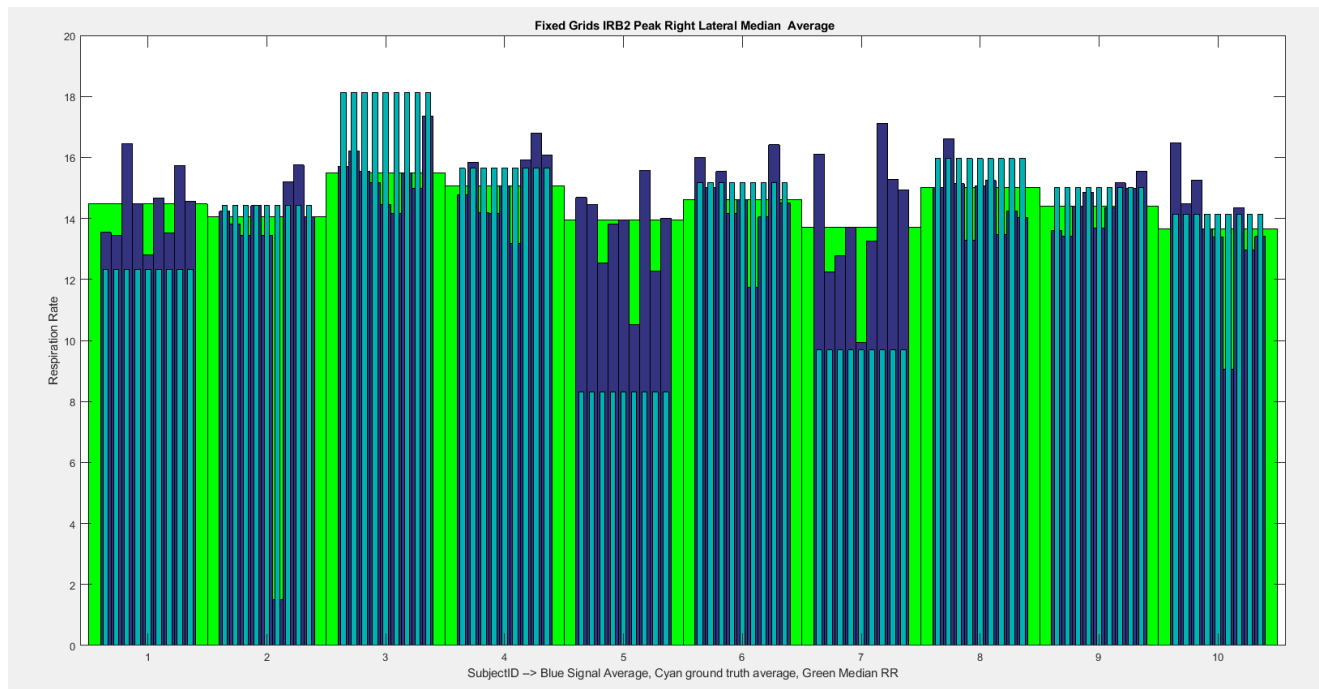


Figure (6C) shows the algorithm respiration detection rate, for subjects 16-25, grids 7, 8, 9, 12, 13, 14, 17, 18, 19. Cyan is the ground truth, blue is the respiration rate from the depth data, Green is the median Respiration rate from all the grids.

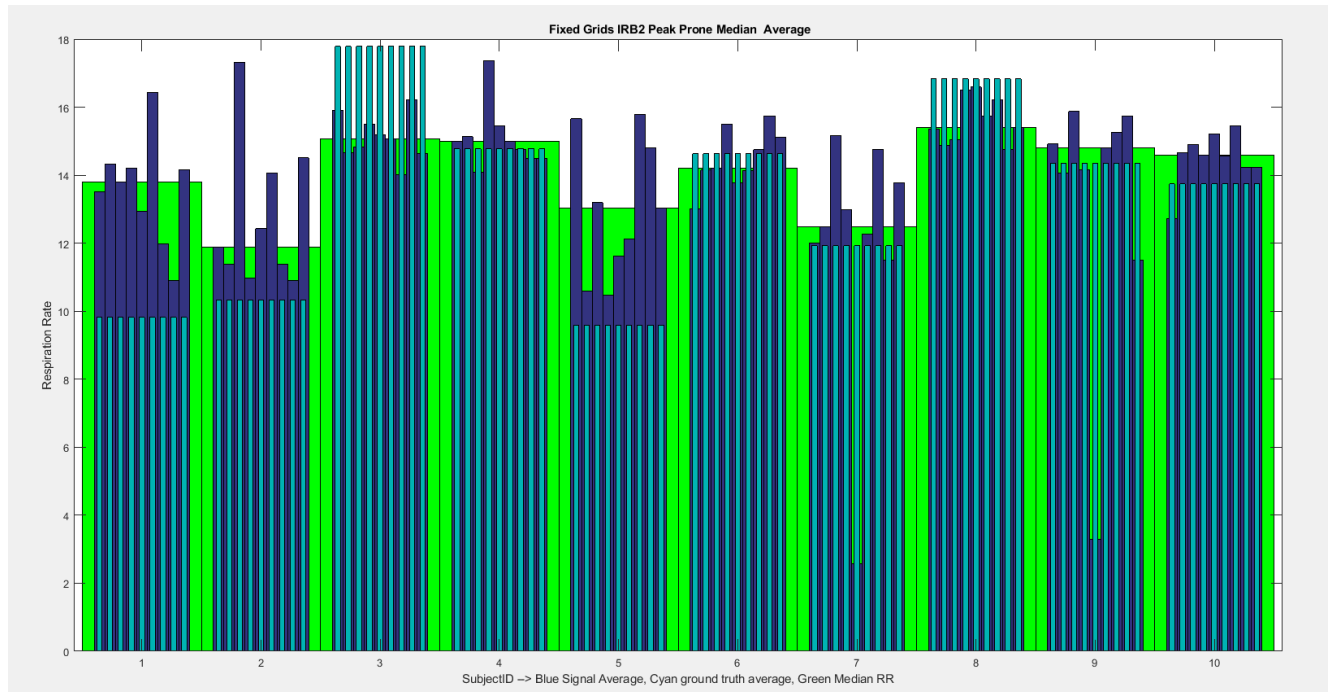


Figure (6D) shows the algorithm respiration detection rate, for subjects 16-25, grids 7, 8, 9, 12, 13, 14, 17, 18, 19. Cyan is the ground truth, blue is the respiration rate from the depth data, Green is the median Respiration rate from all the grids.

6.1.2 Median

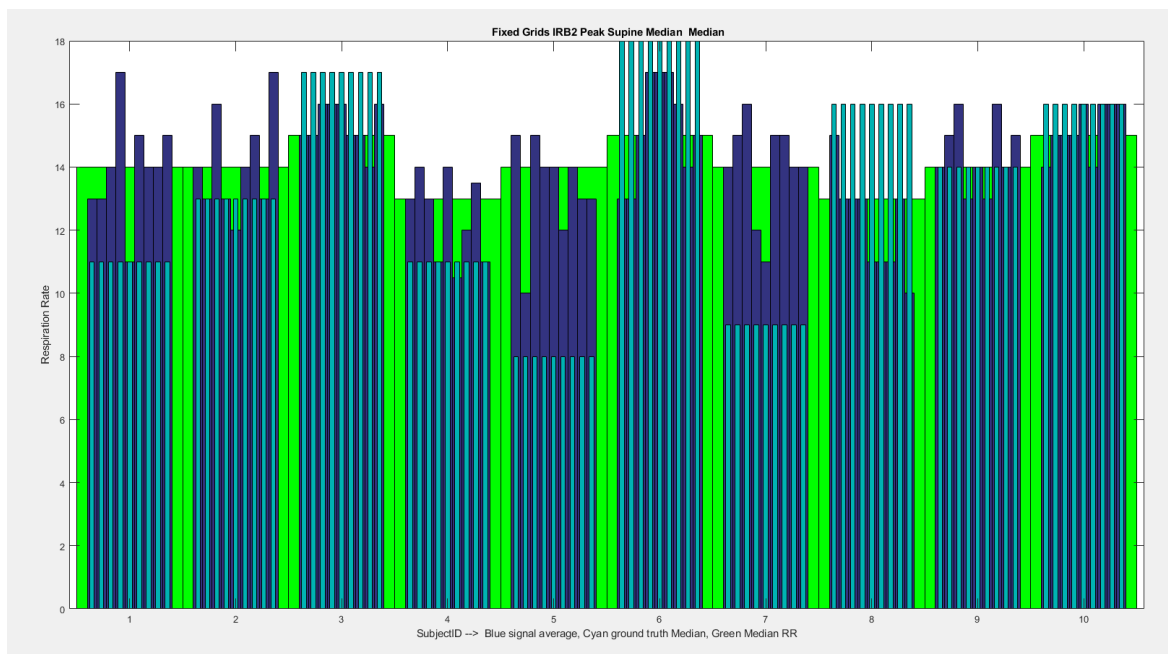


Figure (6E) shows the algorithm respiration detection rate, for subjects 16-25, grids 7, 8, 9, 12, 13, 14, 17, 18, 19. Cyan is the ground truth, blue is the respiration rate from the depth data, Green is the median Respiration rate from all the grids.

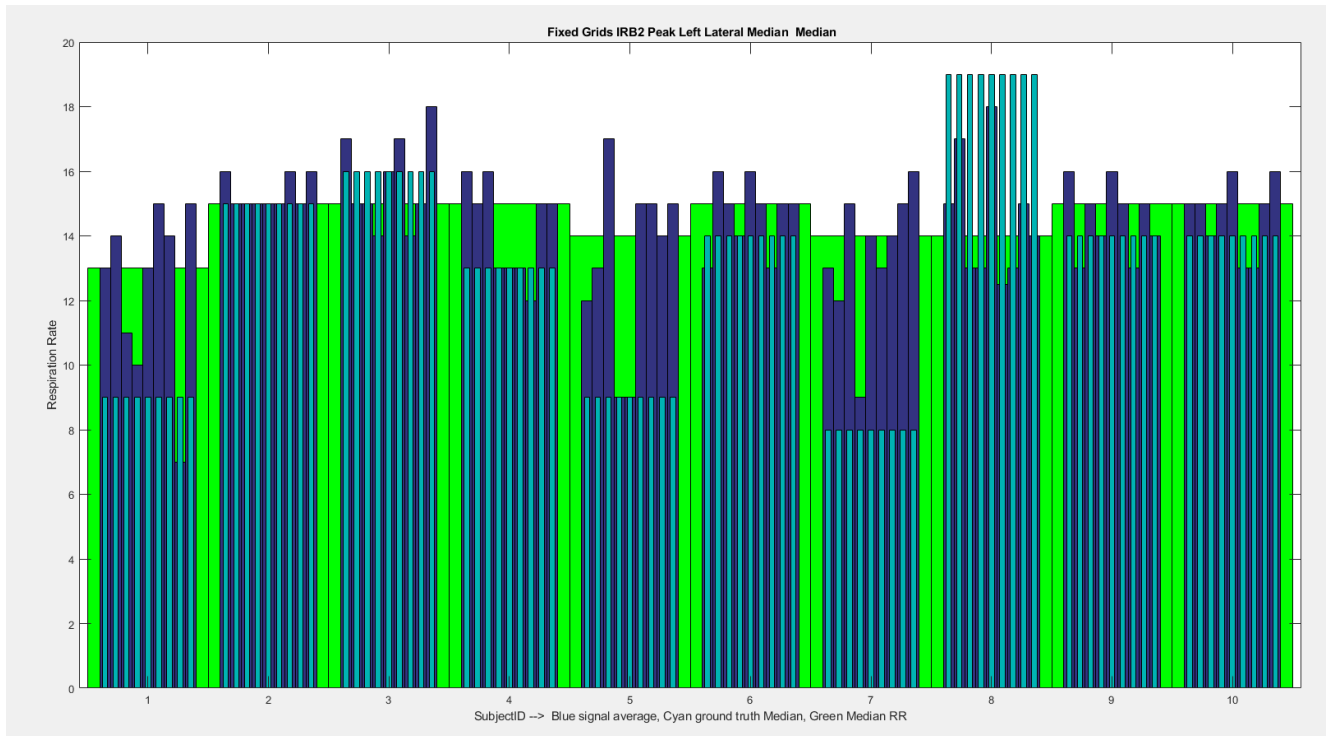


Figure (6F) shows the algorithm respiration detection rate, for subjects 16-25, grids 7, 8, 9, 12, 13, 14, 17, 18, 19. Cyan is the ground truth, blue is the respiration rate from the depth data, Green is the median Respiration rate from all the grids.

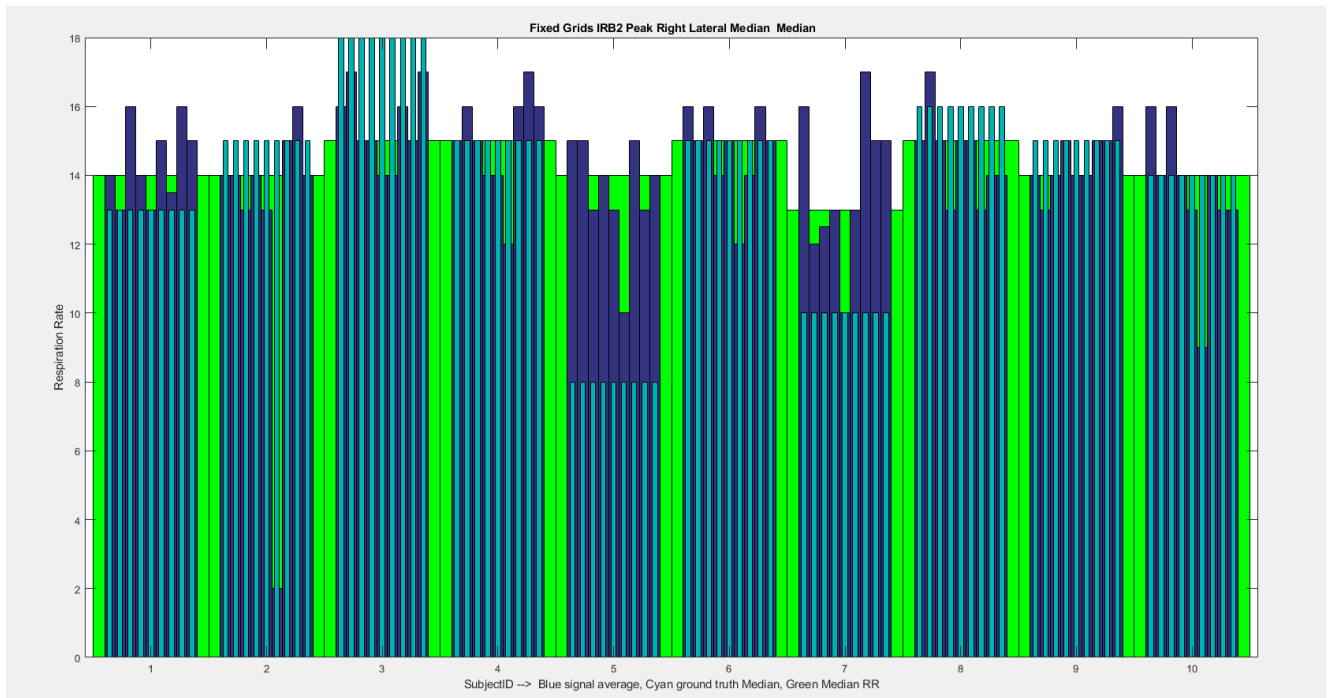


Figure (6G) shows the algorithm respiration detection rate, for subjects 16-25, grids 7, 8, 9, 12, 13, 14, 17, 18, 19. Cyan is the ground truth, blue is the respiration rate from the depth data, Green is the median Respiration rate from all the grids.

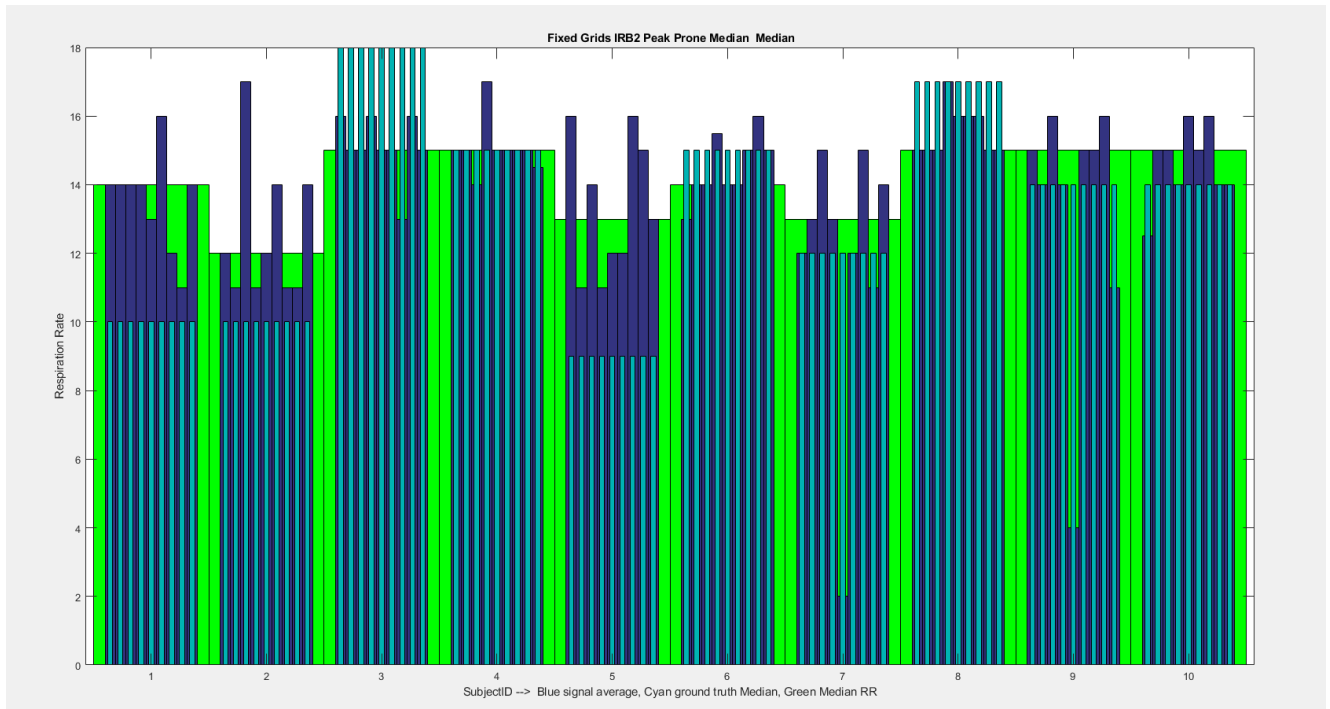


Figure (6H) shows the algorithm respiration detection rate, for subjects 16-25, grids 7, 8, 9, 12, 13, 14, 17, 18, 19. Cyan is the ground truth, blue is the respiration rate from the depth data, Green is the median Respiration rate from all the grids.

6.2. IRB2 Varying grids Peak detection

6.2.1 Average

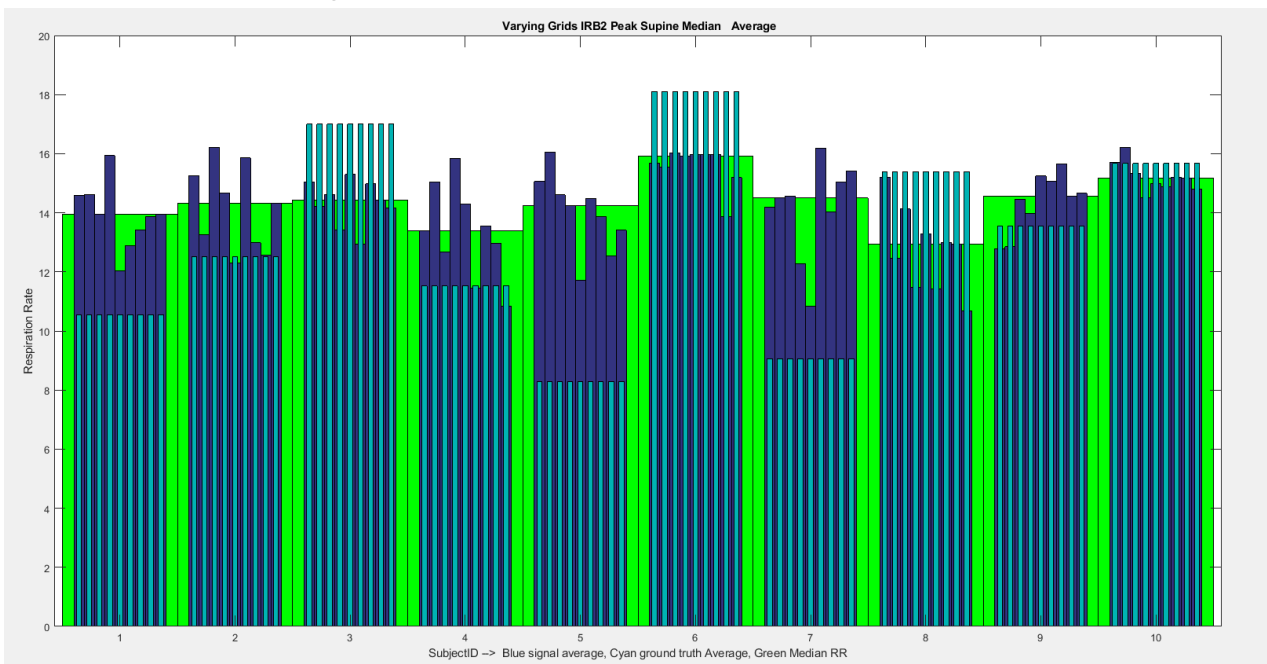


Figure (6I) shows the algorithm respiration detection rate, for subjects 16-25, grids 7, 8, 9, 12, 13, 14, 17, 18, 19. Cyan is the ground truth, blue is the respiration rate from the depth data, Green is the median Respiration rate from all the grids.

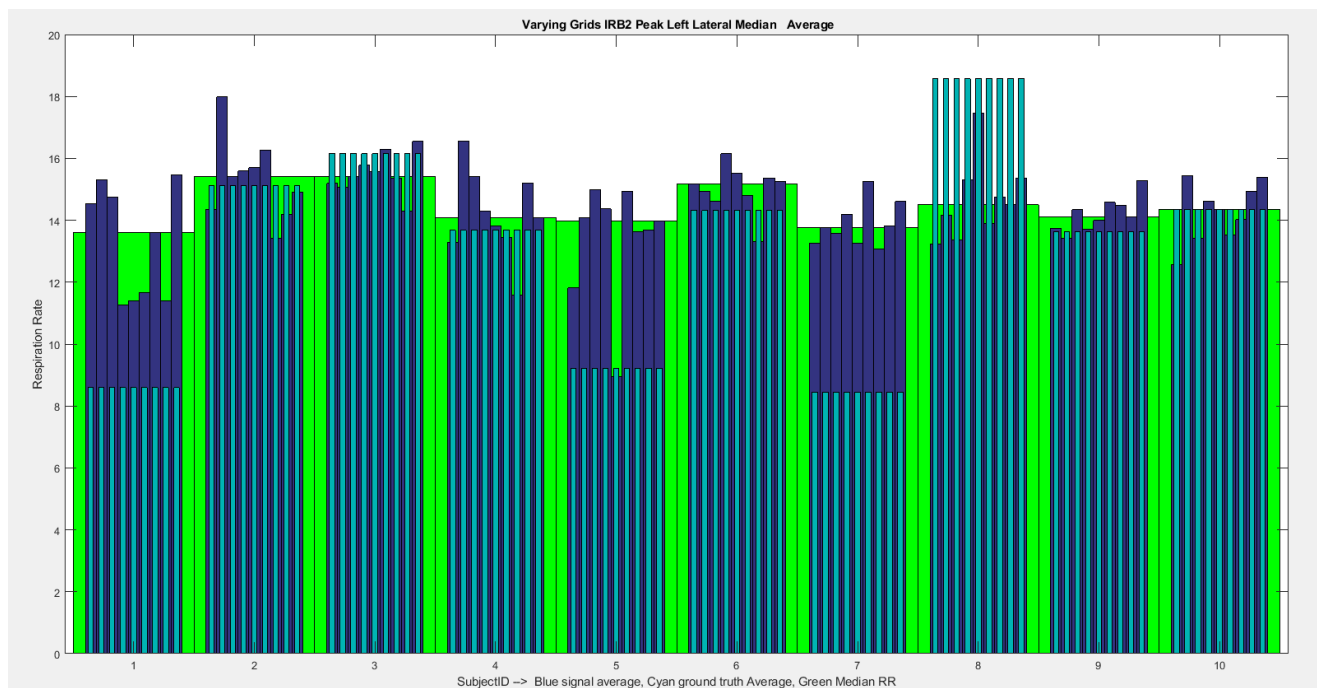


Figure (6J) shows the algorithm respiration detection rate, for subjects 16-25, grids 7, 8, 9, 12, 13, 14, 17, 18, 19. Cyan is the ground truth, blue is the respiration rate from the depth data, Green is the median Respiration rate from all the grids.

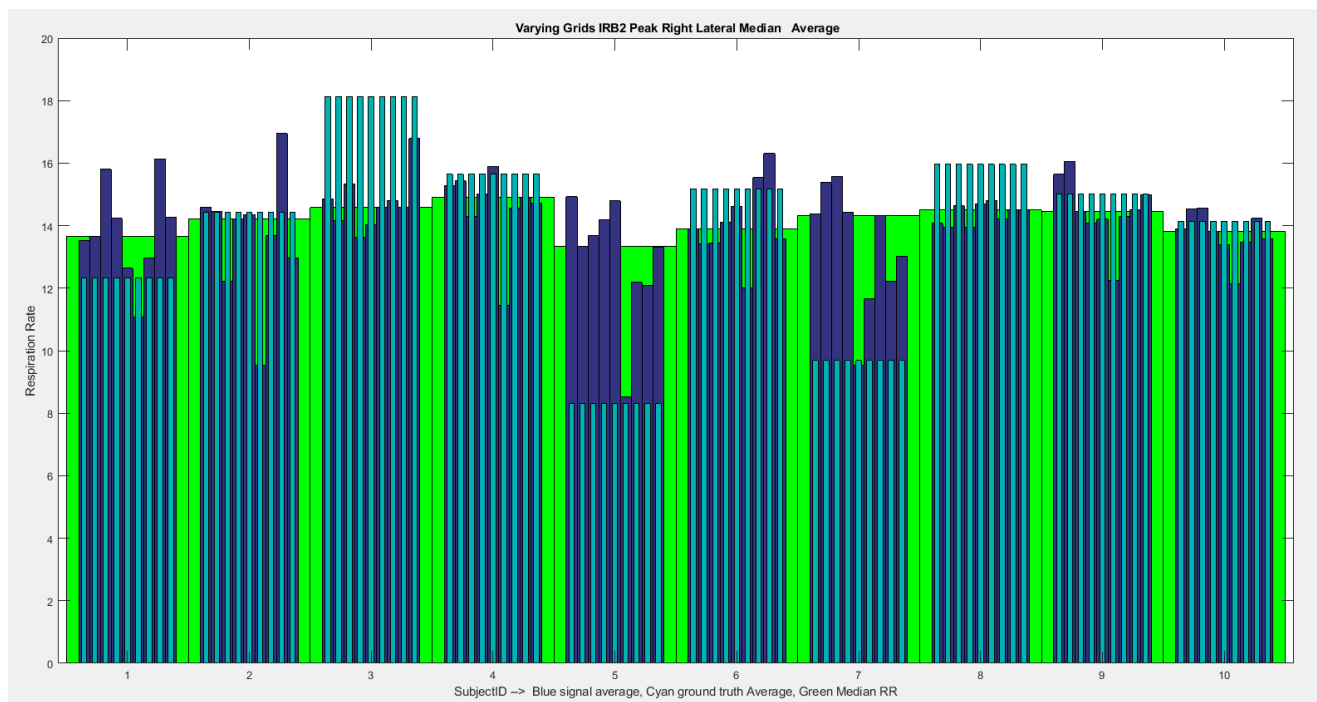


Figure (6K) shows the algorithm respiration detection rate, for subjects 16-25, grids 7, 8, 9, 12, 13, 14, 17, 18, 19. Cyan is the ground truth, blue is the respiration rate from the depth data, Green is the median Respiration rate from all the grids.

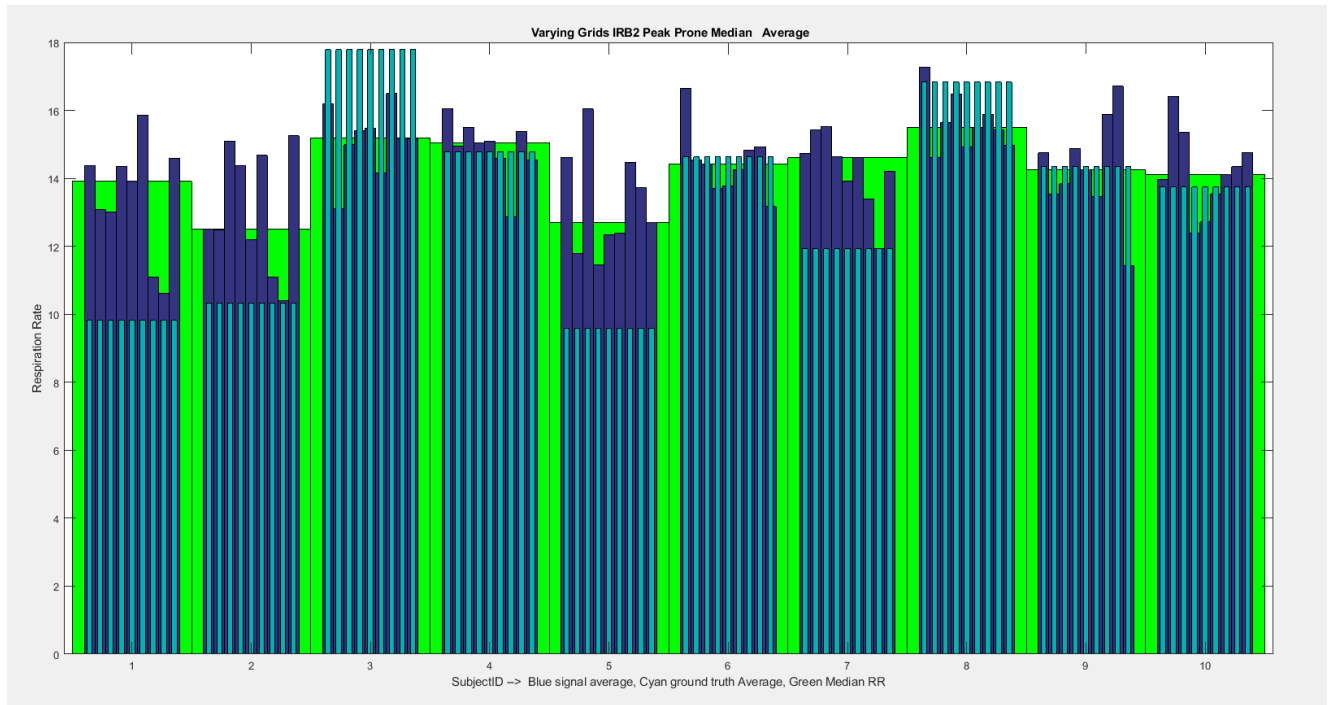


Figure (6L) shows the algorithm respiration detection rate, for subjects 16-25, grids 7, 8, 9, 12, 13, 14, 17, 18, 19. Cyan is the ground truth, blue is the respiration rate from the depth data, Green is the median Respiration rate from all the grids.

6.2.2 Median

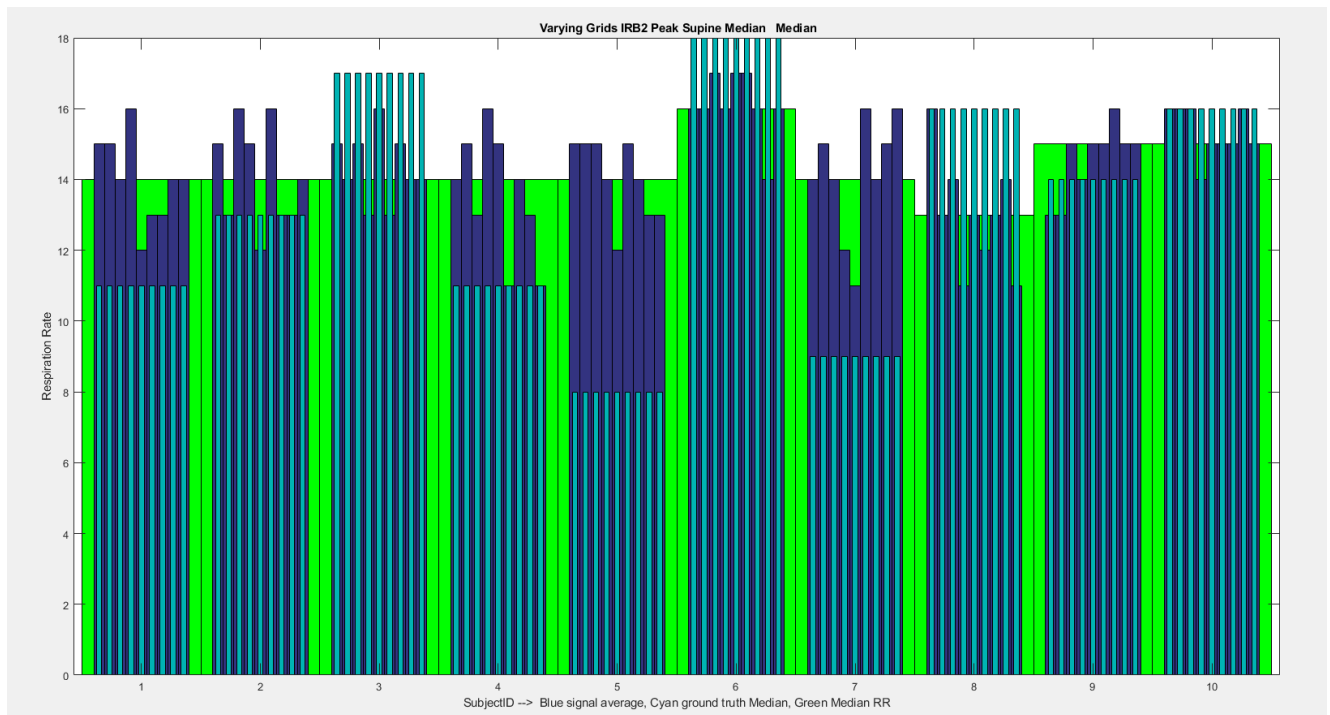


Figure (6M) shows the algorithm respiration detection rate, for subjects 16-25, grids 7, 8, 9, 12, 13, 14, 17, 18, 19. Cyan is the ground truth, blue is the respiration rate from the depth data, Green is the median Respiration rate from all the grids.

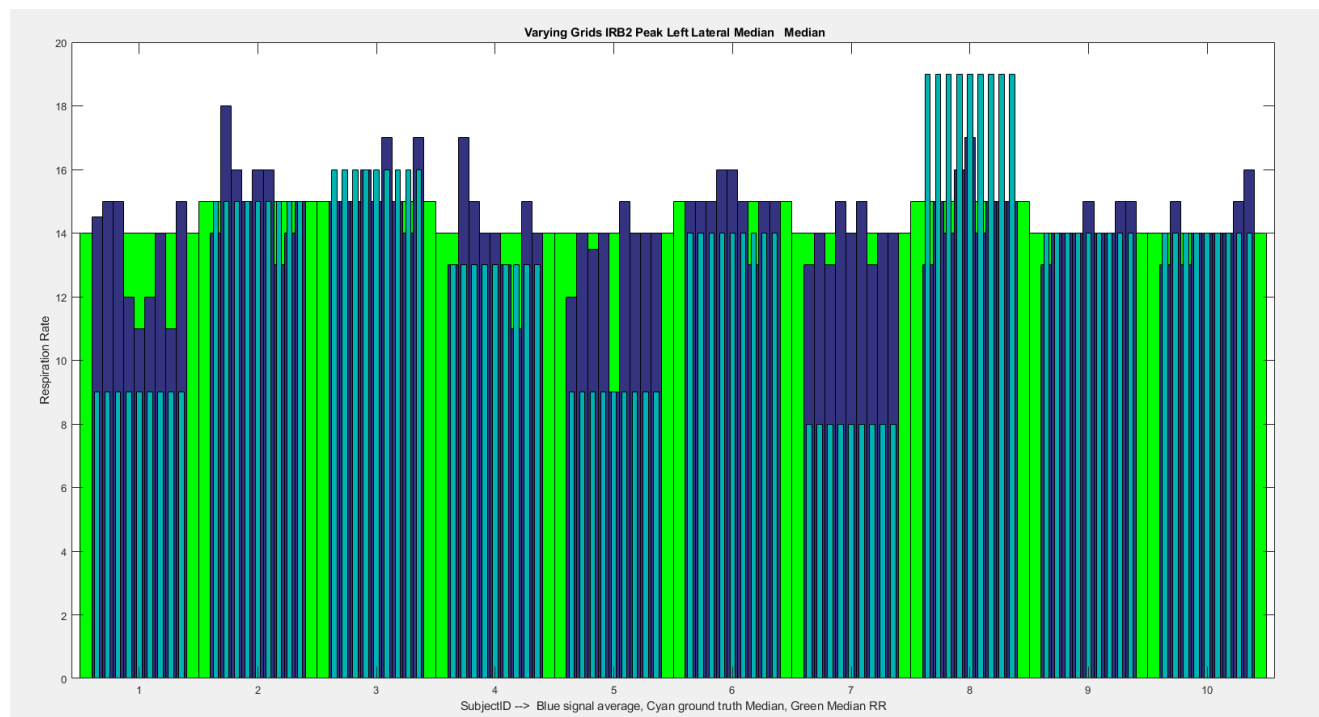


Figure (6N) shows the algorithm respiration detection rate, for subjects 16-25, grids 7, 8, 9, 12, 13, 14, 17, 18, 19. Cyan is the ground truth, blue is the respiration rate from the depth data, Green is the median Respiration rate from all the grids.

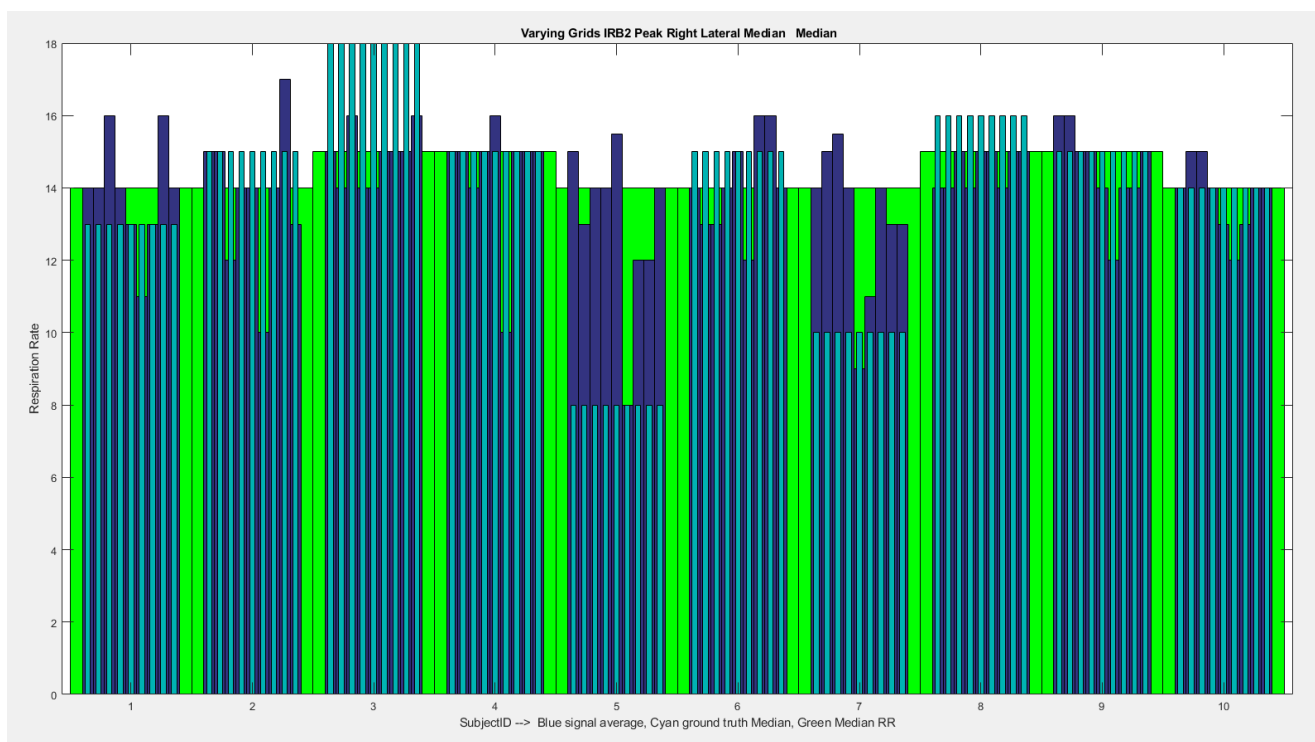


Figure (6O) shows the algorithm respiration detection rate, for subjects 16-25, grids 7, 8, 9, 12, 13, 14, 17, 18, 19. Cyan is the ground truth, blue is the respiration rate from the depth data, Green is the median Respiration rate from all the grids.

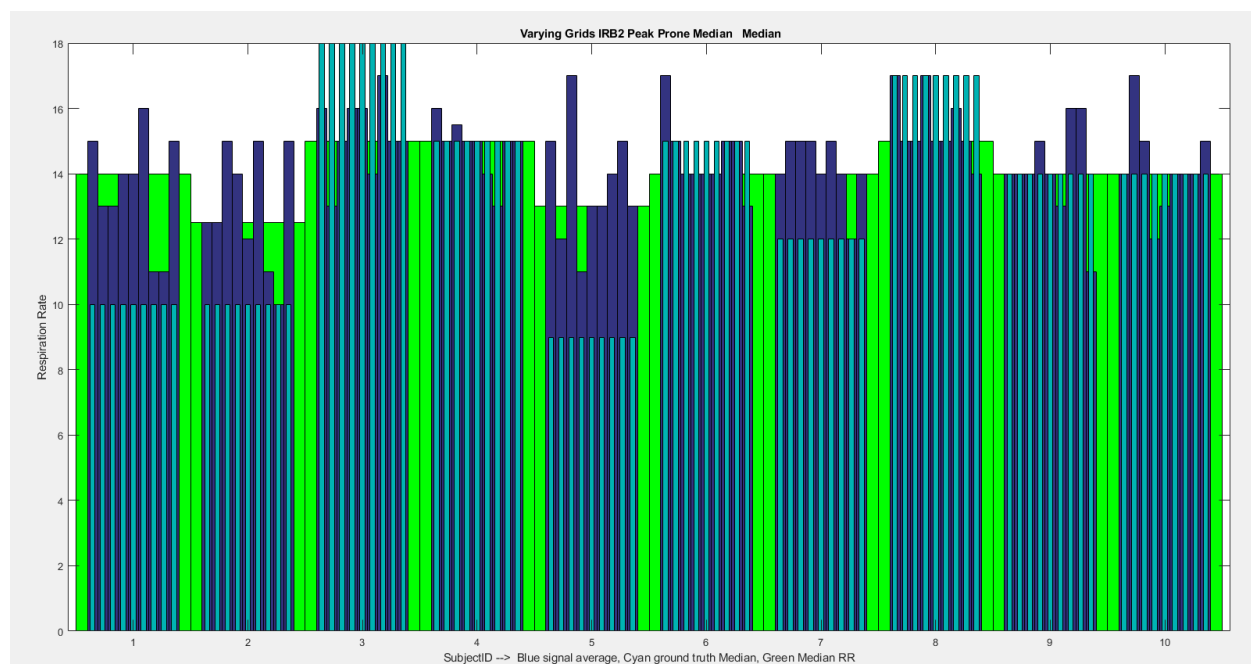


Figure (6P) shows the algorithm respiration detection rate, for subjects 16-25, grids 7, 8, 9, 12, 13, 14, 17, 18, 19. Cyan is the ground truth, blue is the respiration rate from the depth data, Green is the median Respiration rate from all the grids.

6.3. IRB2 Fixed grids FFT detection

6.3.1. Average

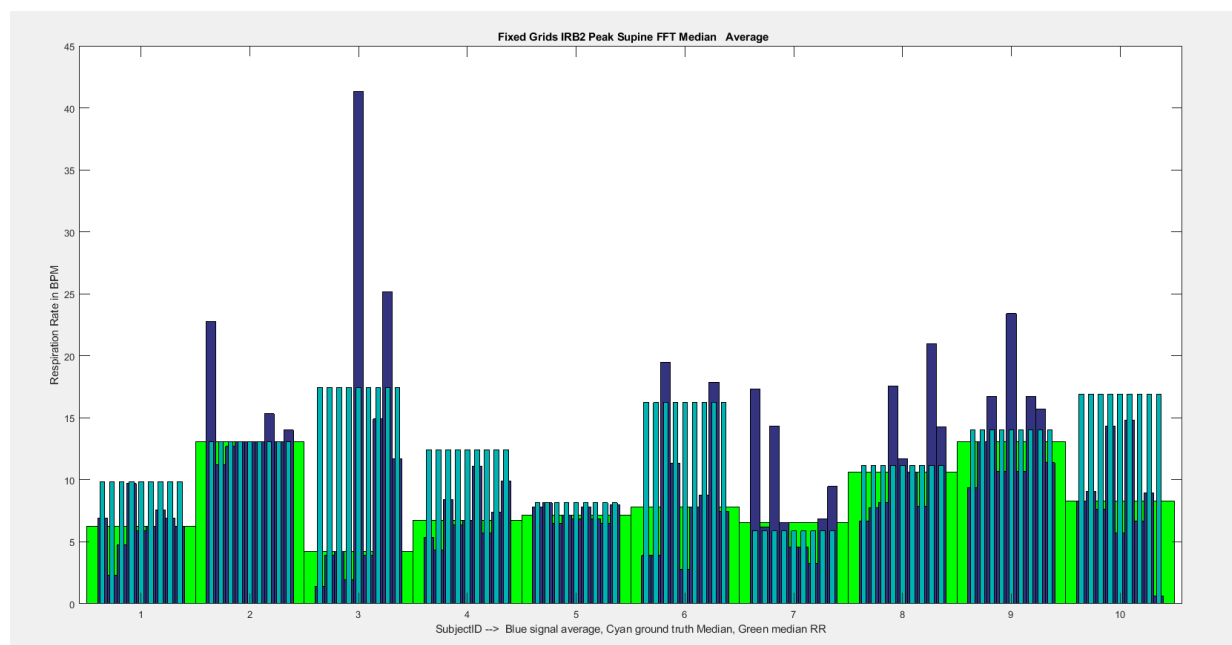


Figure (6Q) shows the algorithm respiration detection rate, for subjects 16-25, grids 7, 8, 9, 12, 13, 14, 17, 18, 19. Cyan is the ground truth, blue is the respiration rate from the depth data, Green is the median Respiration rate from all the grids.

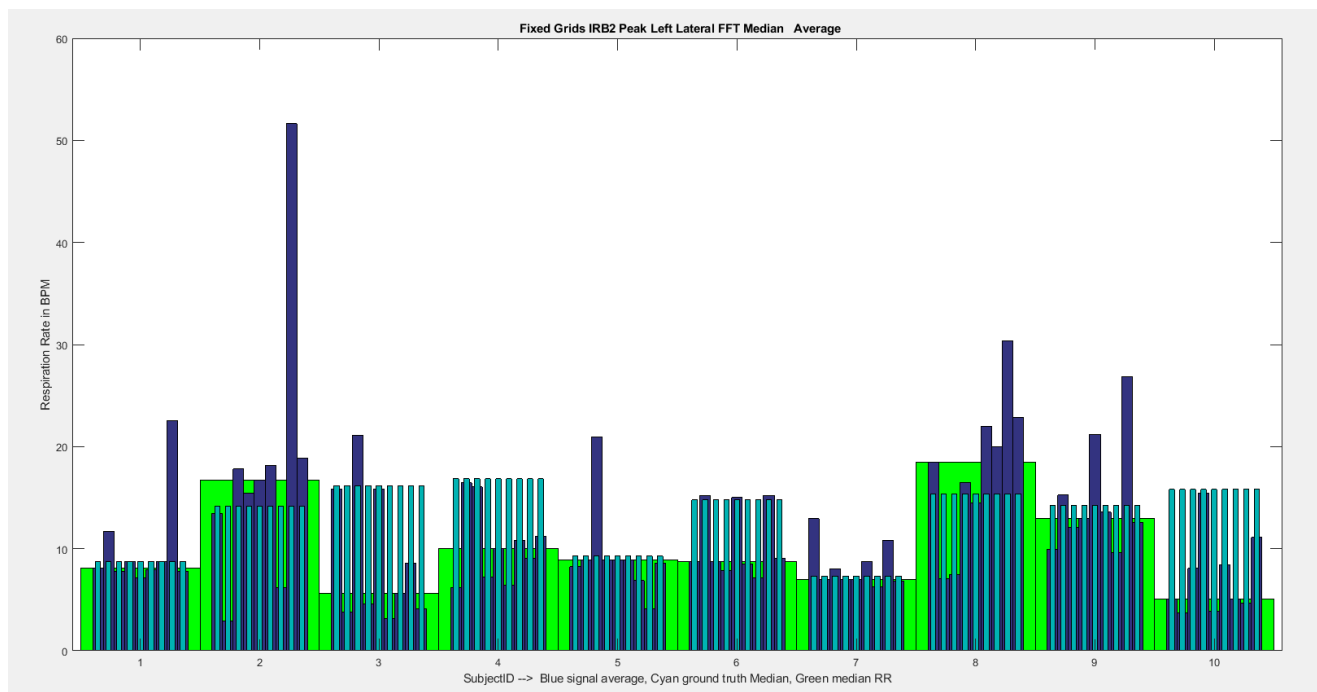


Figure (6R) shows the algorithm respiration detection rate, for subjects 16-25, grids 7, 8, 9, 12, 13, 14, 17, 18, 19. Cyan is the ground truth, blue is the respiration rate from the depth data, Green is the median Respiration rate from all the grids.

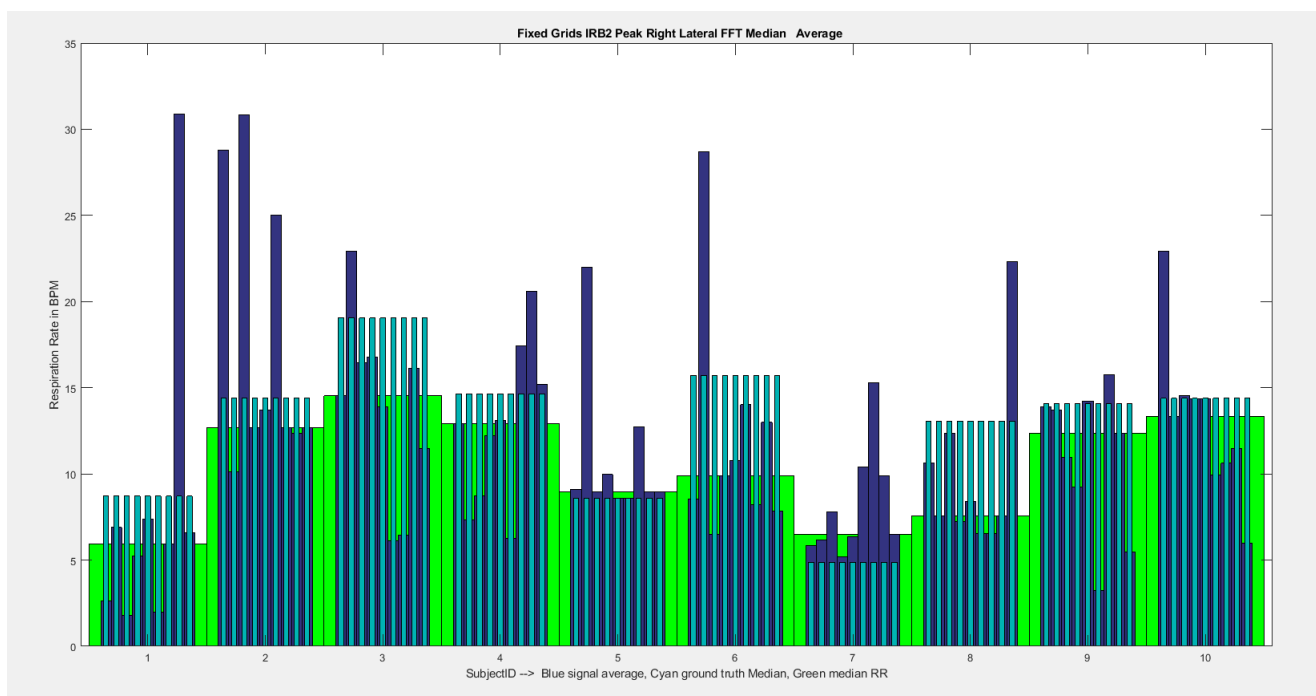
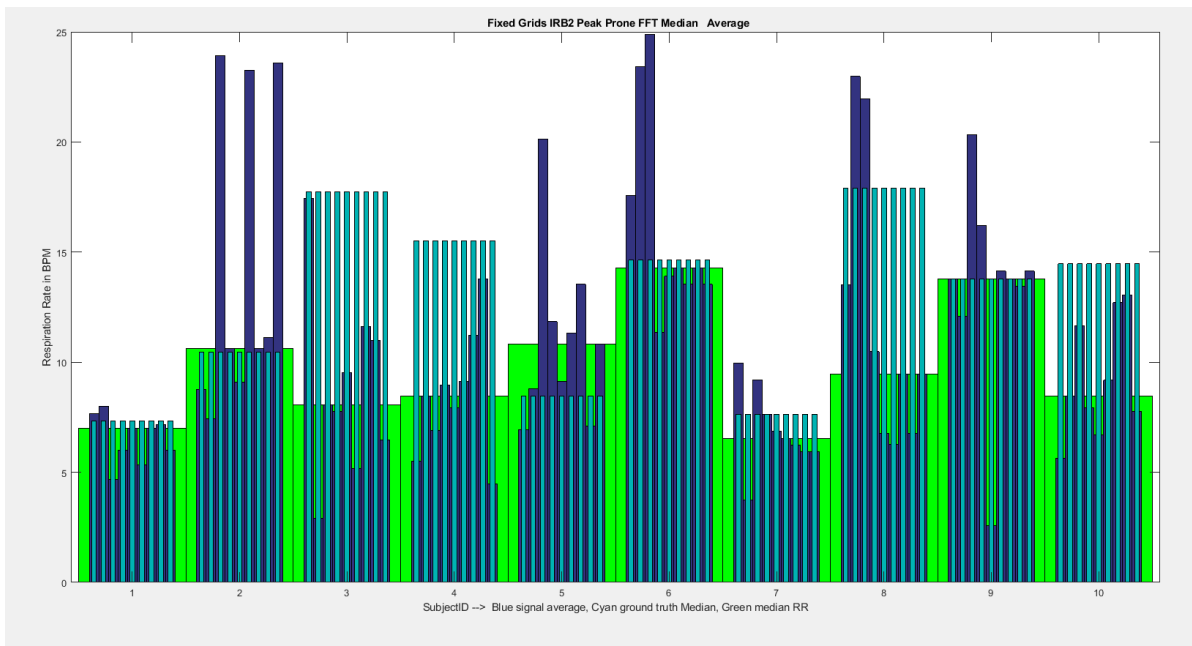


Figure (6S) shows the algorithm respiration detection rate, for subjects 16-25, grids 7, 8, 9, 12, 13, 14, 17, 18, 19. Cyan is the ground truth, blue is the respiration rate from the depth data, Green is the median Respiration rate from all the grids.



Figure

(6T) shows the algorithm respiration detection rate, for subjects 16-25, grids 7, 8, 9, 12, 13, 14, 17, 18, 19. Cyan is the ground truth, blue is the respiration rate from the depth data, Green is the median Respiration rate from all the grids.

6.3.2. Median

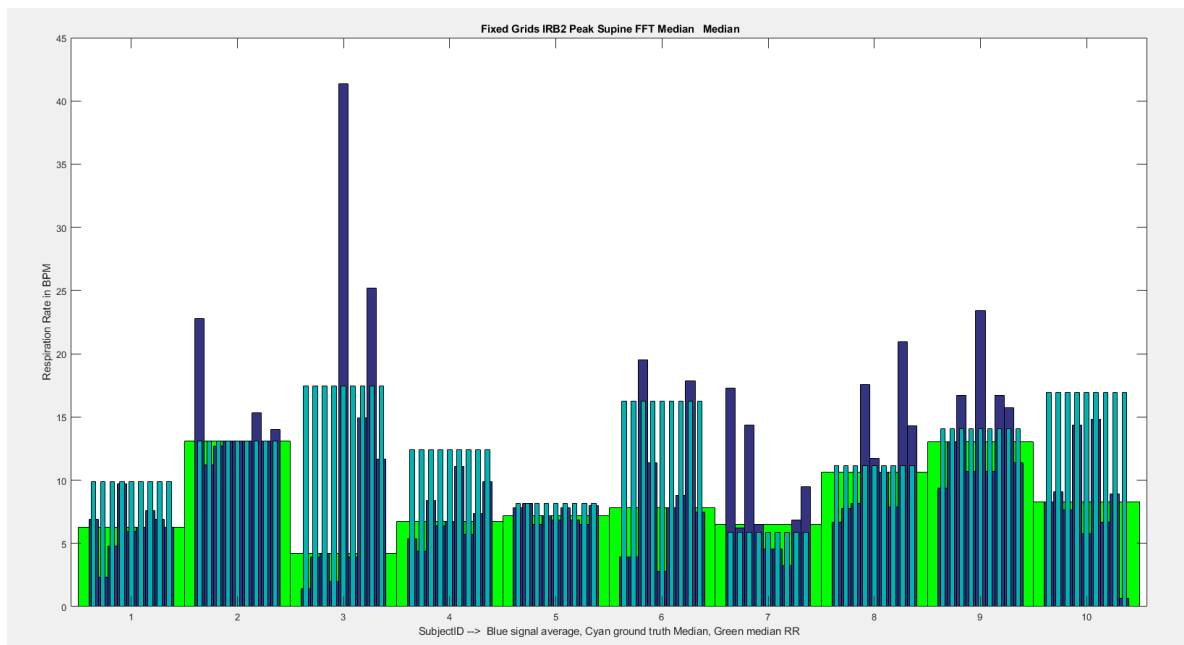


Figure (6U) shows the algorithm respiration detection rate, for subjects 16-25, grids 7, 8, 9, 12, 13, 14, 17, 18, 19. Cyan is the ground truth, blue is the respiration rate from the depth data, Green is the median Respiration rate from all the grids.

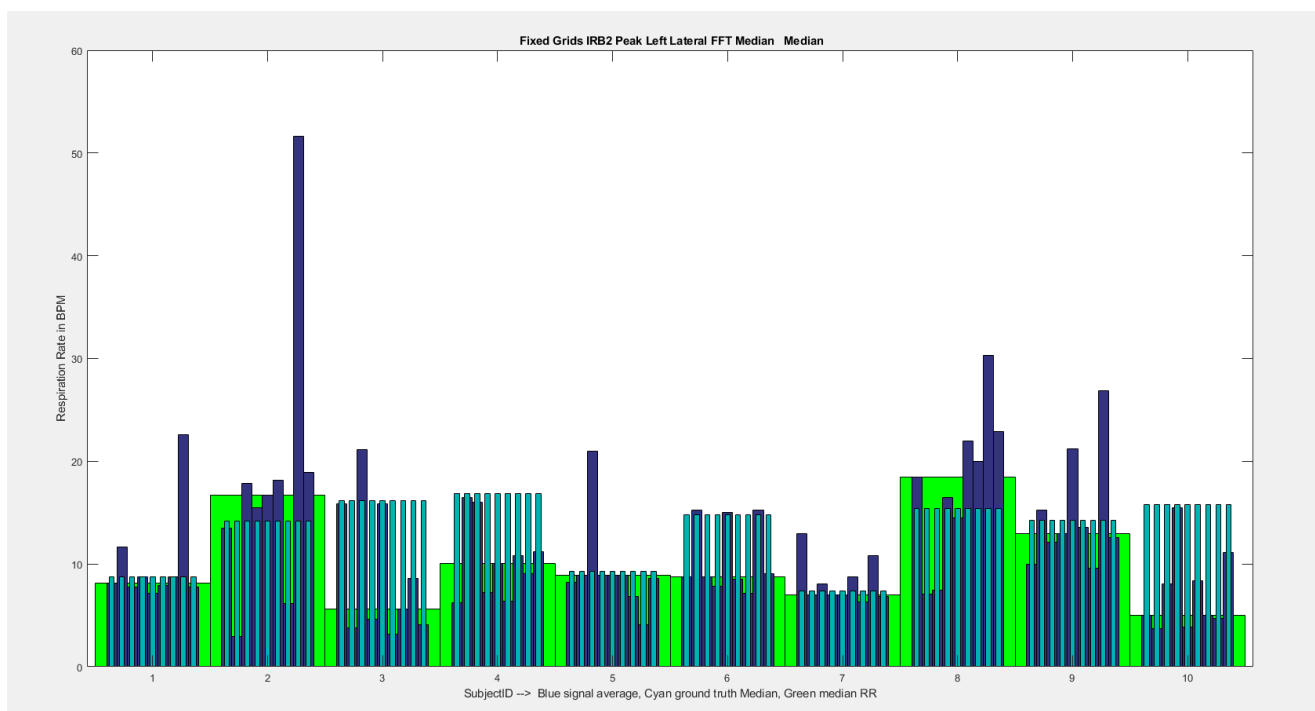


Figure (6V) shows the algorithm respiration detection rate, for subjects 16-25, grids 7, 8, 9, 12, 13, 14, 17, 18, 19. Cyan is the ground truth, blue is the respiration rate from the depth data, Green is the median Respiration rate from all the grids.

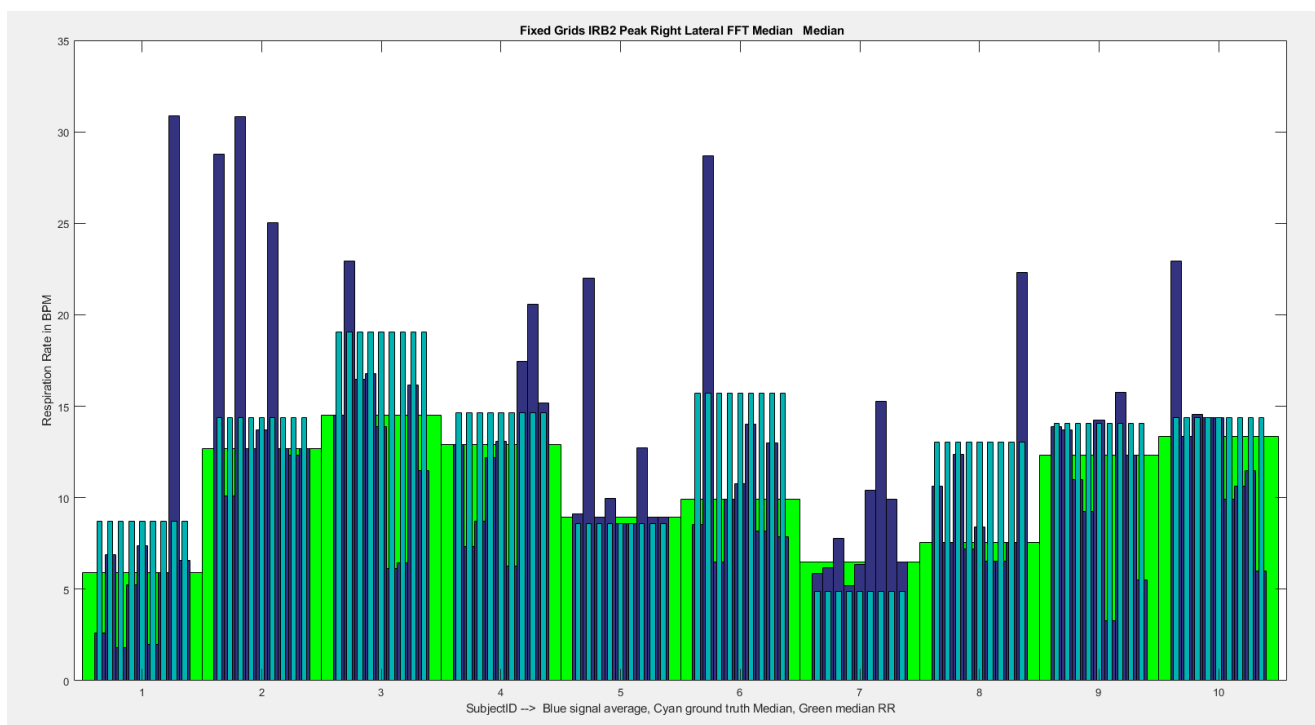


Figure (6W) shows the algorithm respiration detection rate, for subjects 16-25, grids 7, 8, 9, 12, 13, 14, 17, 18, 19. Cyan is the ground truth, blue is the respiration rate from the depth data, Green is the median Respiration rate from all the grids.

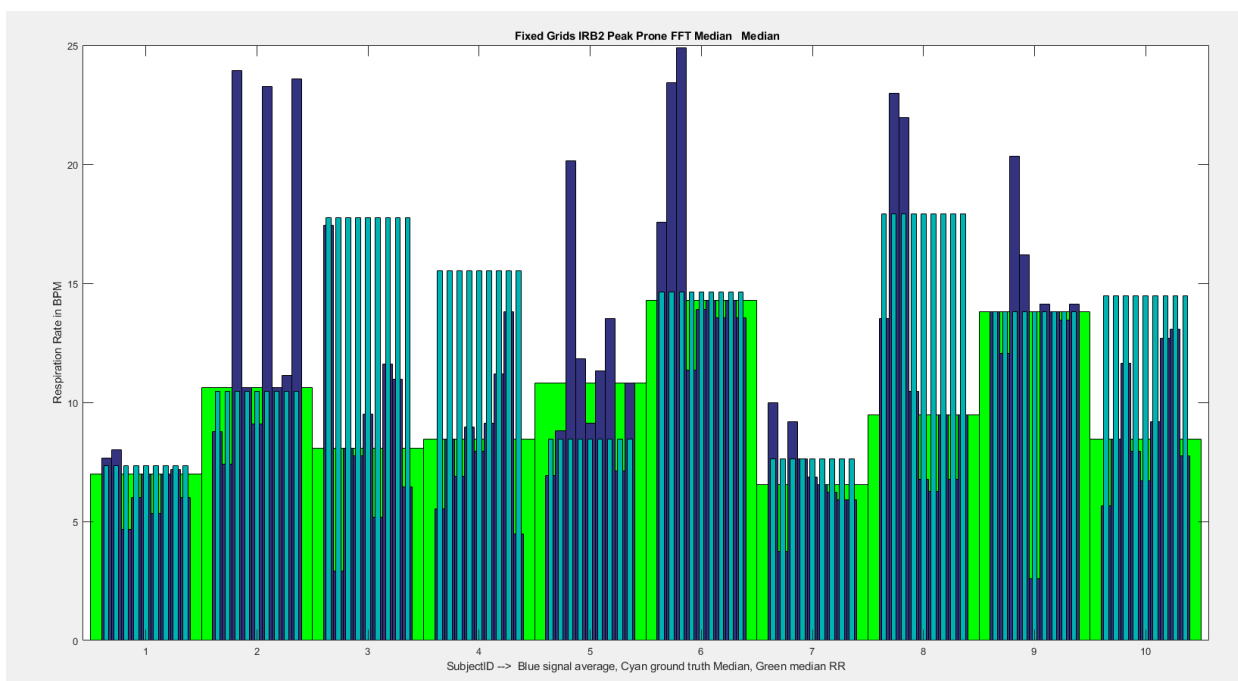


Figure (6X) shows the algorithm respiration detection rate, for subjects 16-25, grids 7, 8, 9, 12, 13, 14, 17, 18, 19. Cyan is the ground truth, blue is the respiration rate from the depth data, Green is the median Respiration rate from all the grids.

6.4. IRB2 varying grids FFT detection

6.4.1. Average

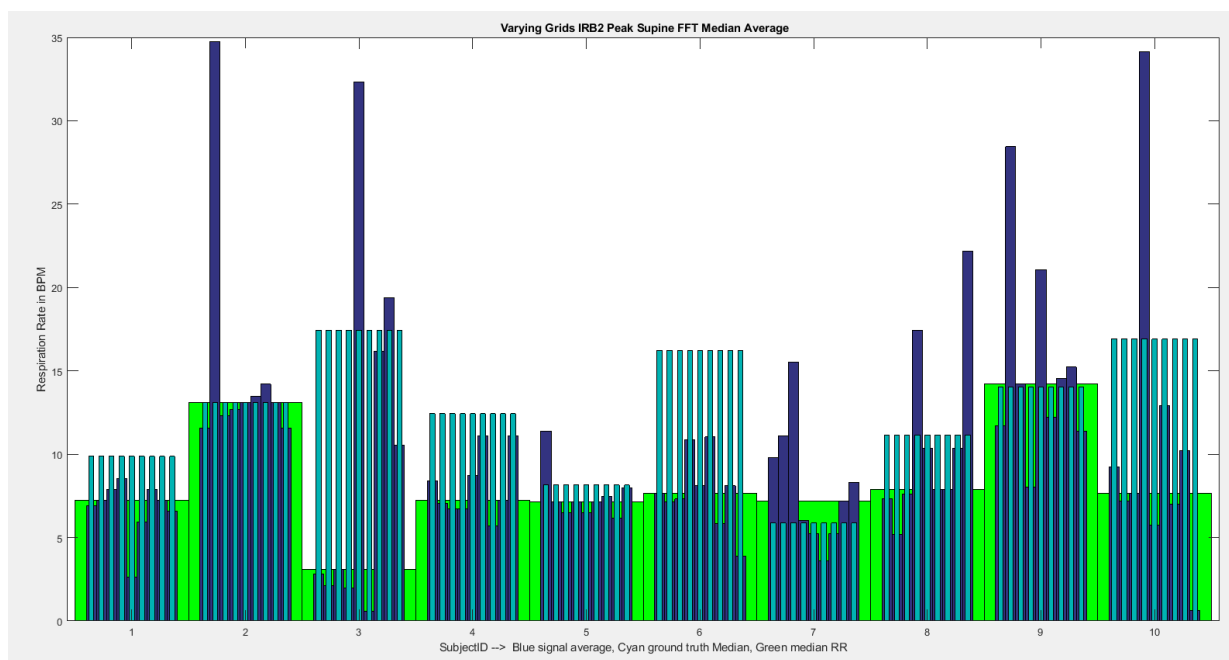


Figure (6Y) shows the algorithm respiration detection rate, for subjects 16-25, grids 7, 8, 9, 12, 13, 14, 17, 18, 19. Cyan is the ground truth, blue is the respiration rate from the depth data, Green is the median Respiration rate from all the grids.

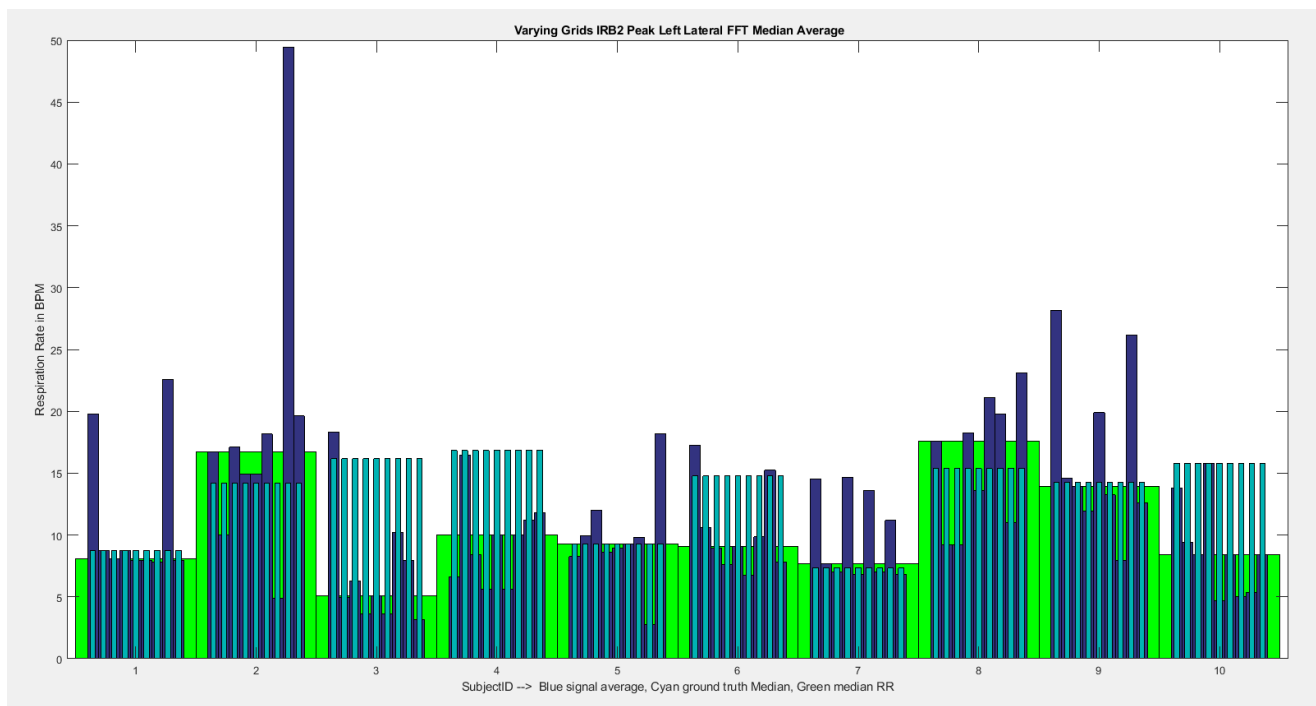


Figure (6Z) shows the algorithm respiration detection rate, for subjects 16-25, grids 7, 8, 9, 12, 13, 14, 17, 18, 19. Cyan is the ground truth, blue is the respiration rate from the depth data, Green is the median Respiration rate from all the grids.

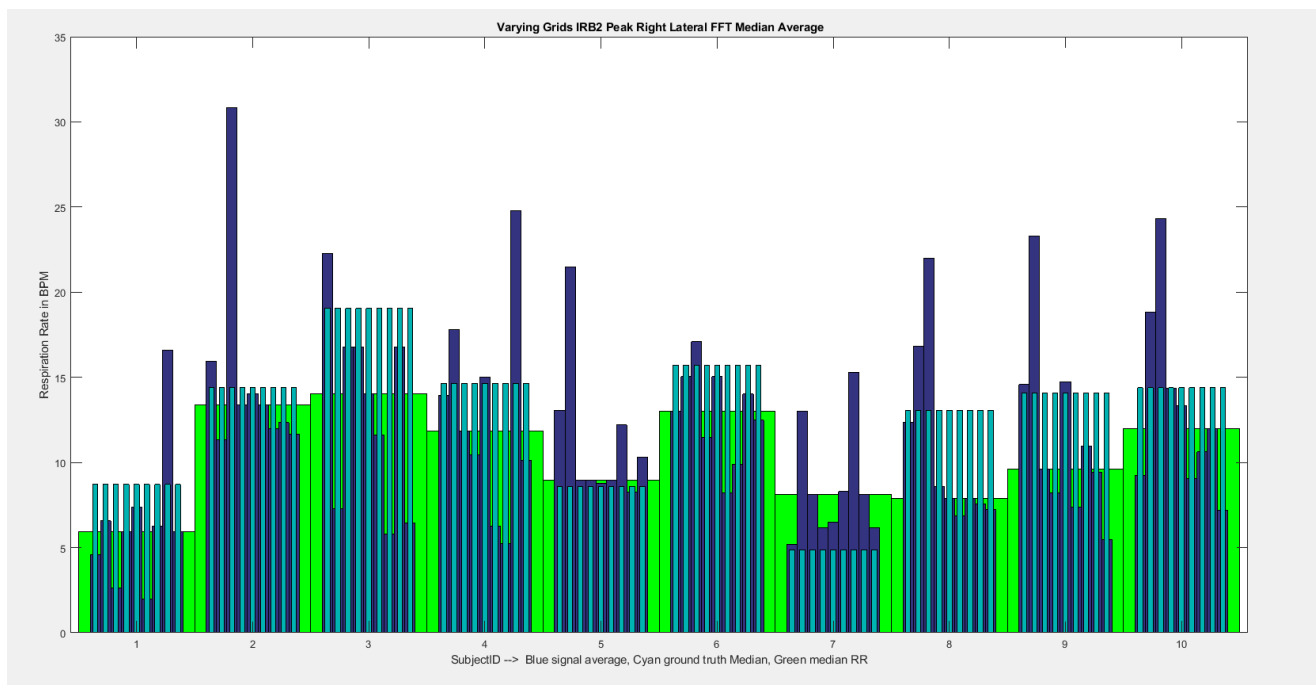


Figure (6AA) shows the algorithm respiration detection rate, for subjects 16-25, grids 7, 8, 9, 12, 13, 14, 17, 18, 19. Cyan is the ground truth, blue is the respiration rate from the depth data, Green is the median Respiration rate from all the grids.

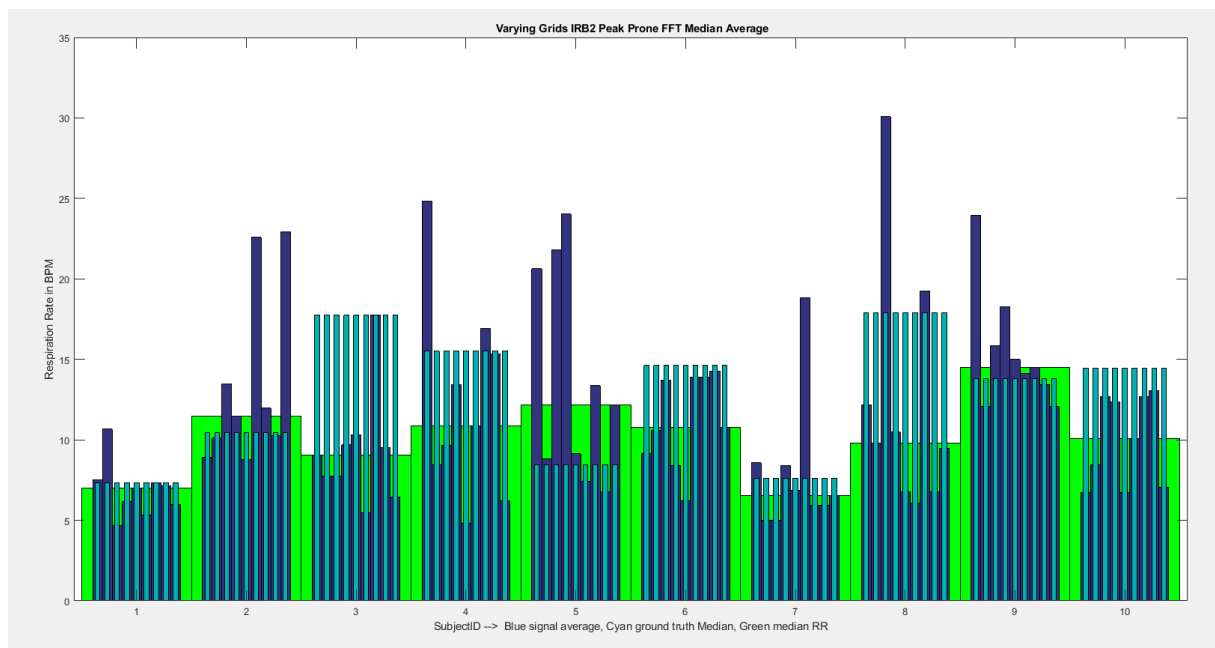


Figure (6AB) shows the algorithm respiration detection rate, for subjects 16-25, grids 7, 8, 9, 12, 13, 14, 17, 18, 19. Cyan is the ground truth, blue is the respiration rate from the depth data, Green is the median Respiration rate from all the grids.

6.4.2. Median

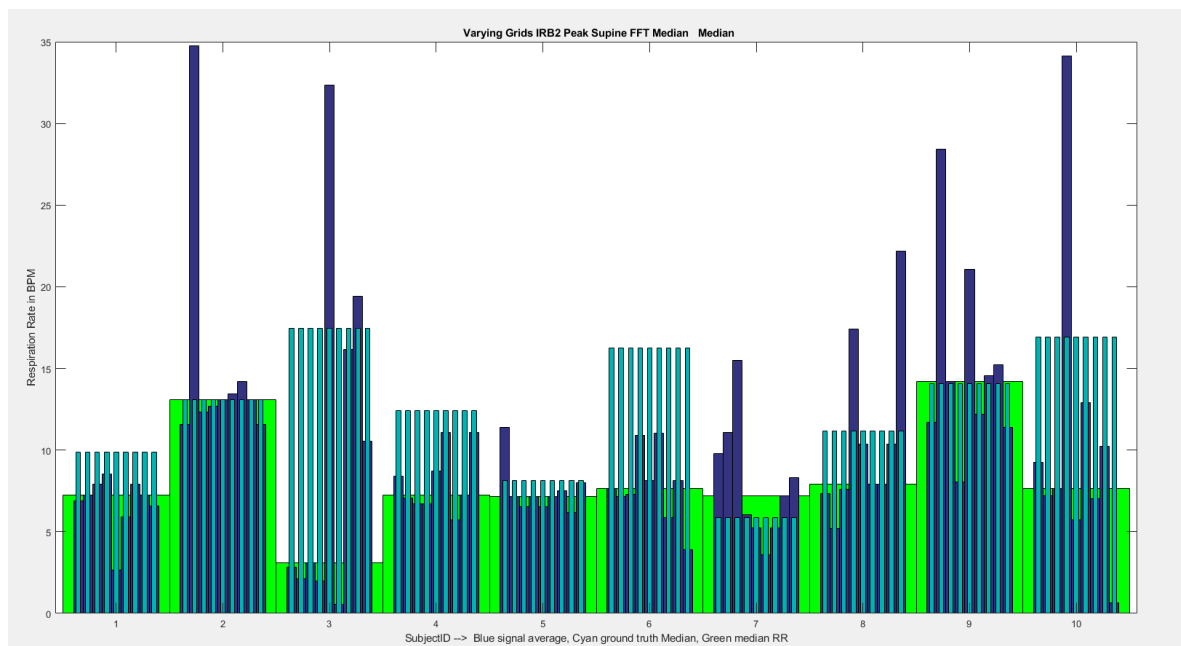


Figure (6AC) shows the algorithm respiration detection rate, for subjects 16-25, grids 7, 8, 9, 12, 13, 14, 17, 18, 19. Cyan is the ground truth, blue is the respiration rate from the depth data, Green is the median Respiration rate from all the grids.

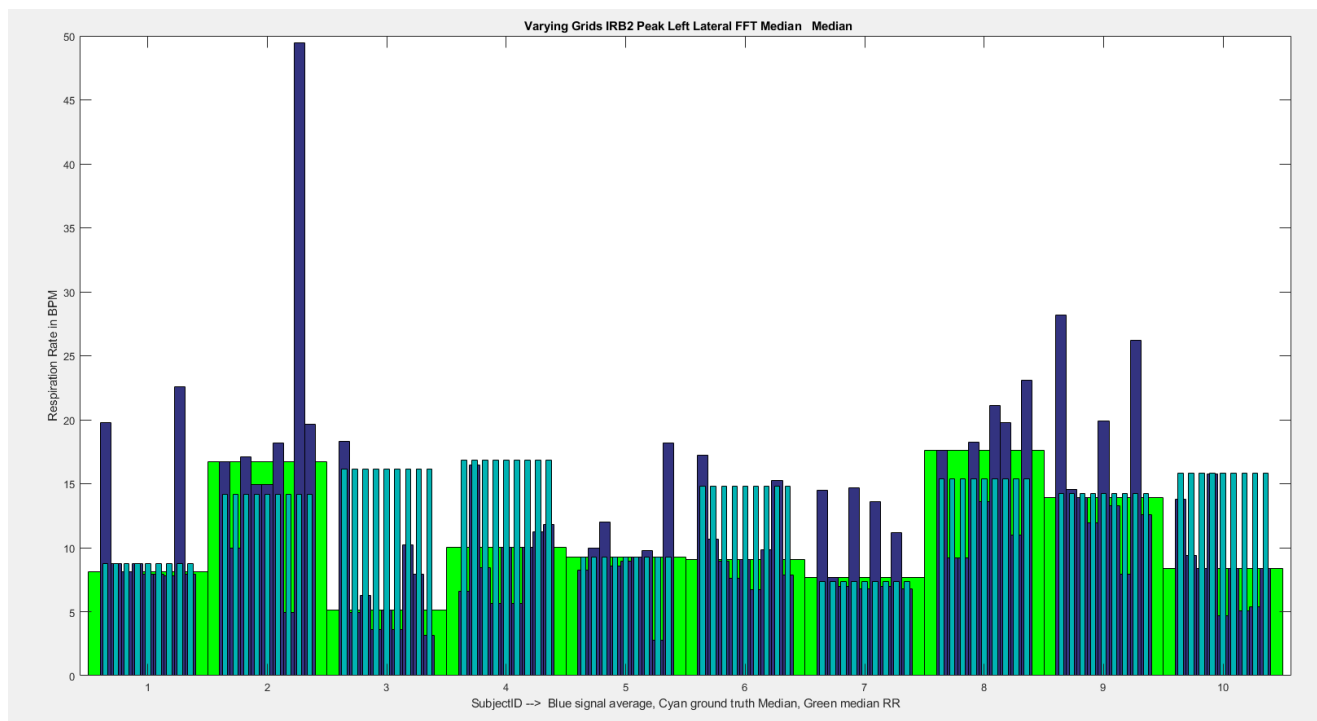


Figure (6AD) shows the algorithm respiration detection rate, for subjects 16-25, grids 7, 8, 9, 12, 13, 14, 17, 18, 19. Cyan is the ground truth, blue is the respiration rate from the depth data, Green is the median Respiration rate from all the grids.

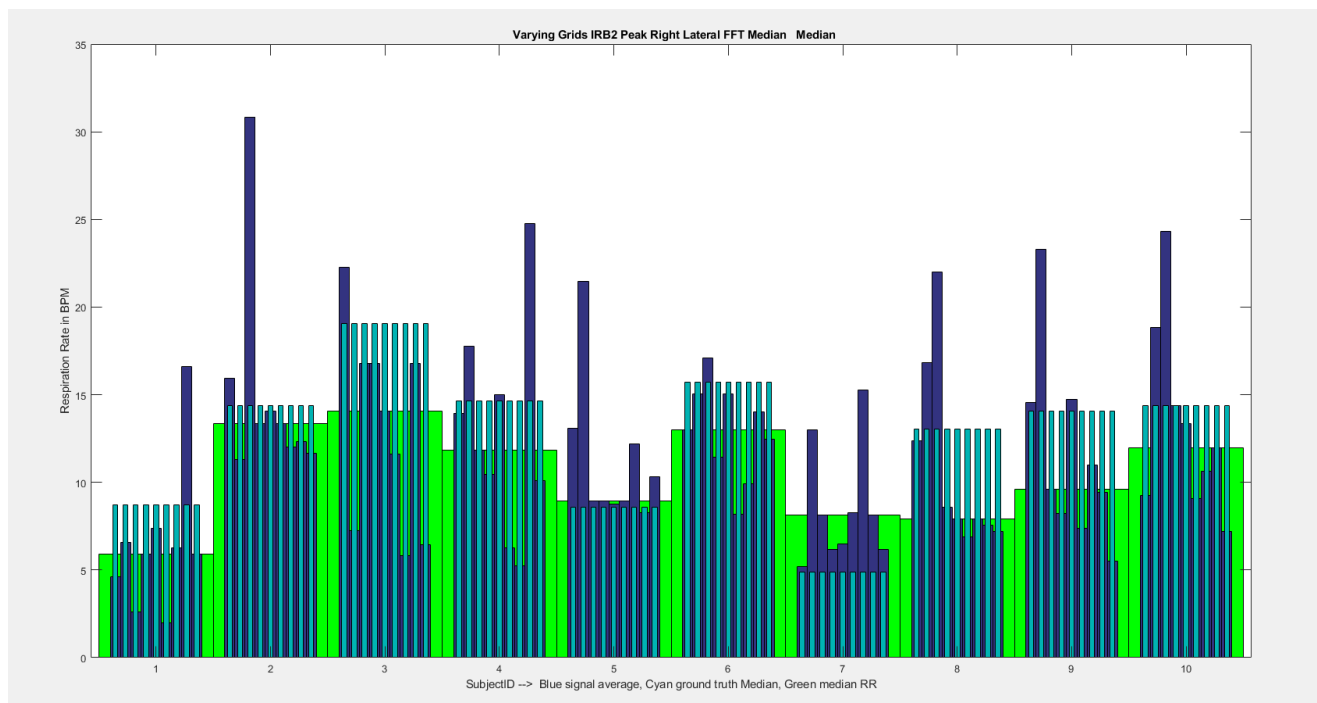


Figure (6AE) shows the algorithm respiration detection rate, for subjects 16-25, grids 7, 8, 9, 12, 13, 14, 17, 18, 19. Cyan is the ground truth, blue is the respiration rate from the depth data, Green is the median Respiration rate from all the grids.

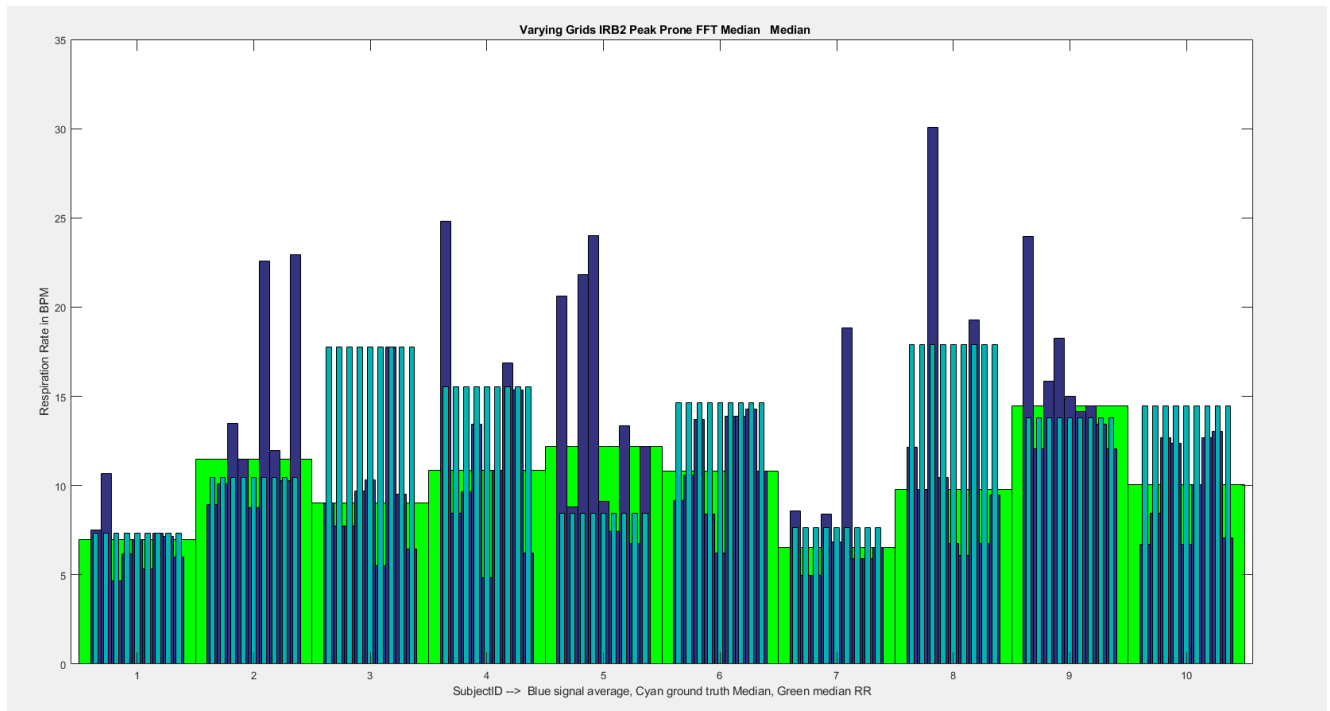


Figure (6AF) shows the algorithm respiration detection rate, for subjects 16-25, grids 7, 8, 9, 12, 13, 14, 17, 18, 19. Cyan is the ground truth, blue is the respiration rate from the depth data, Green is the median Respiration rate from all the grids.

Chapter 7

Discussion

7.1. Results

7.1.1 Pre IRB Results

We anticipated and verified a higher variation in the depth values for the supine posture, as the variation of the rib cage moving toward or away from the depth camera is the highest. We also expected to see some visible variations in the left and right lateral positions.

The three waveforms observed are for the respiration variation based on three different positions, i.e. for supine, left shoulder lateral and right shoulder lateral.

Table (7A) shows the average respiratory accuracy % rate of various parameters for three positions for the Pre IRB initial 5 trials. As seen in table 7A, the algorithm is able to detect the respiration rate with high accuracy. We can see that the supine position gave a better accuracy than the left or right shoulder positions.

Posture	P1-Supine	P2 - Left shoulder	P3-Right shoulder
Respiration Count (number of peaks) %	89.2	80	84.6
Breath-2-breath interval (average peak-2-peak distance in seconds)%	89.2	86	87.6
Breath-2-breath respiratory rate, %	88	81.4	84.2
Overall interval (entire length / number peaks) %	90	85.4	87.4
Overall rate (60/Overall interval) %	89.2	80	84.6

Table (7A) shows the algorithm for respiration variation detection for Pre IRB trials

We noticed for a few subjects, the waveform had a lot of noise for a few sleeping positions. The above accuracy figures includes the beginning and end of the transition between steady state stable position of the subjects, and higher accuracy values would be possible if they are truncated. Overall, we were able

to obtain respiratory rates that were close to the actual respiratory rates. In computing the respiration accuracy, the difference was considered as if the percentage error is computed, we would get a different percentage error for smaller respiration rate compared to larger respiration rate, even if they differed by the same amount. The accuracy is in breaths per minute (BPM).

7.1.2 IRB2 fixed grids peak detection average

Error Diff between GT and algorithm - Manual best grid selection (BPM)				
Subject	Positions			
	Supine	Left	Right	Prone
MU_IRB_RDT_016	-0.5	1.5	-0.5	-1.1
MU_IRB_RDT_017	0.2	0.2	0.0	-0.6
MU_IRB_RDT_018	0.6	0.3	0.8	1.6
MU_IRB_RDT_019	0.1	0.1	-0.2	0.0
MU_IRB_RDT_020	-1.9	-0.4	-2.2	-0.9
MU_IRB_RDT_021	1.2	-0.3	0.2	-0.1
MU_IRB_RDT_022	-1.8	-0.9	-0.2	0.0
MU_IRB_RDT_023	1.5	0.7	0.9	0.2
MU_IRB_RDT_024	0.5	0.1	0.0	0.3
MU_IRB_RDT_025	-0.2	-0.1	-0.3	-0.5

Table (7B) shows the error in beats per minute between the algorithm run on the Ground truth and the depth data

Table (7B) shows the difference in respiration rates in beats per minute between the peak detection algorithm run on the ground truth and the respiration depth data variation with fixed grids, on manually selecting the best grid. We can see that the maximum over estimation is about 1.6 bpm and maximum under estimation is about 2.2bpm. The above table is obtained from Figures (6A), (6B), (6C) and (6D).

error Diff between GT and algorithm - Auto best grid selection (BPM)				
Subject	Positions			
	Supine	Left	Right	Prone
MU_IRB_RDT_016	-3.9	-1.6	-3.4	-1.1
MU_IRB_RDT_017	-1.4	-0.2	0.6	-0.7
MU_IRB_RDT_018	1.1	0.3	2.6	1.9
MU_IRB_RDT_019	1.8	-2.8	-0.4	0.3
MU_IRB_RDT_020	-1.9	-5.6	-6.4	-3.6
MU_IRB_RDT_021	1.2	-0.4	-0.4	-0.2
MU_IRB_RDT_022	-1.8	-4.6	-5.3	-2.3
MU_IRB_RDT_023	2.3	3.6	-0.6	0.3
MU_IRB_RDT_024	0.5	-0.9	0.2	-0.9
MU_IRB_RDT_025	0.4	-1.5	0.5	-0.5

Table (7C) shows the error in beats per minute between the algorithm run on the Ground truth and the depth data

Table (7C) shows the difference in respiration rates in beats per minute between the peak detection algorithm run on the ground truth and the respiration depth data variation with fixed grids, on selection of best grid by automated algorithm. We can see that the maximum over estimation is about 3.6 bpm and maximum under estimation is about 6.4bpm. The above table is obtained from Figures (6A), (6B), (6C) and (6D).

7.1.3 IRB2 fixed grids peak detection median of grids

Error Diff between GT and algorithm – Median RR of grids around chest (BPM)				
Subject	Positions			
	Supine	Left	Right	Prone
MU_IRB_RDT_016	-3.5	-4.6	-2.2	-4.0
MU_IRB_RDT_017	-1.2	-0.2	0.4	-1.6
MU_IRB_RDT_018	1.7	0.6	2.6	2.7
MU_IRB_RDT_019	-0.9	-1.4	0.6	-0.2
MU_IRB_RDT_020	-5.1	-4.9	-5.7	-3.4
MU_IRB_RDT_021	2.7	-0.3	0.6	0.4
MU_IRB_RDT_022	-4.8	-5.5	-4.0	-0.6
MU_IRB_RDT_023	2.9	4.5	0.9	1.4
MU_IRB_RDT_024	-0.9	-0.9	0.6	-0.5
MU_IRB_RDT_025	0.4	-0.4	0.5	-0.9

Table (7D) shows the error in beats per minute between the algorithm run on the Ground truth and the Respiration data

Table (7D) shows the difference in respiration rates in beats per minute between the peak detection algorithm run on the ground truth and the median respiration rate of the fixed grids 7, 8, 9, 12, 13, 14, 17, 18, 19 from the respiration depth data variation. We can see that the maximum over estimation is about 4.5 bpm and maximum under estimation is about 5.7bpm. The above table is obtained from Figures (6A), (6B), (6C) and (6D).

7.1.4 IRB2 varying grids peak detection average

Error Diff between RR algorithm and GT, Manual best grid selection (BPM)				
Subject	Positions			
	Supine	Left	Right	Prone
MU_IRB_RDT_016	-1.5	-2.7	-0.3	-0.8
MU_IRB_RDT_017	0.0	0.2	0.0	0.0
MU_IRB_RDT_018	1.7	-0.1	1.3	1.3
MU_IRB_RDT_019	0.1	-0.1	-0.2	-0.2
MU_IRB_RDT_020	-3.4	0.3	-0.2	-1.9
MU_IRB_RDT_021	2.1	-0.3	-0.4	0.1
MU_IRB_RDT_022	-7.1	-4.6	0.0	0.0
MU_IRB_RDT_023	0.2	1.1	1.2	0.3
MU_IRB_RDT_024	-0.4	0.0	0.0	0.1
MU_IRB_RDT_025	0.0	0.0	-0.1	-0.2

Table (7E) shows the error in beats per minute between the algorithm run on the Ground truth and the Respiration data

Table (7E) shows the difference in respiration rates in beats per minute between the peak detection algorithm run on the ground truth and the median of the respiration rate from grids 7, 8, 9, 12, 13, 14, 17, 18, 19 from the respiration depth data variation with varying grids. We can see that the maximum over estimation is about 2.1 bpm and maximum under estimation is about 7.1bpm. The above table is obtained from Figures (6I), (6J), (6K) and (6L).

error Diff between RR and GT, Auto best grid selection (BPM)				
Subject	Positions			
	Supine	Left	Right	Prone
MU_IRB_RDT_016	-5.4	-6.7	-3.8	-0.8
MU_IRB_RDT_017	-0.1	-0.6	0.1	-4.1
MU_IRB_RDT_018	2.6	0.6	3.3	1.3
MU_IRB_RDT_019	-3.5	-2.9	0.9	-0.3
MU_IRB_RDT_020	-7.8	0.3	-3.9	-2.2
MU_IRB_RDT_021	2.4	-0.6	0.6	0.4
MU_IRB_RDT_022	-7.1	-5.7	-3.3	-2.7
MU_IRB_RDT_023	3.9	1.1	1.8	-0.5
MU_IRB_RDT_024	-1.5	-0.9	0.9	0.1
MU_IRB_RDT_025	0.5	0.8	0.3	-1.0

Table (7F) shows the error in beats per minute between the algorithm run on the Ground truth and the Respiration data

Table (7F) shows the difference in respiration rates in beats per minute between the peak detection algorithm run on the ground truth and the median of the respiration rate from grids 7, 8, 9, 12, 13, 14, 17, 18, 19 from the respiration depth data variation with varying grids, on automatically selecting the best grid. We can see that the maximum over estimation is about 3.9 bpm and maximum under estimation is about 7.8bpm. The above table is obtained from Figures (6I), (6J), (6K) and (6L).

7.1.5 IRB2 varying grids peak detection median of grids

error Diff between GT and algorithm – Median RR of grids around chest (BPM)				
Subject	Positions			
	Supine	Left	Right	Prone
MU_IRB_RDT_016	-3.4	-5.0	-1.3	-4.1
MU_IRB_RDT_017	-1.8	-0.3	0.2	-2.2
MU_IRB_RDT_018	2.6	0.7	3.6	2.6
MU_IRB_RDT_019	-1.9	-0.4	0.7	-0.3
MU_IRB_RDT_020	-6.0	-4.8	-5.0	-3.1
MU_IRB_RDT_021	2.2	-0.9	1.3	0.2
MU_IRB_RDT_022	-5.4	-5.3	-4.6	-2.7
MU_IRB_RDT_023	2.5	4.1	1.5	1.3
MU_IRB_RDT_024	-1.0	-0.5	0.6	0.1
MU_IRB_RDT_025	0.5	0.0	0.3	-0.4

Table (7G) shows the error in beats per minute between the algorithm run on the Ground truth and the Respiration variation

Table (7G) shows the difference in respiration rates in beats per minute between the peak detection algorithm run on the ground truth and the median of the respiration rate from grids 7, 8, 9, 12, 13, 14, 17, 18, 19 from respiration depth data variation with varying grids. We can see that the maximum over estimation is about 4.1 bpm and maximum under estimation is about 6.0bpm. The above table is obtained from Figures (6I), (6J), (6K) and (6L).

7.1.6 IRB2 fixed grids FFT detection average

Error Diff between RR and GT, Manual best grid selection				
Subject	Positions			
	Supine	Left	Right	Prone
MU_IRB_RDT_016	0.2	0.0	1.4	0.2
MU_IRB_RDT_017	0.0	-1.3	0.7	-0.2
MU_IRB_RDT_018	2.5	0.3	2.3	0.3
MU_IRB_RDT_019	1.3	0.4	-0.5	1.7
MU_IRB_RDT_020	0.2	0.0	0.0	-0.3
MU_IRB_RDT_021	-1.6	-0.2	1.7	0.4
MU_IRB_RDT_022	-0.3	-0.7	-0.3	0.0
MU_IRB_RDT_023	-0.6	-1.1	0.7	-4.1
MU_IRB_RDT_024	-1.7	-1.0	-0.2	0.0
MU_IRB_RDT_025	2.1	0.3	0.0	1.4

Table (7H) shows the error in beats per minute between the algorithm run on the Ground truth and the Respiration variation

Table (7H) shows the difference in respiration rates in beats per minute between the FFT detection algorithm run on the ground truth and the respiration depth data variation. We can see that the maximum over estimation is about 2.5 bpm and maximum under estimation is about 4.1bpm. The above table is obtained from Figures (6Q), (6R), (6S) and (6T).

error Diff between RR and GT, Auto best grid selection(BPM)				
Subject	Positions			
	Supine	Left	Right	Prone
MU_IRB_RDT_016	5.1	0.0	-22.2	0.2
MU_IRB_RDT_017	0.0	-2.5	4.3	-0.2
MU_IRB_RDT_018	5.8	0.3	12.6	0.3
MU_IRB_RDT_019	2.5	0.8	-0.5	11.0
MU_IRB_RDT_020	0.0	0.3	-0.5	-11.7
MU_IRB_RDT_021	4.9	-0.5	9.2	0.4
MU_IRB_RDT_022	1.3	-1.4	-1.6	-1.6
MU_IRB_RDT_023	3.0	-15.0	5.5	7.4
MU_IRB_RDT_024	3.3	1.7	4.8	0.0
MU_IRB_RDT_025	10.2	11.9	0.0	6.7

Table (7I) shows the error in beats per minute between the algorithm run on the Ground truth and the Respiration variation

Table (7I) shows the difference in respiration rates in beats per minute between the FFT detection algorithm run on the ground truth and the respiration depth data variation, for automated best grid selection. We can see that the maximum over estimation is about 12.6 bpm and maximum under estimation is about 22.2bpm. The above table is obtained from Figures (6Q), (6R), (6S) and (6T).

7.1.7 IRB2 fixed grids FFT detection median of grids

Error Diff between GT and algorithm – Median RR of grids around chest (BPM)				
Subject	Positions			
	Supine	Left	Right	Prone
MU_IRB_RDT_016	3.6	0.6	2.8	0.3
MU_IRB_RDT_017	0.0	-2.5	1.7	-0.2
MU_IRB_RDT_018	13.2	10.6	4.5	9.7
MU_IRB_RDT_019	5.7	6.8	1.7	7.1
MU_IRB_RDT_020	1.0	0.3	-0.3	-2.4
MU_IRB_RDT_021	8.4	6.0	5.8	0.4
MU_IRB_RDT_022	-0.7	0.4	-1.6	1.1
MU_IRB_RDT_023	0.5	-3.1	5.5	8.5
MU_IRB_RDT_024	1.0	1.3	1.7	0.0
MU_IRB_RDT_025	8.6	10.8	1.0	6.0

Table (7J) shows the error in beats per minute between the algorithm run on the Ground truth and the Respiration variation

Table (7J) shows the difference in respiration rates in beats per minute between the FFT detection algorithm run on the ground truth and the median of the respiration rate from grids 7, 8, 9, 12, 13, 14, 17, 18, 19 from respiration depth data variation with fixed grids. We can see that the maximum over estimation is about 13.2 bpm and maximum under estimation is about 3.1bpm. The above table is obtained from Figures (6Q), (6R), (6S) and (6T).

7.1.8 IRB2 varying grids FFT detection average

error Diff between GT and RR, Manual best grid selection (BPM)				
Subject	Positions			
	Supine	Left	Right	Prone
MU_IRB_RDT_016	1.3	0.0	1.3	0.0
MU_IRB_RDT_017	0.0	-0.7	0.4	0.2
MU_IRB_RDT_018	1.3	-2.1	2.3	0.0
MU_IRB_RDT_019	1.3	0.4	-0.4	0.2
MU_IRB_RDT_020	0.2	0.0	-0.3	-0.3
MU_IRB_RDT_021	5.2	-0.5	0.7	0.4
MU_IRB_RDT_022	-0.2	-0.3	-0.3	-0.8
MU_IRB_RDT_023	0.8	1.8	0.7	-1.3
MU_IRB_RDT_024	0.0	-0.3	-0.5	-0.4
MU_IRB_RDT_025	4.0	0.0	0.0	1.4

Table (7K) shows the error in beats per minute between the algorithm run on the Ground truth and the Respiration variation

Table (7K) shows the difference in respiration rates in beats per minute between the FFT detection algorithm run on the ground truth and the respiration depth data variation with varying grids. We can see that the maximum over estimation is about 5.2 bpm and maximum under estimation is about 2.1bpm. The above table is obtained from Figures (6Y), (6Z), (6AA) and (6AB).

error Diff between GT and RR, Auto best grid selection (BPM)				
Subject	Positions			
	Supine	Left	Right	Prone
MU_IRB_RDT_016	1.3	0.0	-7.9	0.2
MU_IRB_RDT_017	0.0	-0.7	0.4	-1.0
MU_IRB_RDT_018	-2.0	11.1	13.2	0.0
MU_IRB_RDT_019	5.4	0.4	4.5	10.7
MU_IRB_RDT_020	1.0	0.3	-3.6	-0.3
MU_IRB_RDT_021	8.6	4.1	0.7	0.7
MU_IRB_RDT_022	2.3	-7.3	-1.3	-0.8
MU_IRB_RDT_023	-6.3	1.8	5.2	5.8
MU_IRB_RDT_024	1.8	1.0	5.8	-1.2
MU_IRB_RDT_025	9.9	7.4	0.0	7.4

Table (7L) shows the error in beats per minute between the algorithm run on the Ground truth and the Respiration variation

Table (7L) shows the difference in respiration rates in beats per minute between the FFT detection algorithm run on the ground truth and the respiration depth data variation with varying grids. We can see that the maximum over estimation is about 13.2 bpm and maximum under estimation is about 7.9bpm. The above table is obtained from Figures (6Y), (6Z), (6AA) and (6AB).

7.1.9 IRB2 varying grids FFT detection median of grids

error Diff between GT and algorithm - Median of grids around chest (BPM)				
Subject	Positions			
	Supine	Left	Right	Prone
MU_IRB_RDT_016	2.6	0.6	2.8	0.3
MU_IRB_RDT_017	0.0	-2.5	1.0	-1.0
MU_IRB_RDT_018	14.3	11.1	5.0	8.7
MU_IRB_RDT_019	5.2	6.8	2.8	4.7
MU_IRB_RDT_020	1.0	0.0	-0.3	-3.7
MU_IRB_RDT_021	8.6	5.7	2.7	3.8
MU_IRB_RDT_022	-1.3	-0.3	-3.3	1.1
MU_IRB_RDT_023	3.3	-2.2	5.2	8.1
MU_IRB_RDT_024	-0.2	0.3	4.5	-0.7
MU_IRB_RDT_025	9.3	7.4	2.4	4.4

Table (7M) shows the error in beats per minute between the algorithm run on the Ground truth and the Respiration variation

Table (7M) shows the difference in respiration rates in beats per minute between the FFT detection algorithm run on the ground truth and the median of the respiration rates from the grids 7, 8, 9, 12, 13, 14, 17, 18, 19 from respiration depth data variation with varying grids. We can see that the maximum over estimation is about 14.3 bpm and maximum under estimation is about 3.7bpm. The above table is obtained from Figures (6Y), (6Z), (6AA) and (6AB).

7.1.10 Overall Accuracy

Manual best grid selection		Supine	Left	Right	Prone	Mean
IRB2 grid fixed peak average	Mean error difference	0.9	0.5	0.5	0.5	0.6
IRB2 grid varying peak average	Mean error difference	1.7	0.9	0.4	0.5	0.9
IRB2 grid fixed FFT average	Mean error difference	1.0	0.5	0.8	0.9	0.8
IRB2 grid varying FFT average	Mean error difference	1.4	0.6	0.7	0.5	0.8

Table (7N) shows the average absolute error in bpm between RR and GT for manual best grid selection

Automated best grid selection		Supine	Left	Right	Prone	Mean
IRB2 grid fixed peak average	Mean error difference	1.6	2.2	2.0	1.2	1.7
IRB2 grid varying peak average	Mean error difference	3.5	2.0	1.9	1.3	2.2
IRB2 grid fixed FFT average	Mean error difference	3.6	3.4	6.1	3.9	4.3
IRB2 grid varying FFT average	Mean error difference	3.9	3.4	4.3	2.8	3.6

Table (7O) shows the average absolute error in bpm between RR and GT for automated best grid selection

Median of chest region grids		Supine	Left	Right	Prone	Mean
IRB2 grid fixed peak median	Mean error difference	2.4	2.3	1.8	1.6	2.0
IRB2 grid varying peak median	Mean error difference	2.7	2.2	1.9	1.7	2.1
IRB2 grid fixed FFT median	Mean error difference	4.3	4.2	2.7	3.6	3.7
IRB2 grid varying FFT median	Mean error difference	4.6	3.7	3.0	3.7	3.7

Table (7P) shows the average absolute error in bpm between median of RR for grids around chest and GT

The overall accuracy for the system comprising algorithms and hardware can be gauged by the above tables. The above metric is computed using the mean of the absolute differences between the respiration rate from the algorithm and the ground truth. As seen in table (7N), for manual selection of the best grid, we can see that the algorithm has the least possible mean absolute error of about 0.4. As seen in table (7O), for automated selection of the best grid, we can see that the algorithm has the least possible mean absolute error of about 1.2. As seen in table (7P), for median of the respiratory rates for grids around the chest region, we can see that the algorithm has the least possible mean absolute error of about 1.6.

7.2. Challenges

The respiration rate for few of the signals was over estimated compared to the ground truth. On closer investigation, this was due to the depth variation signal being noisier, and thereby the algorithm detected a slightly higher number of peaks than the ground truth. As seen in Fig. (7A), and Fig.(7B), the peaks detected for the depth variation and ground truth for subject #20 grid 13 by the algorithm differ, due to the more number of peaks.

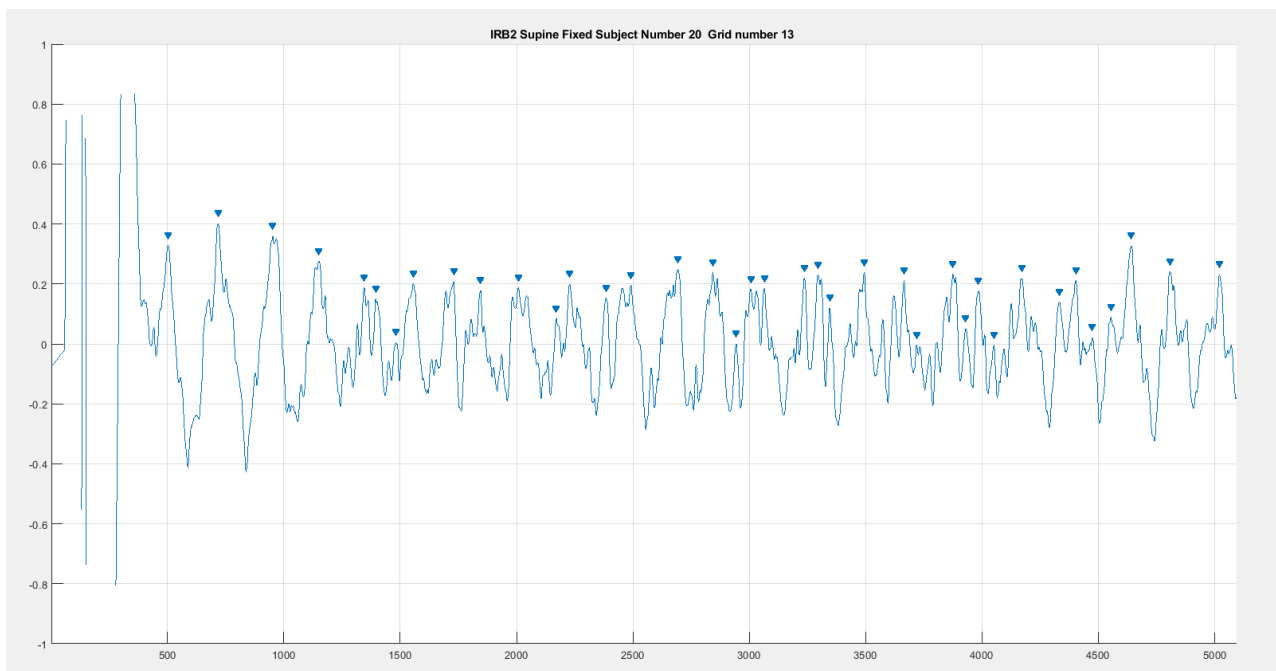


Figure (7A) shows the peak detection algorithm on noisy signal, detecting more than expected peaks for subject #20 grid

13

When training the LSTM-RNN, the classification of signals was not very successful. The training had high accuracy, but it was not able to classify the signals based on object signatures. One probable cause of this was limited data training set. Other algorithms were devised to select the best signal and detect region of interest.

The Signal Energy parameter 1, Signal Variation Factor parameter 2 and Signal strength Parameter 3 were not very effective in selecting the best signal, and thereby the other parameters, Signal symmetry parameter 4, signal variation parameter 5, SNR maxima parameter 6 and SNR minima parameter 7

were used to select the best signal in the grid. Grid selection worked among grids around the chest region, and improved computation time.

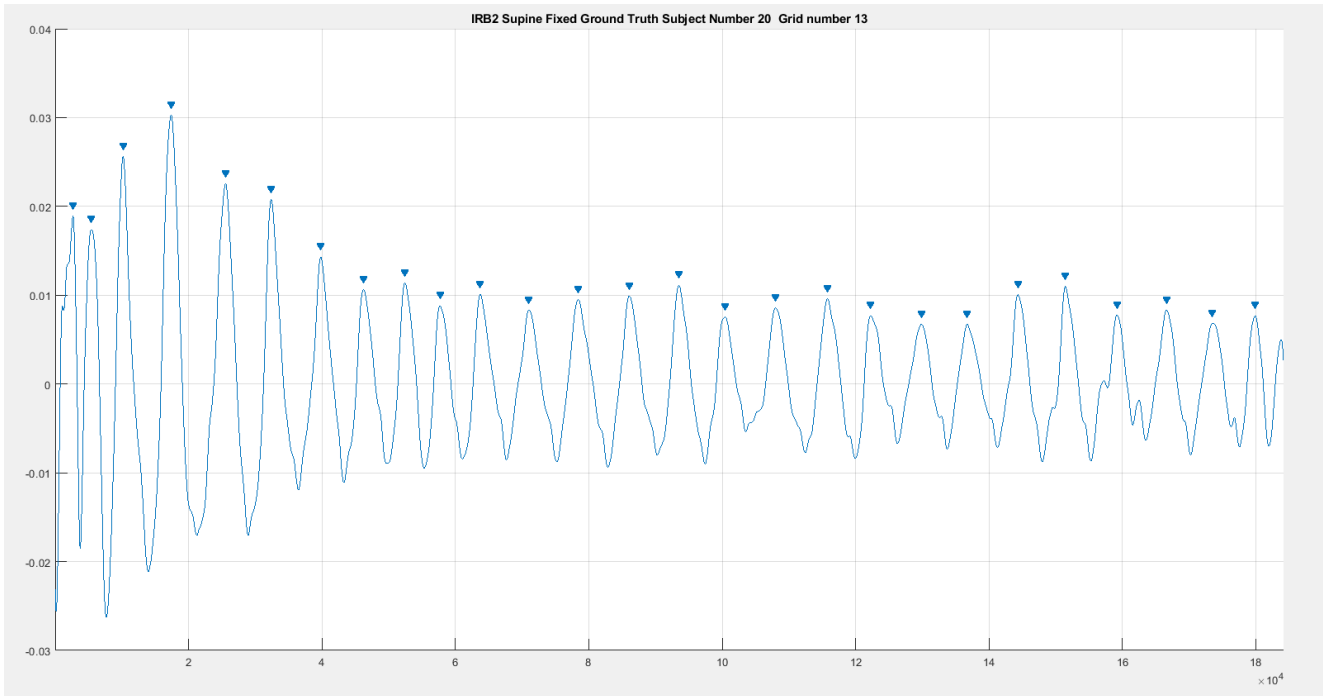


Figure (7B) showing the peak detection algorithm on ground truth for subject #20

IRB1 respiration signals were not very clear due to H264 encoding, and then lossless compression was implemented on the code, and IRB2 was conducted with lossless compression. Lot of testing, trial and error, and delays were seen in processing the code for the entire grid and tuning the parameters for the algorithms.

Tests were conducted with the Raw and encoded depth video captured from the Kinect based DSK3 and the Orbec based DS5 camera, to ensure that the camera was sensitive to the depth variation and select the best system for our tests.

Chapter 8

Conclusions

8.1 Contributions

My contributions to this work include the following:

- Code contributions to the OpenCV library for data acquisition and storage of depth and thermal data
- Methods to detect the bed area as the region of interest
- Methods for generating grid on the bed as well as selecting grid size and the best grid for estimating respiration
- Refinement of methods to estimate the respiration rate in the time domain and frequency domain

I would like to immensely thank Dr. Skubic, Dr. Keller, Dr. Popescu and Moein for the valuable guidance and help rendered during multiple instances of progress of this project.

Dr. Skubic provided the concept of considering the grids which have a thermal signature, and which has been implemented as seen in section 4.5.

Moein had helped in troubleshooting the code and refining the graphs for syncing the ground truth and depth variation signal. Moein also provided the concept of the varying grids, which has been implemented as discussed in section 4.4.2. Moein has also coded the three signal parameters, as seen in section 4.9.1, 4.9.2 and 4.9.3.

Dr. Keller and Dr. Popescu provided valuable concepts, suggestions and experiments for helping me refine the results based on mathematical outcomes, which helped me choose the best algorithm to solve the given problem and obtain optimal results.

8.2 Future Work

As part of an enhancement of this paper, we can extend the respiration detection to other viewing perspectives instead of directly perpendicular to the bed, which would provide more flexibility in placement of the sensing device. We can also enhance the algorithm to detect the change in volume based on entire chest depth variation and thus estimate respiration volume. We can also study prospective fuzzy-neural template matching for automated chest region detection, which we hope shall be robust to the movement of the subject, a subject covered by bed linens, and a subject sitting on the bed irrespective of the direction or orientation or posture of the person. We also plan to adopt Recurrent Neural Network especially the Long-Short-Term-Memory, to differentiate between noisy signals and clean signals of respiration. This methodology can have far and wide applications for analysis of other biomedical / non biomedical signal processing and interpretation. This will also give us the possibility of extracting the respiration volume, respiratory rate variability and restlessness along with restless body movement.

We can now say that we have a reliable method of non-invasively estimating the respiratory rate of persons sleeping on the bed. The work done here shall be beneficial for passive and active healthcare analytics.

BIBLIOGRAPHY

- [1] J. Coughlin and J. Pope, "Innovations in health, wellness, and aging-in-place," vol. 17, 2008, pp. 47 – 52.
- [2] C. Fausset, A. Kelly, W. Rogers, and A. Fisk, "Challenges to aging in place: Understanding home maintenance difficulties," vol. 25, no. 2, 2011, pp. 125–141.
- [3] "Average in-home gait speed: investigation of a new metric for mobility and fall risk assessment of elders." Stone E, Skubic M, Rantz M, Abbott C, Miller S. *Gait Posture*. 2015 Jan;41(1):57-62. doi: 10.1016/j.gaitpost.2014.08.019. Epub 2014 Sep 6. PMID:25245308.
- [4] Farah Q Al-Khalidi, Reza Saatchi, Derek Burke, Heather E Elphick, Stephen Tan. "Respiration Rate Monitoring Methods: A Review". *Pediatric Pulmonology*, Wiley, 2011, 46 (6)
- [5] Hyoung Jong Kim, Ki Ho Kim, Yun Seok Hong, and Jin Joo Choi "Measurement of human heartbeat and respiration signals using phase detection radar" *Review of Scientific Instruments* 78, 104703 (2007)
- [6] F. Benetazzo, A. Freddi, A. Monteriù and S. Longhi, "Respiratory rate detection algorithm based on RGB-D camera: theoretical background and experimental results," in *Healthcare Technology Letters*, vol. 1, no. 3, pp. 81-86, 09 2014.
- [7] S. Šprager and D. Zazula, "Heartbeat and Respiration Detection From Optical Interferometric Signals by Using a Multimethod Approach," in *IEEE Transactions on Biomedical Engineering*, vol. 59, no. 10, pp. 2922-2929, Oct. 2012.
- [8] F. Q. AL-Khalidi, R. Saatchi, D. Burke and H. Elphick, "Tracking human face features in thermal images for respiration monitoring," *ACS/IEEE International Conference on Computer Systems and Applications - AICCSA 2010, Hammamet, 2010*, pp. 1-6.

- [9] K. Y. Lin, D. Y. Chen, C. Yang, K. J. Chen and W. J. Tsai, "Automatic Human Target Detection and Remote Respiratory Rate Monitoring," 2016 IEEE Second International Conference on Multimedia Big Data (BigMM), Taipei, 2016, pp. 354-356.
- [10] T. Harada, T. Mori, Y. Nishida, T. Yoshimi and T. Sato, "Body parts positions and posture estimation system based on pressure distribution image," Proceedings 1999 IEEE International Conference on Robotics and Automation (Cat. No.99CH36288C), Detroit, MI, 1999, pp. 968-975 vol.2.
- [11] Microsoft Kinect Visual and Depth Sensors for Breathing and Heart Rate Analysis, Aleš Procházka, Martin Schätz, Oldřich Vyšata, Martin Vališ, *Sensors (Basel)* 2016 July; 16(7): 996.
- [12] F. Benetazzo, A. Freddi, A. Monteriù and S. Longhi, "Respiratory rate detection algorithm based on RGB-D camera: theoretical background and experimental results," in *Healthcare Technology Letters*, vol. 1, no. 3, pp. 81-86, 09 2014.
- [13] Kaveh Bakhtiyari, Nils Beckmann, Jürgen Ziegler, "Contactless heart rate variability measurement by IR and 3D depth sensors with respiratory sinus arrhythmia", *Procedia Computer Science*, Volume 109, 2017, Pages 498-505, ISSN 1877-0509
- [14] T. T. Dang, C. Huynh, K. Tran, A. Dinh, H. D. Nguyen and Q. M. V. Le, "Measuring human respiration rate using depth frames of PrimeSense camera," 2015 International Conference on Advanced Technologies for Communications (ATC), Ho Chi Minh City, 2015, pp. 411-416.
- [15] M. Baboli, O. Boric-Lubecke and V. Lubecke, "A new algorithm for detection of heart and respiration rate with UWB signals," *2012 Annual International Conference of the IEEE Engineering in Medicine and Biology Society*, San Diego, CA, 2012, pp. 3947-3950.
doi: 10.1109/EMBC.2012.6346830
- [16] Johan Vertens, Fabian Fischer, Christian Heyde, Fabian Höflinger, Rui Zhang, Leonhard M. Reindl, Albert Gollhofer, "Measuring Respiration and Heart Rate using Two Acceleration Sensors on a Fully Embedded Platform", Published 2015 in *icSPORTS*, DOI:10.5220/0005604000150023
- [17] Erin Griffiths, T. Scott Saponas, A. J. Bernheim Brush, "Health chair: implicitly sensing heart and respiratory rate" *UbiComp '14 Proceedings of the 2014 ACM International Joint Conference on Pervasive and Ubiquitous Computing*, Pages 661-671 Seattle, Washington — September 13 - 17, 2014, table of contents ISBN: 978-1-4503-2968-2 doi>10.1145/2632048.2632099

- [18] Wusk, Grace and Hampton Gabler. “Non-Invasive Detection of Respiration and Heart Rate with a Vehicle Seat Sensor” *Sensors (Basel, Switzerland)* vol. 18, 5 1463. 8 May. 2018, doi:10.3390/s18051463
- [19] Garn H. et al. (2018) Contactless 3D detection of respiratory effort. In: Eskola H., Väisänen O., Viik J., Hyttinen J. (eds) EMBEC & NBC 2017. EMBEC 2017, NBC 2017. IFMBE Proceedings, vol 65. Springer, Singapore
- [20] https://blogs.technet.microsoft.com/microsoft_blog/2013/10/02/collaboration-expertise-produce-enhanced-sensing-in-xbox-one/
- [21] <http://lttm.dei.unipd.it/nuovo/Papers/ToF-Kinect-book.pdf>
- [22] TigerPlace, “Tigerplace independent living by americare,” 2011. [Online]. Available: www.americareusa.net
- [23] M. J. Rantz, M. Skubic, S. J. Miller, and J. Krampe, “Using technology to enhance aging in placer,” in Proceedings of the International Conference on Smart Home and Health Telematics, Ames, IA, June 2008, pp. 169–176.
- [24] Z. Beattie, C. Hagen, and T. Hayes, “Classification of lying position using load cells under the bed,” in Proceedings of the 33rd Annual International Conference of the IEEE EMBS, Boston, Massachusetts, USA, August 2011.
- [25] Y. Xinsheng, D. Dent, and C. Osborn, “Classification of ballistocardiography using wavelet transform and neural networks,” vol. 3, 1996, pp. 937 – 938.
- [26] D. Heise and M. Skubic, “Monitoring pulse and respiration with a hydraulic bed sensor,” in Proceedings of the 32rd Annual IEEE International Conference of the IEEE Engineering in Medicine and Biology Society, Buenos Aires, Argentina, August 2010, pp. 1926–1929.
- [27] <https://msdn.microsoft.com/en-us/library/jj131033.aspx>
- [28] <https://www.flir.com/products/lepton/>
- [29] https://en.wikipedia.org/wiki/Butterworth_filter

[30] https://en.wikipedia.org/wiki/Savitzky%E2%80%93Golay_filter

[31] <https://www.adinstruments.com/products/powerlab>

[32] <https://www.mathworks.com/help/nnet/ug/long-short-term-memory-networks.html>

[33] Section 11.1.5, Signatures, *Digital Image Processing (3rd Edition)* Prentice-Hall, Inc. Upper Saddle River, NJ, USA ©2006 ISBN:013168728X

[34] Section 8.1.3, Signatures, *Digital image processing (2nd Ed.)* Addison-Wesley Longman Publishing Co., Inc. Boston, MA, USA ©1987 ISBN:0-201-11026-1